Zinc Oxoclusters for Extreme Ultraviolet Lithography

Cover design by Himanshu Jassal & Neha Thakur

ISBN: 978-94-92323-59-0

Full colour version of the thesis and the electronic supplementary information are available at https://dare.uva.nl/en

Printed by ProefschriftMaken

Zinc Oxoclusters for Extreme Ultraviolet Lithography

ACADEMISCH PROEFSCHRIFT

ter verkrijging van de graad van doctor
aan de Universiteit van Amsterdam
op gezag van de Rector Magnificus
prof. dr. ir. K.I.J. Maex
ten overstaan van een door het College voor Promoties ingestelde commissie,
in het openbaar te verdedigen in de Agnietenkapel
op maandag 28 maart 2022, te 14.00 uur

door

Neha Thakur

geboren te Rihru, Himachal Pradesh

Promotiecommissie:

Promotor:	
prof. dr. A.M. Brouwer	Universiteit van Amsterdam
Copromotor:	
dr. S. Castellanos Ortega	Inpria
Overige leden:	
prof. dr. E.L. von Hauff	Universiteit van Amsterdam
prof. dr. S. Woutersen	Universiteit van Amsterdam
prof. dr. B. Ehrler	Rijksuniversiteit Groningen
prof. dr. S. Ghosh	IIT Mandi, India
dr. J. García Santaclara	ASML

Faculteit der Natuurwetenschappen, Wiskunde en Informatica

The research described in this thesis was carried out at the Advanced Research Center for Nanolithography (ARCNL), a public-private partnership between the Universiteit van Amsterdam (UvA), the Vrije Universiteit Amsterdam (VU), the Netherlands Organization for Scientific Research (NWO) and the semiconductor equipment manufacturer ASML.

CONTENTS

1 INTRODUCTION 1
1.1 PHOTOLITHOGRAPHY 2
1.1.1 EUV Lithography 4
1.2 PHOTORESISTS 5
1.2.1 Innovations in Photoresists 5
1.2.2 Challenges for EUV Photoresists 6
1.2.3 Zinc-based metal oxoclusters 10
1.3 OUTLINE AND SCOPE 11

2 STABILITY STUDIES ON SENSITIVE ZINC-BASED OXOCLUSTER: EUV PHOTORESIST 13
2.1 INTRODUCTION 14
2.2 MATERIALS AND METHODS 15
2.2.1 Materials 15
2.2.2 Synthesis of photoresist: Zn(MA)(TFA) 15
2.2.3 Characterization of the bulk material 16
2.2.4 Thin film preparation 16
2.2.5 Characterization of thin films 17
2.2.6 EUV exposure and post-exposure analysis 17
2.3 RESULTS AND DISCUSSIONS 17
2.3.1 Determination of the organic shell composition 17
2.3.2 Stability Studies 20
2.3.3 Sensitivity towards EUV light and lithography performance 24
2.4 CONCLUSIONS 28

3 ZINC-BASED OXOCLUSTER: CHEMISTRY FOR HIGH RESOLUTION NANOLITHOGRAPHY 31
3.1 INTRODUCTION 32

3.2 MATERIALS AND METHODS ... 33
3.2.1 Zn(MA)(TFA) material and thin film deposition ... 33
3.2.2 EUV exposure and development ... 34
3.2.3 Post-exposure analysis ... 35
3.3 RESULTS AND DISCUSSIONS ... 35
3.3.1 EUV lithography performance ... 35
3.3.2 Mechanistic Insights ... 39
3.4 CONCLUSIONS ... 45

4 PHOTON-INDUCED FRAGMENTATIONS OF ZINC OXOCLUSTER ... 47
4.1 INTRODUCTION ... 48
4.2 MATERIALS AND METHODS ... 49
4.2.1 Synthesis of photoresist: Zn(MA)(TFA) ... 49
4.2.2 Sample preparation and Experimental details ... 49
4.3 RESULTS AND DISCUSSIONS ... 51
4.4 CONCLUSIONS ... 57

5 ROLE OF ELECTRONS IN THE SOLUBILITY SWITCH OF ZINC OXOCLUSTER ... 59
5.1 INTRODUCTION ... 60
5.2 MATERIALS AND METHODS ... 62
5.2.1 Preparation of Zn(MA)(TFA) resist layers ... 62
5.2.2 Reflection absorption infrared spectroscopy ... 62
5.2.3 Electron irradiation and monitoring of evolving volatile species ... 63
5.3 RESULTS AND DISCUSSIONS ... 64
5.3.1 Electron-stimulated desorption from Zn(MA)(TFA) and Zn(TFA) resist layers ... 64
5.3.2 RAIRS of Zn(MA)(TFA) and Zn(TFA) resist layers ... 69
5.3.3 Electron-stimulated conversion of Zn(MA)(TFA) resist layers monitored by RAIRS ... 70
5.3.4 Comparison with the EUV results ... 73
5.3.5 Reaction mechanism ... 74
5.4 CONCLUSIONS ... 78

6 FLUORINE-RICH ZINC OXOCLUSTER AS EUV PHOTORESIST ... 79
6.1 INTRODUCTION ... 80
6.2 MATERIALS AND METHODS ... 82
6.2.1 Synthesis of fluorine-rich oxocluster: Zn(TFMA) and Zn(TFMA)(MA)(TFA) ... 82
6.2.2 Silanization process ... 84
6.2.3 Sample preparation for spectroscopy studies ... 84
6.2.4 EUV Exposures ... 85
6.2.5 Post exposure analysis and ex situ spectroscopy study ... 85
6.2.6 In situ XPS study ... 86

6.3 RESULTS AND DISCUSSIONS 86
6.3.1 Processability and stability studies 86
6.3.2 Thin films and Contrast curves 87
6.3.3 EUV-IL performance of fluorine-rich Zn oxoclusters 89
6.3.4 Effect of PEB on EUV-IL performance 90
6.3.5 STXM measurements 91
6.3.6 UV-vis spectroscopy 92
6.3.7 Infrared spectroscopy 93
6.3.8 Post-EUV exposure in situ XPS 94
6.3.9 Reaction mechanism 97
6.4 CONCLUSIONS 99

REFERENCES **101**

APPENDIX **113**

SUMMARY **121**

SAMENVATTING **125**

PUBLICATION LIST **129**

ACKNOWLEDGEMENTS **131**

1

INTRODUCTION

The semiconductor industry has gone through astounding advancements over the years, beginning from fabricating a single transistor on a chip in the early 1960s to fabricating 50 billion transistors on a chip of a size similar to our fingernail.[1,2] The products of the semiconductor industry have a profound impact on our modern life. Electronic devices, from well-established computers and mobile phones to futuristic human micro-chip implants and self-driving cars, have achieved impressive functionality due to the tiny complex systems embedded on small chips. These chips are the product of the semiconductor industry, and transistors are the foundation of these complex integrated circuits (IC) on a chip.[3] The invention of the transistor in 1948 by Bell laboratory engineers replaced the less-suitable and inefficient vacuum tubes and led the way to one of the biggest revolutions in the semiconductor industry.[4,5] With this revolution, computers which once occupied an entire room have shrunk to occupying a mere little corner in a room.

In today's age of information, modern computers can perform trillions of calculations per second. All this computing power is generated from a silicon chip having a multitude of transistors, designed and manufactured with incredible precision. The race for having smaller, faster and smarter electronics still continues by squeezing more transistors onto a single silicon chip. More transistors on a single chip simply mean more computing power, which translates into *small is good, i*n the semiconductor industry. The semiconductor industry has sworn by one rule over these years: Moore's law.[6,7] Moore's law is based on observation and projection of doubling of the number of components per IC every two years. In the words of Intel[8]:

"In 1965, Gordon Moore made a prediction that would set the pace for our modern digital revolution. From careful observation of an emerging trend, Moore extrapolated that computing would dramatically increase in power, and decrease in relative cost, at an

exponential pace. The insight, known as Moore's Law, became the golden rule for the electronics industry, and a springboard for innovation. As a co-founder, Gordon paved the path for Intel to make the ever faster, smaller, more affordable transistors that drive our modern tools and toys. Even over 50 years later, the lasting impact and benefits are felt in many ways."

1.1 Photolithography

The key technology for large-scale production of IC's is photolithography and the shrinking of feature sizes and an increase in the density of the circuit has been made possible by the advancements in photolithography over the years. Photolithography (also known as optical lithography) starts with coating a thin film of a photosensitive material, photoresist, on the substrate. A pattern of light is projected onto the thin film, causing local chemical reactions responsible for the change in the solubility of the material (solubility switch) followed by a subsequent development such that only desired parts of the substrate remain covered with resist material while unwanted parts are washed away to obtain the 3D features.[9,10]

Photoresists are classified as positive-tone or negative-tone resists. If the chemical changes in the exposed parts result in an increased solubility of photoresist in the developer compared to the unexposed area, the photoresist is considered as a positive-tone photoresist. While, if the chemical changes in the exposed area of photoresist result in a decreased solubility in the developer as compared to the unexposed part, the photoresist is defined as a negative-tone photoresist. A simplified scheme of the basic steps of the photolithography process is shown in Figure 1.1. However, to fabricate a complete IC further steps are needed such as etching, ion implantation etc. with multiple pattern transfers.

The smallest feature size that can be printed depends on two basic factors: (i) the capability of the resist material to undergo localized solubility switch upon exposure to photons such that the unwanted parts can be dissolved by the developer after exposure,[11,12] and (ii) the smallest size that can be theoretically projected on the resist material and is defined according to the Rayleigh resolution criterion:[13,14]

$$\text{smallest feature} = k_1 \frac{\lambda}{\text{NA}} \qquad (1.1)$$

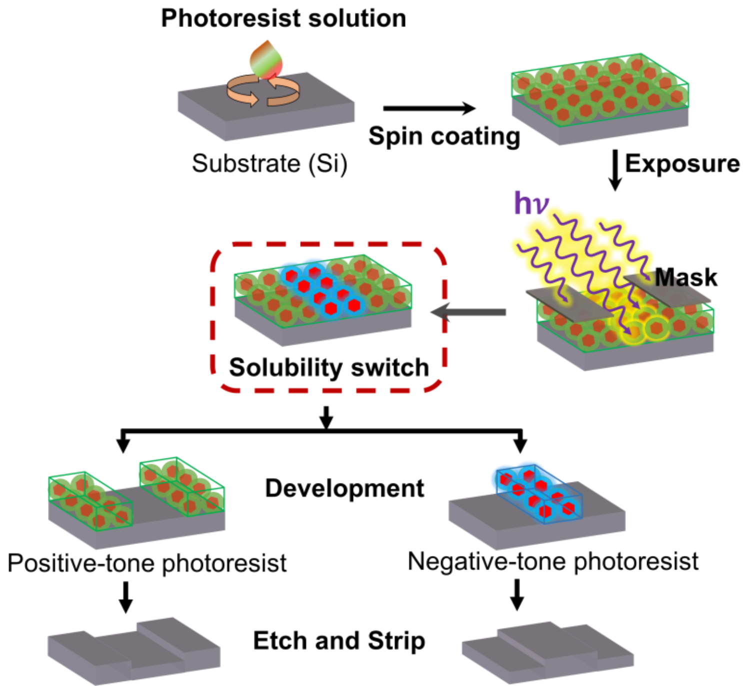

Figure 1.1: Schematic representation of the basic steps in photolithography process: spin coating, exposure to light, development followed by etching and striping. Note: the number of steps can vary in the actual process, for instance, modification of the silicon substrate before spin coating photoresist, post-apply bake (PAB) and post-exposure bake (PEB), etc.

In eq. 1.1, k_1 is dependent on the optical system used for light projection and the resist characteristics combined, λ is the wavelength of the imaging light used and NA is the numerical aperture of the projection optics. Thus, the possible theoretical smallest feature size can either be decreased by increasing the NA or by decreasing k_1 and λ.

Over the years, there has been a continuous increase in the NA and a decrease in k_1 and λ. The imaging light (λ) used in photolithography has evolved from g-line (436 nm) to i-line (365 nm) to KrF (248 nm) to ArF (193 nm) to ArF immersion lithography (ArFi, 193 nm) over the years.[15,16] ArFi is the lithography enhancement technique adopted to improve the resolution that replaces the air gap between the photoresist and the final lens with water (high refractive index). Moreover, by adopting various enhancement techniques and using multiple patterning process, the value of k_1 could also be successfully decreased and the achieved value was below 0.2 for photolithography at 193 nm light.[17] There has

been a continuous increase in the NA, as well. The highest NA (of 1.35) was achieved for water immersion lithography (ArFi).[18] The resolution limit reported for the water immersion lithography at 193 nm is ~36 nm for a single exposure.[19,20]

To continue printing smaller feature sizes and enhance further resolution, the semiconductor industry has exploited immersion lithography technology by using multi-patterning exposures process. But the fidelity of the final printed patterns using multiple ArFi exposures tends to degrade. Therefore, to overcome this, semiconductor industry introduced extreme ultraviolet (EUV) at 13.5 nm as the next-generation lithography and successor of the ArFi. Besides, a single EUV exposure offers better pattern fidelity and is simpler and cost effective than the multi-patterning processes.[18]

1.1.1 EUV Lithography

The very early picture of extreme ultraviolet lithography (EUVL) emerged in the 1980s while the commercialization of EUVL efforts only began around 1996.[21] EUV is in the soft X-ray band region and utilizes 13.5 nm light to expose the photoresist. EUVL allows the semiconductor industry to reach its objective of patterning feature sizes down to 10 nm and beyond in a cost-effective manner.[22,23] However, the big jump from conventional optical photolithography at 193 nm to EUV (13.5 nm) has posed numerous big challenges. Table 1.1 summarizes some of the key differences between ArFi lithography and its successor EUVL.

Table 1.1: Summary of the key differences between ArFi and its successor EUVL technology.

	ArFi	**EUV**
Wavelength	193 nm (6.4 eV)	13.5 nm (~92 eV)
Light source	ArF excimer laser	Sn plasma
NA	1.2-1.35	0.25-0.55
Optics	Transmissive lenses	Reflective multilayer
Ambient	water immersion fluid	vacuum

And, after years of efforts EUVL readiness for high-volume manufacturing for semiconductor devices was announced in 2018 by ASML,[18] and was moved into the production within Samsung and TSMC at the 7 nm technology node in 2020.[24]

1.2 Photoresists

1.2.1 Innovations in Photoresists

Photoresists are the fundamental materials used in the photolithography process in the semiconductor industry. Photoresists for g-line (at 436 nm) and i-line (at 365 nm) were developed in the 1950s and were mainly composed of diazonapthoquinone (DNQ) molecules as photosensitizer and novolak resin.[25] The solubility of DNQ in the aqueous base developing solvent is low and thus inhibits dissolution of the resin material, but after exposure (solubility switch) the exposed part of resin is soluble in the alkaline developer solution (Figure 1.2). However, this kind of resist material was not suitable for deep ultraviolet light (DUV) lithography applications as the absorption of DUV photons by novolak structure is high, consequently resulting in high absorption by the top part of the resist and underexposure of the bottom part.[26] Therefore, the resist material has to evolve to meet the industry requirements and chemically amplified resist (CARs) were introduced.

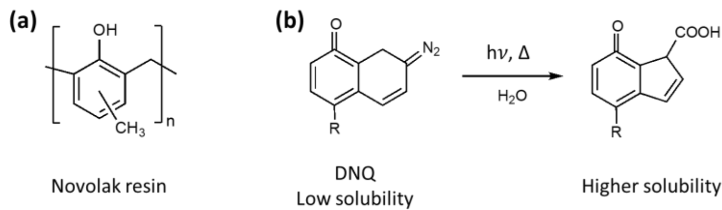

Figure 1.2: (a) Basic novolak resin structure for g-line and i-line photoresist, and (b) DNQ as photosensitizer and it's photoreaction after exposure. Adapted with permission from ref. 25. Copyright 1996 Wiley.

CARs were innovated at IBM[27] in the early 1980s for DUV technology. CARs are formulated polymer resin-matrix (reactant) loaded with photo-acid generator (PAG; an inactive dormant catalyst). The absorption of photons effectively results in the transfer of the aerial image into the latent image upon exposure by the generation of active acid by photochemical decomposition of the PAG. The generated acid further activates and catalyses the localized reactions responsible for the solubility switch in the polymer matrix.[28] This catalysis of the reaction occurs in the second step after exposure, during a post-exposure bake (PEB, heat) in the CARs.

As an example, the reaction mechanism for poly(4-hydroxystyrene) (PHS), a base polymer material for CAR, is shown in Figure 1.3. The -OH of PHS is blocked by a *tert*-butoxycarbonyl group (t-BOC). As a result, PHS has reduced solubility in

polar- usually alkaline aqueous solvents. But after the exposure and PEB, acid catalysed deprotection of this –OH group results in higher solubility of the localized exposed part (solubility switch). This ingenious concept of deblocking was developed by Wilson (IBM, USA), Ito (IBM, USA) and Frechet (University of Ottawa, Canada).[29] CARs have been proven as a class of photoresists that have led to high throughput in the semiconductor industry. Further, the high absorbance of PHS polymers at 193 nm led to the introduction of polymers platforms (such as acrylic based polymers) that are sufficiently transparent at the actinic wavelength.[30,31]

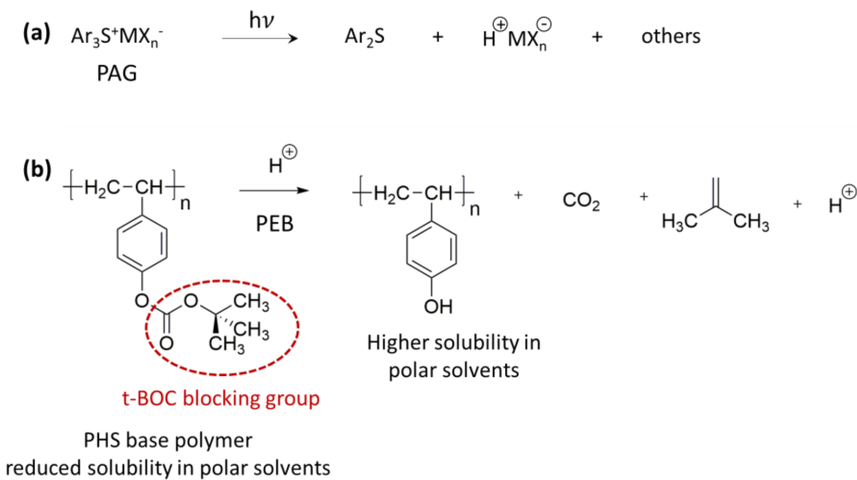

Figure 1.3: Positive-tone chemically amplified photoresist as an example for DUV lithography application using PHS as a base polymer; PEB = post-exposure bake. Adapted with permission from ref. 29. Copyright 1982 IEEE.

Based on the performance of CARs for DUV and their anticipated potential, researchers have studied their performance as EUV photoresists over the years.[32–34] However, photoresists with better sensitivity were needed for EUVL applications. Efforts were made by researchers to improve and tune the performance by increasing the acid generation efficiency of PAG by introducing electron-withdrawing groups on PAGs, changing the formulations or introducing the PAGs with better EUV absorption.[35,36] But traditional CARs had various limitations for the EUVL applications and are discussed in the next section.

1.2.2 Challenges for EUV Photoresists

With the big jump in the semiconductor industry from ArFi lithography to EUVL,

CARs for EUVL applications faced significant challenges. The fundamental mechanism by which the EUV photons are absorbed is very different from the mechanism of the previous conventional lithography wavelengths. With the shorter wavelength, EUV photons (13.5 nm, ~92 eV) are highly energetic in comparison to its successor of conventional longer wavelength (193 nm, 6.4 eV).

Typically, the molecular ionization potential of the resist materials is in the range of 6 to 14 eV and the energy of the EUV photons (~92 eV) surpasses this ionization potential by far. The absorption of EUV photons can result in the ionization of the material by ejection of an electron from the outer valence levels and this will lead to the generation of high-energy photoelectrons with kinetic energies of 78 to 86 eV and resultant holes in the thin film.[37–41] The high-energy photoelectron can further lose its energy in the nearby environment through various processes and one of the possible ways is to initiate further photoionization process, thus further generating secondary electrons in the thin film. Moreover, the absorption of EUV photons can also lead to the ejection of electrons from strongly bound core atomic orbitals (with higher EUV absorption cross-section). The primary photoelectron ejected in this case will thus possess relatively lower kinetic energy. However, the resultant molecular ion left behind after ionization will have high residual energy. It can release its energy by different relaxation processes, among which are the ultrafast Auger ionization, which can lead to the generation of multiple electrons as well. And subsequent relaxation can lead to chemically reactive species such as radical cations in the thin film.[42]

The details of these chemical events are complex and not well understood. Contrary to this, the absorption of photons of the conventional wavelength of light (365 to 193 nm) by the resist is well understood, since the energy of the photon is below the molecular ionization potential of resist and the absorption of photon will only lead to the excitation of the molecule to electronically excited states, often described in a simplified way by the promotion of an electron from a filled molecular orbital to an unoccupied orbital.[43] While the mechanism for interaction of the resist materials with the longer wavelengths photons is well understood, the challenge is to grasp the interaction of EUV photons with resist materials, making this currently an active research area.

One of the important resist property to be considered for lithography applications is the absorption of the imaging light.[44] EUV absorption by photoresist is strongly dependent on the atomic composition of the material. However, the traditional CARs have mainly C, H and O as the constituting elements and are mostly transparent to the EUV photons (Figure 1.4). Therefore, the elemental composition for the resist material must be considered for the EUVL application and elements with higher absorption for EUV photons must be incorporated. Table 1.2 highlights some of the key differences in ArFi and EUVL photoresists and photochemistry.

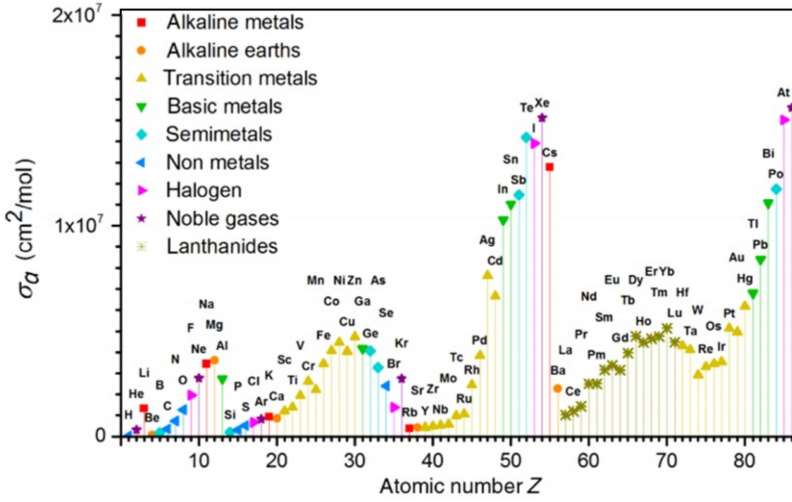

Figure 1.4: Absorption coefficient of elements with atomic number (Z) from 1 to 85 for EUV photons (13.5 nm, 92 eV). Adapted with permission from ref. 44. Copyright 2018 SPIE.

The absorption properties of the resist thin films can be described using conventional definitions. If I_0 is the incident light intensity on resist thin film, and I is the intensity of the light after it has passed through the resist thin film, the transmission T and absorbance A are defined as

$$\text{Transmission } T = {}^{I}/{}_{I_0} \tag{1.2}$$

$$\text{Absorbance } A = -ln\, T \tag{1.3}$$

$$\text{Absorption fraction} = \frac{I_0 - I}{I_0} = 1 - T, \tag{1.4}$$

The absorbance is related to the absorption cross section, and the number of absorbing species in the light path of length l. In solution, we use the familiar Lambert-Beer law $A = \varepsilon c l$ where ε is the molar absorption coefficient and c is the concentration. In thin films, the absorbance is commonly quantified by the absorption coefficient α (μm^{-1}) and is defined as $A = \alpha l$ with layer thickness l in µm.

Table 1.2: Summary of the key differences in ArFi and EUV resist material and photon-induced chemistry.

	ArFi	EUV
Ionization of resist	No	Yes
Photon absorption chemistry	*Photochemistry*: Excitation to electronically excited states described using molecular orbital occupations	*Radiation chemistry*: Photon absorption is described as an atomic property and results in ionization (from valence or core orbitals)
Resist material	CARs: formulated polymer resin-matrix with PAG.	Incorporation of elements (such as metals) to increase EUV absorption

Developing a resist platform for lithography having a good trade-off between transparency and absorption of photons is important. The resists materials should be transparent enough for the photons to obtain a straight sidewall in patterned features through the whole thickness of the thin film.[45] However, the increasing demand for the smaller features has led to a decrease in the film thickness to maintain the necessary aspect ratio and prevent pattern collapse.[46] Therefore, with a decrease in the thin film thickness, a sufficient increase in the EUV absorption is also required.[47] The present target for printing dense pattern of 20 nm, however, involves thinner thin films (~20-30 nm). The absorption coefficients of organic-based resists or low-density polymers (used for conventional wavelength applications) for EUV photons are ~5 μm^{-1} which makes them transparent towards EUV photons. The optimal absorption coefficient (α) for a thickness of 20 to 30 nm with 70% transmittance will be 18 to 12 μm^{-1}, respectively. Hence, the incorporation of elements in resist material with a higher EUV absorption coefficient is required.[48]

Initial studies recommended fluorine incorporation into the resist material to increase EUV photon absorption.[49–51] In 2012, metal-based resists were suggested to enhance the EUV absorption since most of the metals have a high EUV absorption.[52,53] Incorporating metals into the resist material was also demonstrated to provide better etching resistance.[54] Therefore, metal-based resists became a potential candidate for EUVL applications and the study of hybrid (inorganic-organic) systems is currently a very active research area. Figure 1.4 shows the graph of the absorption cross sections of elements from 1 to 85 for EUV photons (92 eV). Studies have been done on various resists systems incorporating different metals: Sn, Hf, Zr, Co, Pt, Pd, Zn, Sb, Bi, Te and more.[55–60] Despite the progress in the past decade, it is still a challenge to design the

materials for EUVL that can meet the industrial targets. The overall performance of a photoresist can be evaluated by using the so-called RLS trade-off: resolution (R< 20 nm), line width/line edge roughness (LWR/ LER) of printed patterns (L< 20%) and sensitivity (S< 20 mJ/cm^2).[61,62]

1.2.3 Zinc-based metal oxoclusters

Among hybrid materials, metal oxoclusters (MOCs) have emerged as potential candidates for EUVL applications. They are composed of small (~1-2 nm) multi-metal oxo-cores surrounded by ligands (organic shell). A monodisperse particle size is an inherent property due to the well-defined molecular nature of these compounds. The oxo-core of metal is anticipated to provide high absorption of EUV photons, and the organic ligand shell is mainly responsible for the solubility switch mechanism upon light irradiation (Figure 1.5 (a)).[63] The ligand shell of such systems is dynamic in nature, which provides the flexibility to exchange the ligands with other ligands providing specific functionality in a simple synthetic approach.[64–66]

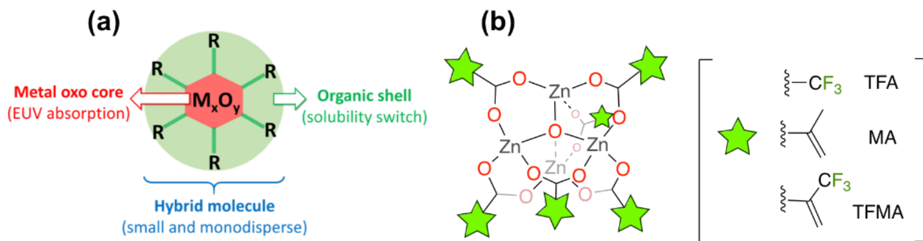

Figure 1.5: (a) Basic schematic representation of metal-based oxoclusters, and (b) Zn-based oxoclusters having the same oxo-core with different ligands (TFA, MA and TFMA) studied in this thesis.

The absorption coefficient of Zn for 92 eV photons is ~13.5× that of C and ~3.7× that of O.[67] In addition, Zn metal has 3p core orbitals with binding energies close to the EUV energy (92 eV), which may contribute towards better EUVL performance via resonant photoabsorption in the resist material.[42] Previous study on Zn-based resist: zinc-oxide nanoparticle photoresists and zinc-clusters inspired from the metal-organic framework (MOF-2) has been reported for applications in EUVL as well.[68–70] The Zn-oxoclusters studied in this thesis comprise a tetranuclear core having 4 Zn atoms in a tetrahedral geometry bridged by an O in the centre (μ_4-oxo) in their inorganic core. They are surrounded by 6 carboxylate ligands that bridge two Zn atoms (Figure 1.5 (b)).[71]

1.3 Outline and scope

The thesis focuses on the evaluation of the performance of Zn-MOCs for EUVL lithography applications, and on the chemical reaction mechanisms involved. The Zn-MOCs studied in the thesis were synthesized from a commercially available Zn-oxocluster with the trifluoroacetate (TFA) ligand. By ligand exchange, methacrylate (MA) and 2-trifluoromethylacrylate (TFMA) ligands were introduced in the Zn-MOCs . The patterning capability of Zn-MOCs as EUV photoresists was evaluated using the EUV-interference lithography tool at the Paul Scherrer Institute, Switzerland. Chemical changes induced into the resist material responsible for solubility switch upon EUV irradiation were studied using a combination of various spectroscopy tools.

In **Chapter 2,** the chemical changes in $Zn(MA)_5(TFA)_1$ oxocluster upon thin film deposition from its bulk and due to ageing under different atmospheres in the thin film is investigated, using a combination of spectroscopic studies. Additionally, the sensitivity of the Zn oxocluster and its reproducibility for EUVL applications was also investigated. New developers that can have specific interactions with this type of hybrid materials were explored in order to improve the contrast of the material.

In **Chapter 3,** the results of Chapter 2 are expanded and the capability of $Zn(MA)_5(TFA)_1$ as EUV photoresist is explored. The chemical changes that this Zn-oxocluster undergoes in thin films upon EUV irradiation were studied by a combination of ex situ UV-vis, FTIR and XPS spectroscopy. It is shown that radical-induced polymerization of the acrylate C=C bonds is one of the main factors responsible for the solubility change.

In **Chapter 4,** the photon-induced fragmentation of photoionized $Zn(MA)_5(TFA)_1$ in the gas phase in the UV/VUV (4 to 14 eV) range is investigated using atmospheric pressure photoionization (APPI) mass spectrometry. This study assisted in gaining insights into the reaction pathways that this molecular resist can follow after the ionization events.

In **Chapter 5,** electron-induced chemistry in $Zn(MA)_5(TFA)_1$ oxocluster responsible for the solubility switch in EUV photoresists is explored. Electron beams at 80 eV and 20 eV that mimic the photoelectrons and low-energy secondary electrons (LESEs) generated in thin films after EUV exposure were used in the experiments. The chemical changes in the resist thin films were monitored by recording mass spectra of desorbed species upon electron beam exposure. In combination, reflection absorption infrared spectroscopy (RAIRS) was used to study chemical changes before and after electron beam exposure with doses comparable to EUV.

In **Chapter 6,** fluorine-rich Zn oxoclusters are studied. The presence of fluorine in a resist material is known to increase the EUV photon absorption and is thus

consequently expected to enhance the sensitivity. The fluorine in the oxocluster was introduced via the fluorine-rich ligand TFMA in the organic shell, preserving the Zn-oxo core and the terminal double bonds (for solubility switch, studied in Chapter 3). In this fashion, the effect of the organic shell on the photoresist's performance was studied.

Overall, our study of the EUVL performance of the Zn-based MOCs featuring organic ligands sheds light on the importance of the selection of proper ligands for an optimal design of hybrid EUV resists and provide pertinent mechanistic insights into the EUV-induced chemistry in the Zn-MOCs responsible for the solubility switch using combination of spectroscopy techniques.

2

STABILITY STUDIES ON SENSITIVE ZINC-BASED OXOCLUSTER: EUV PHOTORESIST*

Abstract

Hybrid inorganic-organic materials have emerged as promising candidates for EUV resists. For their performance in EUV lithography, knowledge of their stability when deposited as thin films is essential. Herein, we investigate whether the molecular structure of novel Zn-based metal oxoclusters is preserved upon thin film deposition and study the ageing process of the thin film under different atmospheres since these chemical changes affect the solubility properties of the material. A hybrid cluster that combines the high EUV photon absorption cross-sections of zinc and fluorine with the reactivity of methacrylate organic ligands was synthesized. The structural modifications upon thin film formation and after ageing in air, nitrogen, and vacuum were studied using a combination of spectroscopic techniques. Preliminary studies on the lithographic performance of this novel material were performed by EUV interference lithography. The Zn-based compound undergoes structural rearrangements upon thin film deposition as compared to the bulk material. The thin films degrade in the air over 24 hours, yet they are found stable for the duration and conditions of the lithography process and show high sensitivity. The easy dissociation of the ligands might facilitate hydrolysis and rearrangements after spin-coating, which could affect the reproducibility of EUV lithography.

*Published as: N. Thakur, L.T. Tseng, M. Vockenhuber, Y. Ekinci, and S. Castellanos, Journal of Micro/Nanolithography, MEMS, and MOEMS, 2019, 18(4), 043504. DOI: 10.1117/1.JMM.18.4.043504

2.1 Introduction

Photoresists materials are crucial for the semiconductor industry since they mediate the transfer of information from an optically projected pattern onto a substrate where the actual circuitry of processor chips and memory devices are built.[10,70] To keep following Moore's law, which requires the fabrication of patterns with ever-smaller critical dimensions, EUV lithography, using radiation of 13.5 nm wavelength, is seen as the most suitable successor to the state-of-the-art ArF immersion photolithography (193 nm).[72,73] However, this transition has led to critical challenges for the development of suitable EUV photoresists.[51,74–77] For adequate lithography performance, resists should simultaneously satisfy the industrial requirements of resolution (< 10 nm) and line-width roughness (LWR $< 15\%$) at sustainable production costs. The latter point thus demands that the photoresists have high sensitivity and can yield nano-patterns at doses as low as 20 mJ/cm^2 or below.[65,70,78,79]

Although the standard platform for resist materials has been polymer-based chemically amplified resists (CAR's), EUV lithography technology requires the development of entirely new resist platforms.[62,70,80,81] As future nodes are continuously decreasing, the size of traditionally used polymers in photoresists has become a critical point especially with regard to linewidth roughness.[82] Furthermore, increasing EUV radiation absorption by the resist material is now one of the most important design criteria towards optimizing resists performance.[83] These performance targets require research on new materials that incorporate elements with high EUV photon absorption cross-sections and, at the same time, are composed of small units consistent with future resolutions targets.[62,84–86]

Metal oxoclusters are hybrid molecular compounds[63,65] and hold great potential as resists platforms for EUV lithography applications. By choosing the right metal component, they can meet the desired properties for EUV photon absorption while offering intrinsically small and homogeneous size (monodisperse) due to their molecular nature.[62,65,87] In the present contribution, the elucidation of a simple and versatile preparation method of a new Zn-based metal oxocluster, as well as the stability and sensitivity of the resulting material towards EUV radiation are explored. Recently, molecular materials based on Zn have been investigated and have shown promising results.[68,69,85] In our approach, a denser Zn metallic oxo core is used as the inorganic building block in order to enhance the EUV absorbance of the material. The organic ligands surrounding the inorganic EUV-absorbing core are envisioned as the main factor defining the solubility properties.[63] In addition, the organic ligands play a major role in the reactivity of the material. The organic shell is thus responsible for the switching of the solubility properties of the material upon EUV exposure, which enables patterning.[88]

In this study, we focus on trifluoroacetate (TFA) and methacrylate (MA) ligands as components of the organic shell around a tetranuclear Zn oxo core. The presence of fluorine in the resist material is known to increase the EUV photon absorption.[47,89] On the other hand, the introduction of MA ligands having a terminal double bond is anticipated to provide an effective solubility switch arising from the cross-linking of these double bonds.[65,90] The shelf life of Zn-based oxoclusters featuring simultaneously both types of ligands, MA and TFA, and its response towards EUV high energy radiation were investigated. Developers that have specific interactions with this type of hybrid materials were explored to improve the contrast of the material. These investigations highlight the importance of understanding the chemistry of the resist at the molecular level to optimize their performance.

2.2 Materials and Methods

2.2.1 Materials

All chemicals ($Zn_4O(TFA)_6$ precursor, CAS 1299489-47-6; methacrylic acid, CAS 79-41-4) were purchased from Sigma-Aldrich and were used without further purification. All the used solvents were reagent grade.

2.2.2 Synthesis of photoresist: Zn(MA)(TFA)

Methacrylic acid (MAA, 110 mg, 1.247 mmol, 12.0 eq) and $Zn_4O(TFA)_6$ (100 mg, 0.103 mmol, 1.0 eq) were dissolved in chloroform (10-15 ml) and left stirring for 2.5 hours at 40°C. The solvent was then evaporated, and the oily residue was precipitated by washing with toluene (5-10 ml). The process was repeated for 5-6 times to remove excess MAA in the reaction mixture and obtain a solid white compound (Figure 2.1).

^{1}H NMR (300 MHz, DMSO-d_6) δ: 1.83 (3H, $-CH_3$), 5.34 (1H, $=CH_2$), 5.83 (1H, $=CH_2$) ppm

^{13}C NMR (300 MHz, DMSO-d_6) δ: 19.36 ($-CH_3$), 115.04 (s, $-CF_3$), 122.02 ($=CH_2$), 139.93 (-C=), 158.57 (s, -COO, TFA), 173.00 (-COO, MA) ppm

^{19}F NMR (300 MHz, DMSO-d_6) δ: -73.94 ($-CF_3$) ppm

All NMR spectra are shown in Appendix I.

FTIR: 523 (w, ν_{as} Zn-O-Zn), 628 (s, COO angle bending), 1205-1155 (m, ν C-F), 1238 (m, coupled rocking $=CH_2$ and ν C-C), 1300-1500 (s, coupled CH_x deformations and ν_s COO), 1543 (s, ν_{as} COO, bonded acid MA), 1606 (m, COO H-bonded MA), 1653 (s, ν_{as} C=C), 1687 (s, ν_{as} COO bonded TFA), 1735 (w, ν_{as} COOH non-bonded TFA), 2929-2987 (w, ν $-CH_3$), 3022 & 3105 (s, ν $=CH_2$), 3200-3600 (b, ν_s O-H) cm^{-1}.

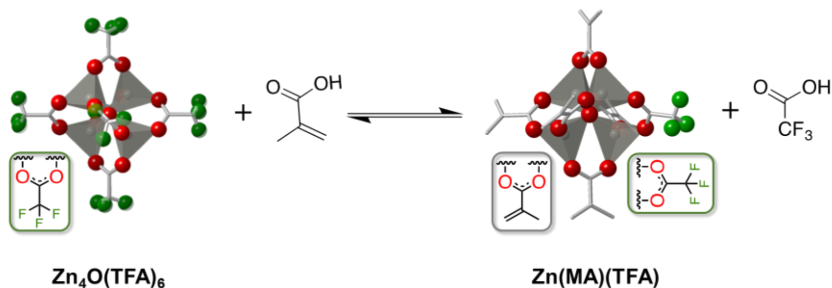

Figure 2.1. Scheme of the Zn(MA)(TFA) synthesis by ligand exchange reaction. In the three-dimensional representation, grey tetrahedra represent the coordination geometry of the Zn^{2+} atoms (grey spheres in the center), red spheres represent oxygen atoms, green spheres represent fluorine atoms, and grey sticks are chemicals bonds. Lewis structure below gives the details of the ligands' structure.

2.2.3 Characterization of the bulk material

NMR was recorded using a Bruker AV-400 NMR spectrometer using deuterated dimethylsulfoxide (DMSO-d_6) as a solvent. FTIR was performed using a Bruker ALPHA FTIR spectrometer. Mass spectra were collected on an AccuTOF LC, JMS-T100LP Mass spectrometer (JEOL). Thermogravimetric analysis (TGA) was performed using a NETZSCH thermogravimetric analyser in an Al_2O_3 crucible and heating was performed from 35 °C to 700 °C at 10 K/min in an N_2/O_2 atmosphere. Elemental analysis was performed by Mikroanalytisches Labor Kolbe, Germany for elements Zn, Carbon (C) and Fluorine (F) in the synthesized compound Zn(MA)(TFA).

2.2.4 Thin film preparation

Zn(MA)(TFA) resist solution 2% (w/v) was prepared in chloroform ($CHCl_3$), and propylene glycol methyl ether acetate (PGMEA), 9:1 v/v followed by filtration using a 0.22 µm PTFE filter after sonication for 4 minutes. All thin films for analysis and lithography were prepared by spin-coating the resist solution at 2100 rpm for 30 s, using an acceleration of 3000 rpm/s. Samples for UV-vis absorption spectroscopy were spin coated on quartz substrates of 525 µm thickness and samples for FTIR spectroscopy were spin coated on a double side polished Si-wafer of 200 µm thickness. The thickness of the resist thin films spin coated on silicon and quartz substrates was in the range of 25 nm to 35 nm, as measured by atomic force microscopy (AFM). Post application baking (PAB) was applied 90 °C/ 30 s to remove excess residual solvent.

Sample preparation for the EUV absorption coefficient measurement was done using silicon nitride (SiN_x) membranes purchased from Norcada Inc. as substrates (100 nm thickness, membrane window of 7.5 × 7.5 mm^2). A thin film

of the resist was deposited on the membrane by spin coating following the same parameters as for Si substrates for lithography experiments. The thickness measured by ellipsometry was 43 nm.

2.2.5 Characterization of thin films

UV-vis absorption spectroscopy was performed using a Shimadzu UV2600 spectrophotometer and FTIR spectroscopy of the thin films was performed in transmission mode under vacuum in a Bruker Vertex 80v spectrometer. The thickness of the thin film spin coated on SiN_x was measured by using J.A. Woollam- VB-400 VASE Ellipsometer. The spectral range used was 250 nm to 1000 nm. The optical constants of the resist material were first measured independently on a sample of known thickness deposited on a Si substrate.

2.2.6 EUV exposure and post-exposure analysis

Open frame exposures were performed for a wide range of doses by exposing 1.7 × 1.7 mm^2 areas to EUV light at 13.5 nm. These exposures were performed at the SLS XIL-II beamline in the Paul Scherrer Institute (PSI), Switzerland.[91] The detail of the experimental set-up at the XIL-II beamline for absorption coefficient measurement has been described in previous studies.[48,92] A pinhole of 30-µm diameter and a square open frame mask of 0.5 × 0.5 mm^2 were used in this measurement. The absorption of EUV light from the SiN_x membrane was calibrated by measuring the photocurrent passing through a clean SiN_x membrane as a reference photocurrent. The transmittance of the resist materials is given by the ratio of the measured photocurrent of the resists and the reference photocurrent.

Propionic acid, acetylacetone (acac), and acetic acid diluted in $CHCl_3$ were used as developers. Thin film thickness was measured by Atomic Force Microscopy (AFM), using a Bruker Dimensions Icon. For patterning line-space (L/S) patterns, a transmission mask was used. High-resolved SEM images were recorded using FEI Verios 460 system.

2.3 Results and Discussions

2.3.1 Determination of the organic shell composition

The Zn oxocluster (Zn(MA)(TFA)) was synthesized by ligand exchange from the commercially available oxo[hexa(trifluoroacetato)]tetrazinc $Zn_4O(TFA)_6$ (Figure 2.1). The starting material comprises a core of four Zn atoms bridged by one O atom (μ_4-O) and six TFA ligands that bridge two Zn atoms through the carboxylate group.[93,94] Since this reaction proceeds in equilibrium due to the competitive binding of the two types of carboxylate ligands, methacrylic acid is added in excess to favor the shift of the equilibrium to the right side of the

chemical equation and have a high abundance of MA ligands in the shell of the synthesized product Zn(MA)(TFA).

NMR and FTIR spectroscopic analysis performed on the synthesized bulk oxocluster evidenced the presence of both TFA and MA ligands (see section 2.2.2). To confirm whether the tetranuclear oxocluster is preserved during ligand exchange, mass spectrometry experiments were performed. This is an ideal technique since Zn metal has different naturally occurring isotopes, which provides the mass spectrum with a unique characteristic isotopic pattern distribution arising from the four Zn atoms in the oxocluster. The spectra obtained using different solvents for the vaporization step are shown in Figure 2.2.

The isotopic distribution observed in the mass spectra was in concordance with the expected one for a tetranuclear Zn oxocluster (Zn_4O). Two peak envelopes in the mass regions m/z 778-790 and m/z 806-818 were detected, which matched the mass of a Zn_4O cluster with five MA ligands and the Zn_4O cluster with four MA and one TFA ligands complexed with two acetonitrile molecules, $[Zn(MA)_5 + 2CH_3CN]^+$ and $[Zn(MA)_4(TFA) + 2CH_3CN]^+$, respectively (Figure 2.2(a)). Such species would result from the loss of a trifluoroacetate or a methacrylate ligand in the Zn(MA)(TFA) material. The complexation of acetonitrile to the cluster was confirmed by recording mass in deuterated acetonitrile-d_3, which shifted the envelope of peaks with the specific isotopic distribution by +6 *m/z* units (Figure 2.2(b)). Furthermore, when the spectrum was recorded using methanol as the carrying solvent, the molecular peak was observed at 702 *m*/z, corresponding to $[Zn(MA)_5]^+$ (Figure 2.2(c)). These assigned peaks in the mass spectra indicate that in the synthesized Zn(MA)(TFA), MA is the most abundant ligand in the cluster. It can therefore be concluded that upon ligand exchange reaction most of the TFA ligands of the precursor cluster in the organic shell were substituted by MA ligands while keeping the Zn-oxo core unaltered.

The composition of the organic shell (TFA/MA ratio) was further defined by elemental analysis. The results (experimental %Zn: 23.86, %C: 37.24, %F: 7.29) were assigned to the chemical formula $[Zn_4O_{18}C_{31}H_{37.5}F_{4.5}]$ (theoretical %Zn 25.03, %C 35.61, %F 8.19), which would correspond to an average of 7 MA and 1.5 TFA ligands per tetranuclear cluster. This assignment indicates the presence of an excess of non-bonded carboxylic acids in the bulk material, in agreement with FTIR. The occlusion of carboxylic acids in the crystals formed by metal oxoclusters is a common phenomenon.[93,95,96]

The residue detected experimentally in TGA was 32% (Figure 2.3), and is in good agreement with the calculated ZnO residue that results from the combustion of the compound with molecular formula $Zn_4O_{18}C_{31}H_{37.5}F_{4.5}$ (31%).

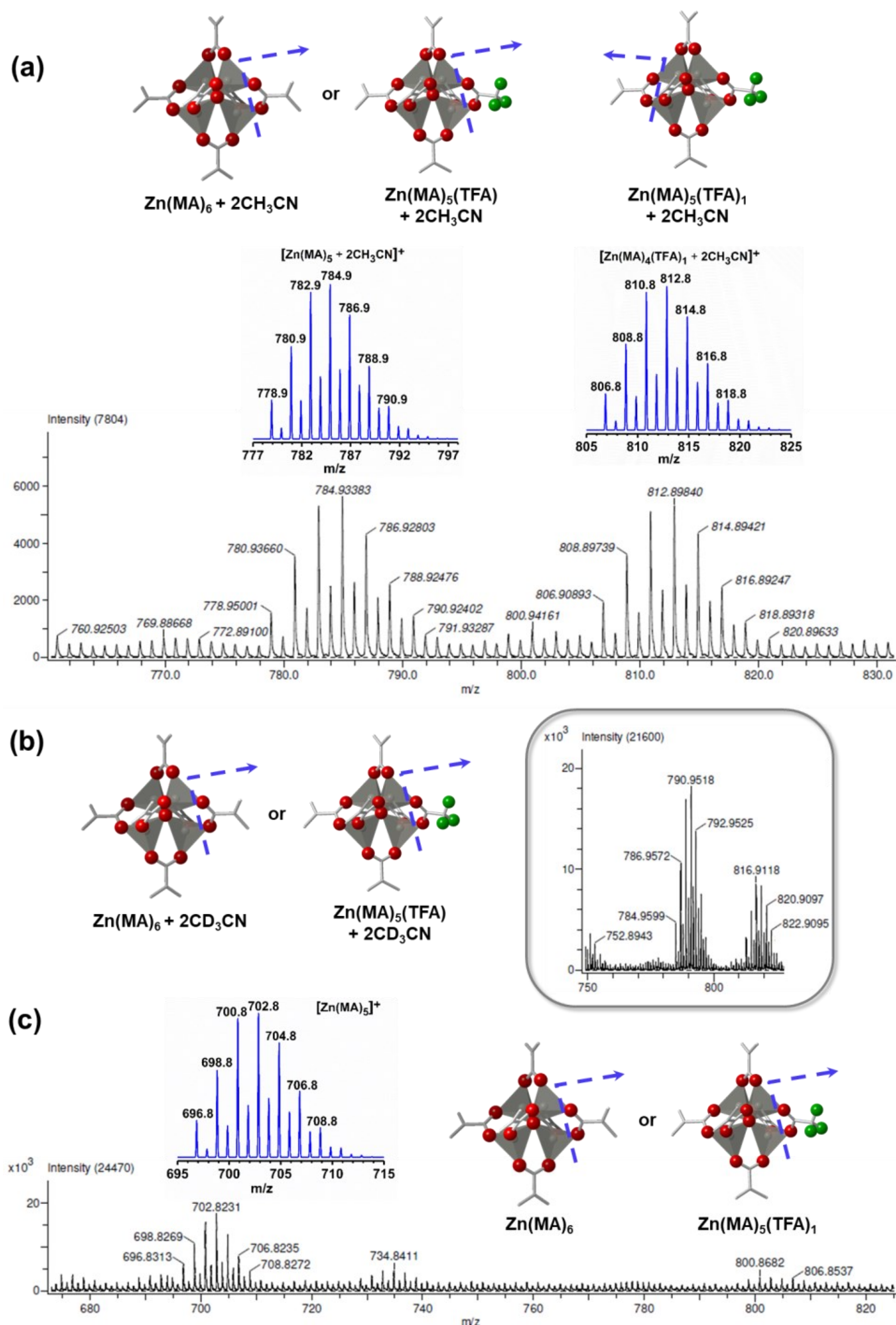

Figure 2.2. Experimental (black) and simulated (blue) mass spectra of Zn(MA)(TFA) oxocluster in solvent (a) acetonitrile, (b) acetonitrile-d$_6$, and (c) methanol.

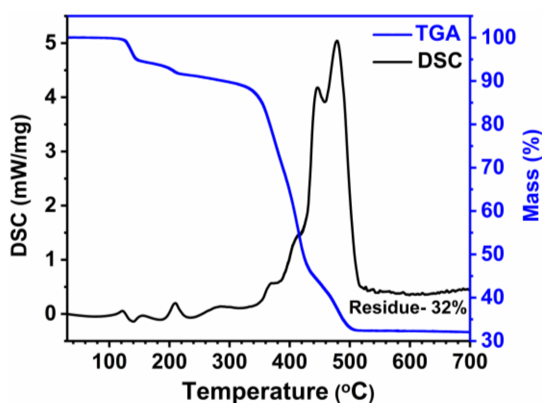

Figure 2.3. TGA of Zn(MA)(TFA) powder sample (bulk material).

2.3.2 Stability Studies

Chemical bonds between carboxylate and metal cations are rather labile, i.e. the metal-ligand bond can dissociate at lower energy, especially in the presence of chemical species that can compete in the coordination of the metal, such as water.[97] Therefore, it is crucial to study the stability of the newly synthesized Zn-cluster both in the bulk material and when deposited as a thin film for the nano-lithographic application. For this purpose, the chemical composition of the bulk material and the thin films was monitored under different atmospheres by spectroscopic means.

The stability of the bulk material was studied by FTIR spectroscopy (Figure 2.4). A significant decrease in the intensity of O-H band (broad band 3750-2800 cm^{-1}) and of the peak assigned to the ν_{as} of non-bonded TFA (1725 cm^{-1}) was observed in the normalized FTIR spectra after 2 months storage in low moisture conditions. These indicate the loss of free trifluoroacetic acid over time. The broadening of the COO stretching band at 1605 cm^{-1} also suggests changes in the environment of carboxylates over this period of time. Such changes together with the decrease of the peaks in the 500-750 cm^{-1} region, where bending modes of the COO are expected, suggest that some bonded ligands might be lost and/or change their coordination geometry. This might result from partial hydrolysis and/or rearrangement of the organic shell. Yet, the presence of the characteristic Zn-O-Zn stretching band of the tetranuclear oxo core[98] indicates that the degradation was only partial.

In addition to the stability of the bulk material, it was crucial to investigate the molecular structure of the oxoclusters when deposited as a thin film and the effect of different atmospheres present in the lithographic process. The stability of the thin film was monitored at ambient conditions in air, nitrogen atmosphere

(glovebox), and high vacuum (<10^{-6} mbar). The latter is highly relevant since EUV exposure is performed under high vacuum (<10^{-6} mbar), which may act as a driving force for ligands loss and undesired aggregation of the inorganic clusters.[90,99] After exposing the thin films to different conditions, the thin films were analyzed by UV-vis absorption and FTIR spectroscopy.

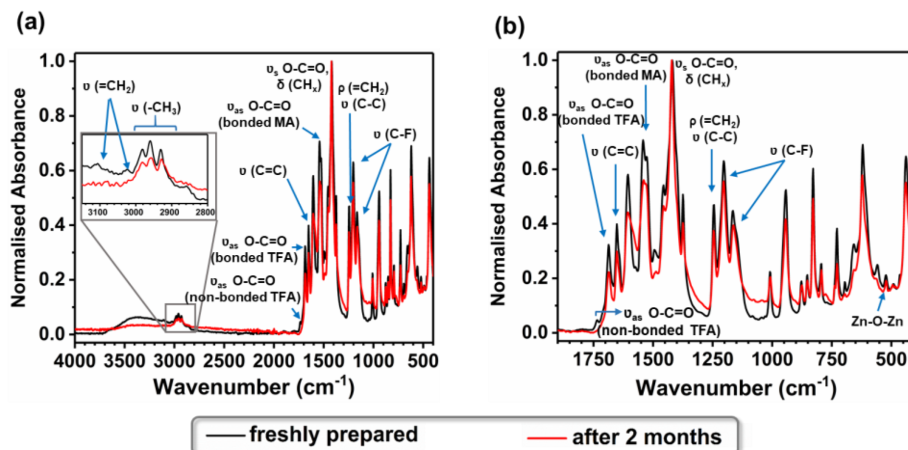

Figure 2.4. (a) Normalised FTIR spectra of freshly synthesized oxocluster Zn(MA)(TFA) and after 2 months (in moisture free conditions); inset of FTIR in the region of ν $-CH_3$ and ν $=CH_2$, and (b) zoom of the spectral region from 1780 to 400 cm^{-1}.

First, the composition of the thin film right after deposition by spin-coating was investigated (Figure 2.5). The FTIR absorption spectrum of Zn(MA)(TFA) deposited as a thin film shows that the extra carboxylic acids initially present in the bulk crystalline material are lost during spin-coating since the bands at 1725 cm^{-1} (assigned to the COOH asymmetric stretching of the non-bonded TFA) and at 1606 cm^{-1} (tentatively assigned COOH of MAA bonded to the Zn cluster in a weak manner[100]) were not observed in the thin film FTIR spectrum. The presence of bonded MA was evidenced by the peak at 1543 cm^{-1} (COO bidentate asymmetric stretching), the envelope at 1500-1300 cm^{-1} (various chelating and bridging COO stretching modes coupled to asymmetric and symmetric CH_x deformations modes), and the vibrational modes corresponding to ν_s C=C at 1653 cm^{-1} (observed as a shoulder) and the peak at 1238 cm^{-1} corresponding to coupled rocking $=CH_2$ and ν C-C.[99] The presence of coordinated TFA was indicated by the intense peak 1675 cm^{-1} (COO asymmetric stretching's of bonded TFA, which shifts compared to the powder sample, 1687 cm^{-1}) and the characteristic C-F stretchings at 1155 and 1205 cm^{-1}.

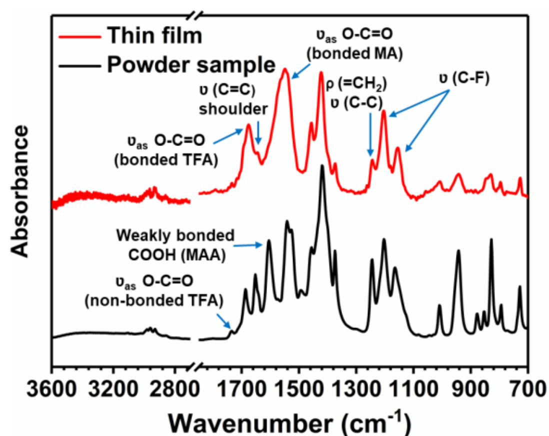

Figure 2.5. Normalised FTIR absorption spectra of Zn(MA)(TFA) as powder and deposited as thin film on Si substrate.

The stability of Zn(MA)(TFA) oxocluster thin films can readily be monitored by UV-vis spectroscopy. The π-π* electronic transition of the terminal methylene of the MA ligand provides a characteristic signal at ~198 nm which can be used to monitor changes in the thin film. The UV-vis spectrum of the freshly spin coated thin film was compared to the spectra for same thin film after certain intervals in air atmosphere (Figure 2.6(a)). The spin coated thin film was stable for at least 4.5 hours while bleaching was clearly observed after 24 hours. Similarly, the stability was monitored after applying high vacuum ($<10^{-6}$ mbar) for 1 hour, resulting in a slight decrease in the absorption band and suggesting that vacuum did not induce a considerable loss of ligands. Another measurement was performed after leaving the latter sample for 3.5 hours at room temperature, which showed negligible change in the absorption band during this period of time (Figure 2.6(b)).

In order to further investigate specific changes in the organic ligands, FTIR of the thin films was recorded. For this purpose, spectra of the freshly prepared sample and of samples after 24 hours in different atmospheres were recorded. By comparing the normalised absorption spectra (Figure 2.6(c)), a slight decrease in the intensities of the peaks at 1421 cm^{-1} (for CH_2 deformations combined with COO symmetric stretchings) and of the small shoulder at 1238 cm^{-1} (due to rocking of vinyl methylene group $=CH_2$ and C-C stretching of neighboring groups)[99] is observed for the sample kept in N_2. Yet, a more dramatic decrease of these bands and broadening of the peaks at 1675 and 1543 cm^{-1} was detected for the sample kept at room conditions, accompanied by a relative increase in the broad band at 3100-3600 cm^{-1}, typical for O-H stretching (Figure 2.6(c)).

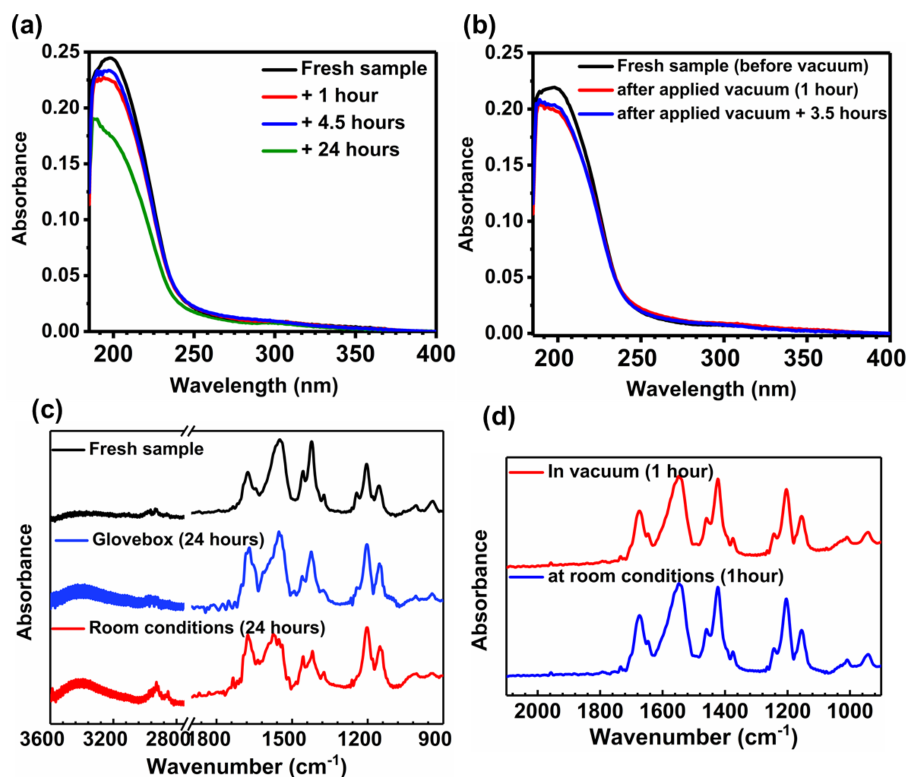

Figure 2.6. Monitoring stability of the thin films of Zn(MA)(TFA) photoresist by: (a), (b) Uv-vis absorption spectra, and (c), (d) FTIR absorption spectra.

These experiments suggest that moisture in the air can lead to a partial hydrolysis of Zn(MA)(TFA) cluster. Also, polymerization of the terminal double bond could also be favored by the natural light available at room conditions and in N_2 atmosphere. FTIR spectra of the sample before and after high vacuum (1 hour) showed more modest changes. The ratio between the peak associated to the $=CH_2$ rocking in MA (1238 cm^{-1}) and the peaks assigned to C-F stretching modes in TFA (1205-1155 cm^{-1}) decreased slightly. Also the intensity of the envelope in the 1500-1300 cm^{-1} related to MA was lower. In parallel, a slight decrease in the absorption band at 198 nm was observed after 1 hour of vacuum. These spectroscopic signs could indicate a small degree of MA ligand loss or cross-linking of the terminal double bonds in the MA ligands (Figure 2.6(d)). Subsequent monitoring of the same sample after one hour at room conditions was in agreement with the previous UV-vis spectroscopy studies and indicated that no significant hydrolysis occurred within this time frame.

In light of the spectroscopic changes, the storage of the thin films in different atmospheres for long periods of time could have an important effect on the patterning capabilities of the resist. Here we focused on working in time scales that guaranteed the integrity of the material. Nevertheless, it should be noticed that evolution of the thin film in vacuum could have an effect on the lithographic performance if there are idle times before exposure. Such effect could affect similar inorganic resists systems as well.

2.3.3 Sensitivity towards EUV light and lithography performance

%Transmittance (T_x) of resist was measured experimentally by using synchrotron EUV light at the Paul Scherrer Institute. The linear absorption coefficient, α, for Zn(MA)(TFA) was calculated after determining the thin film thickness by ellipsometry as per Beer-Lambert law as:

$$T_x = e^{-\alpha d} \tag{2.1}$$

and α value of 12.4 ± 0.4 μm^{-1} was found for the thin film of Zn(MA)(TFA). This is close to the reported values for tin-based resists, where the α ranges from 15 and 19 μm^{-1}, while for organic photoresists is typically ~5 μm^{-1}.[48,83,92] As a reference value, the theoretical linear absorptivity was calculated for this material. To do so, we considered that the material was consisting of Zn-tetranuclear clusters with 5 MA and 1 TFA ligands (molecular formula $C_{22}H_{25}O_{13}Zn_4F_3$) and we approximated its density (2.4 g/cm^3) assuming that the molecular packing was the same as for an analogous tetranuclear cluster consisting of 6 acetate ligands, $Zn_4(OAc)_6$ (1.9 g/cm^3)[101] and correcting for the different molecular weights ($\rho_1/MW_1 = \rho_2/MW_2$). The obtained α value using these assumptions was 14.6 μm^{-1}.

In addition to photon absorption and the chemistry triggered by EUV photons, the interaction of the developer with the unexposed and exposed resist largely defines the contrast (γ) of the lithographic process. Therefore, choosing the right developer is crucial to obtain good γ values and understanding the molecular structure of thin films can greatly assist in the choice. Our first attempt was to use $CHCl_3$ as developer, which is also used as solvent for cluster synthesis and thin film deposition. However, this solvent could not re-dissolve the thin film resulting from the spin-coating of the material on the silicon substrate. This is further evidence that upon thin film formation, some changes occur in the material compared to its structure when it is isolated as a crystal (most likely loss of excess of non-bonded acids, as seen in FTIR, and potentially other structural re-arrangements) such that the solubility in $CHCl_3$ decreases.

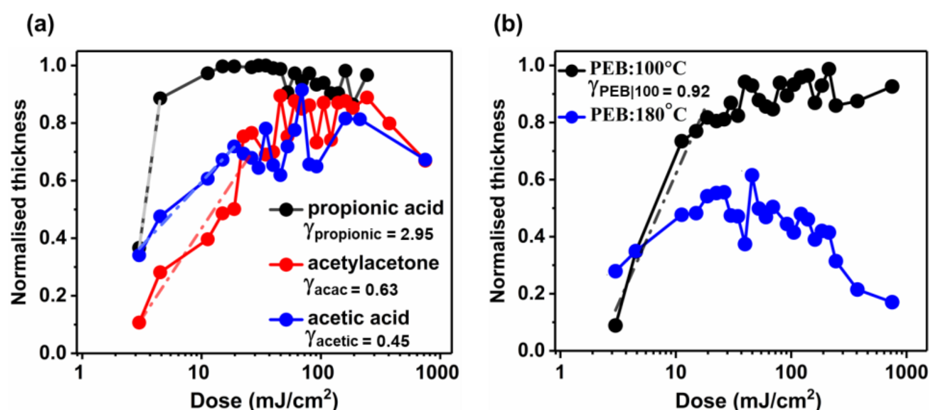

Figure 2.7. Contrast curves of EUV exposed Zn(MA)(TFA): (a) developed with a diluted solution of different organic chelating agents without PEB; (b) after PEB at 100°C and 180°C; developed using diluted propionic acid in $CHCl_3$. Dashed lines in the graphs represent the linear fitting of the curve slope.

Thus, contrast curves were obtained for Zn(MA)(TFA) photoresist by using different developers that could interact more strongly with the Zn-clusters than pure $CHCl_3$ and that could supplement the loss of the non-bonded acids during the thin film deposition or even compete with the existing carboxylate ligands. Diluted solutions (0.05%) of propionic acid, acetylacetate (acac), and acetic acid in $CHCl_3$ were tested. The resists behaved as a negative tone resist in all cases and the three contrast curves in Figure 2.7 show low D_{50}, revealing the high sensitivity of Zn(MA)(TFA) towards EUV photons. Yet, different profiles in the contrast curves were obtained for each developer. The dose to retain most of the film thickness, D_{100}, varied significantly as a function of the developer. This behaviour results in different contrast values (γ) for each developer, which is typically defined by the slope of the contrast curve, and here is approximated with a linear fitting of the slope (dashed line in Figure 2.7).

We attribute the differences among developers to distinct interactions between the chelating agents and the cluster. For instance, acetic acid and propionic acid can coordinate with the Zn cation in the cluster through a different binding mode compared to acac due to the different geometry of the binding sites. Diluted acetic acid seems to assist in the dissolution of the material better than diluted propionic acid, but it also interacted with the material on the exposed area, causing its partial dissolution. Thus, the contrast for dilute acetic acid as developer was quite low (γ_{acetic} = 0.45), whereas for propionic acid was considerably higher ($\gamma_{propionic}$ = 2.95), although more points at lower doses were needed to give a more accurate contrast value (see below). Further, acac, which is a relatively strong chelating agent, did not yield a good contrast (γ_{acac} = 0.63)

and gave signs of dissolution of the exposed part, as in the case of acetic acid. Among the tested developers, diluted propionic acid was thus considered a better developer rendering higher γ and hence was used for all the further lithography experiments.

The effect of post-exposure bake (PEB) at 100°C/ 30 s and 180°C/ 30 s was also studied. According to the TGA of the powder samples, the first temperature should not yield any loss of species from the film, whereas at the latter temperature only some desorption of non-bonded trifluoroacetic molecules was expected in the bulk material. Yet, FTIR spectra indicate that these non-bonded acids are not present in the thin film, since they are lost during deposition. However, the contrast decreased upon application of PEB at 100°C ($\gamma_{PEB|100\ °C}$ = 0.92) as compared to the non- thermally treated material ($\gamma_{propionic}$ = 2.95) and was practically lost at higher PEB temperature of 180 °C (Figure 2.7(b)). Further spectroscopic analyses to identify the structural changes induced at this temperature need to be performed in order to identify the process induced by the heating but such investigations are outside the scope of the present work.

The lithography performance of Zn(MA)(TFA) was preliminarily tested by patterning L/S features using EUV interference lithography (EUVL-IL). In Figure 2.8, selected patterns obtained for 40 nm and 30 nm half-pitch (HP) with two batches of the material synthesized by following same procedure are shown.

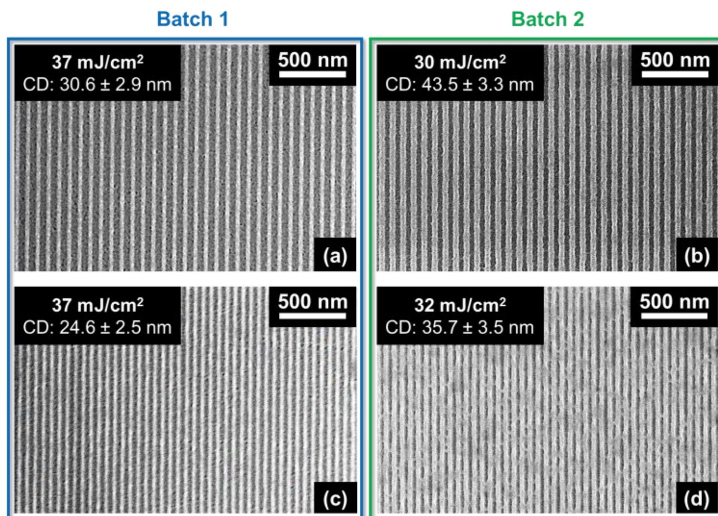

Figure 2.8. SEM images of L/S patterns of (a), (b) 40 nm, and (c), (d) 30 nm half pitch for two batches of the synthesised resist.

We observed that the material shows relatively good lithographic performance yet the relation between feature size and dose in the printed patterns differed from batch to batch (Figure 2.8). In these preliminary tests, well defined lines were observed at 37 mJ/cm^2 for Batch 1. However, their linewidths were below the intended 30 and 40 nm HP values. In contrast, Batch 2 yielded wider lines at lower doses for the same intended HP values, thus indicating over exposure.

The reproducibility of the contrast curve for these two batches was also studied. Given that the Zn(MA)(TFA) oxocluster had shown high sensitivity in our first tests (Figure 2.7(a)), new contrast curves using propionic acid as developer were recorded using smaller dose steps for the lower dose range (Figure 2.9(a)). These new experiments showed that the curves seemed to present some kind of two-step process for both batches, although the origin of this behaviour is still not understood. We estimated the contrast values for the steeper part of the two-step slope (dashed lines in Figure 2.9(a)).

As in the case of the L/S lithographic experiments, the two batches did not yield identical behaviour. Both the contrast (see Figure 2.9(a)) and the D_{50} values (dose to retain half of the thickness) were different for each batch (7.5 mJ/cm^2 for Batch 1 and 11.3 mJ/cm^2 for Batch 2). Yet, no correlation between the feature size vs. dose and contrast can be concluded at present.

Although the two batches were synthesized following the same procedure and the FTIR spectra of the bulk materials look almost identical, some small discrepancies can be spotted. A relevant one is the ratio between the peaks at 1653 cm^{-1} (C=C in MA ligand) and 1687 cm^{-1} (COO in TFA), which could indicate different ratio of the two types of ligands in the two batches. This different composition of the organic shells could be a source of variation in the printability of the two batches. In addition, we suspect that the dynamic character of the cluster-ligand bonds could introduce further changes in the material during the deposition step. This could result in slight differences in the molecular structure of the thin films, such as further variations in the MA/TFA ratio or different extents of ligand loss/hydrolysis.

We would like to point out here that all the mentioned doses are calculated using a tool factor determined by cross-calibration with other resist materials. Therefore, the dose values mentioned here are particularly specific to the calculated EUV-IL tool factor for the specific mask and pin-hole combination and might differ when using a different EUV exposure tool.[61]

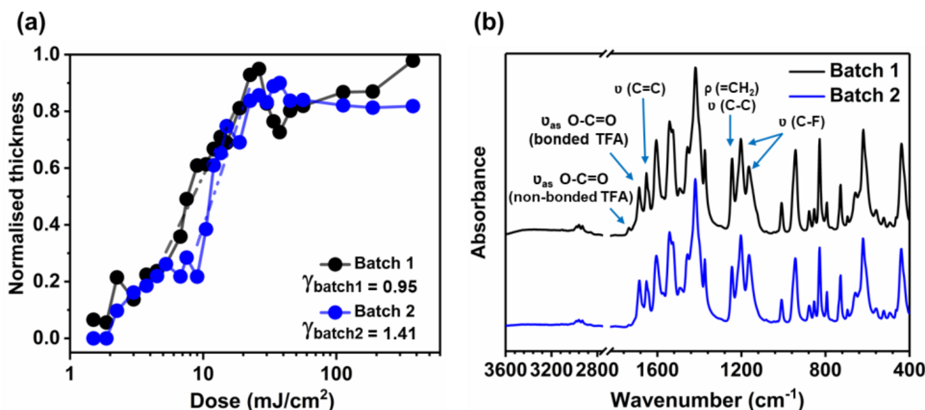

Figure 2.9. (a) Contrast curves of EUV exposed Zn(MA)(TFA) from two different batches (dashed lines in the graphs represent the linear fitting of the slope) developed using diluted propionic acid in $CHCl_3$, and (b) FTIR spectra of the two synthesised batches (bulk powder).

2.4 Conclusions

The novel Zn-based oxoclusters featuring methacrylate and trifluoroacetate ligands, Zn(MA)(TFA), possess small size, good film-forming capability and high sensitivity towards EUV photons. Yet, deposition of the material as thin films changes the solubility properties compared to the bulk material (crystalline powder), presumably due to the loss of extra non-bonded acids that are occluded in the original crystalline forms and/or rearrangements of the carboxylate ligands. Our study on the stability of these clusters using spectroscopic techniques indicates that these oxoclusters having labile ligands are susceptible to undergo structural changes in two months' scale when stored as a crystalline powder, whereas when deposited as thin film it undergoes polymerization and/or hydrolysis in a timescale of hours at room conditions.

Nevertheless, the thin films are stable in the air as well as in the vacuum long enough to perform the intact lithography application and processing (up to 4.5 h). These results provide insights into the stability of such resist systems, which is an important aspect for the development of new hybrid photoresists. The Zn(MA)(TFA) photoresist displays appreciable sensitivity towards EUV radiation albeit with potentially significant variations from batch to batch. This study highlights that inorganic resists are susceptible to undergo structural changes that should be controlled in order to attain the reproducibility of the lithographic performance. Further studies on the solubility switch mechanism

and the optimization of the lithography patterning are discussed in the next chapter.

3

ZINC-BASED OXOCLUSTER: CHEMISTRY FOR HIGH RESOLUTION NANOLITHOGRAPHY*

Abstract

Extreme Ultraviolet lithography (EUVL) is the current technology used in the semiconductor industry for the fabrication of integrated circuits (ICs), since it enables the further miniaturization of their components. For its optimal operation, photoresist materials that can efficiently use EUV photons (92 eV) to yield sub-10 nm patterns are required. However, there is a lack of understanding of the complex mechanisms induced by EUV radiation. In this chapter, we investigate the ability of a new Zn-based oxocluster to fulfil the state-of-the-art requirements for EUVL. This molecular material provides high EUV absorptivity, owing to its contents of Zn, F, and O atoms, and high resolution, given its small molecular size. High reactivity and sensitivity towards EUV is achieved through its mixed-ligand organic shell composed of methacrylate and trifluoroacetate ligands. This new resist shows outstanding lithography performance yielding down to 22 nm half pitch line/space patterns at ~20 mJ/cm^2. Spectroscopy studies on EUV exposed samples revealed an unexpected reaction pathway where fluoride ions are formed. This is an unprecedented way of efficiently inducing a solubility switch in an inorganic resist upon EUV irradiation.

*Published as: N. Thakur, R. Bliem, I. Mochi, M. Vockenhuber, Y. Ekinci and S. Castellanos, Journal of Materials Chemistry C, 2020, 8(41), 14499-14506. DOI: 10.1039/D0TC03597A. The electronic supplementary information is available at https://dare.uva.nl/en.

3.1 Introduction

The downscaling of ICs in computer chips and memory devices over the years has been possible thanks to advances in lithography techniques.[16,102,103] Among them, photolithography has been the workhorse of the semiconductor industry for ICs fabrication. In this technique, an optical projection is captured by a sacrificial photoactive layer, known as photoresist, so that the optical pattern can be transferred to the functional substrate that is the integrating part of the ICs. Within the next five years, the projected device feature size should be less than 10 nanometres.[76,104] For such miniaturization to be cost-effective, the semiconductor industry shifted from deep ultraviolet (DUV) photolithography, using light of 193 nm, to the next-generation technique, extreme ultraviolet lithography (EUVL), as its shorter wavelength (13.5 nm) offers higher resolution.[16,105]

EUV photons exceed the ionization energy of any resist material so that EUV irradiation leads to complex mechanisms that involve the generation of photoelectrons and secondary electrons, together with the associated holes (electron vacancies).[86,106,107] The understanding of this complex EUV-induced chemistry is currently rather limited.[108,109] Yet, without the proper EUV-chemistry knowledge, it is a challenge to custom-design materials for EUVL that can meet the industrial targets of sensitivity (< 20 mJ/cm^2), low line width/line edge roughness (LWR/LER < 20%), and resolution (< 20 nm).[76,78,83,109]

A prerequisite for EUV resist materials is high absorbance at 13.5 nm.[48,62] A straightforward approach to attain this is to incorporate elements into the resist layer that have high EUV absorption cross-section, typically metals. Such materials are commonly called inorganic resists and have emerged as promising candidates for EUVL applications.[26,61,62] In addition to the enhancement of EUV photon absorption, inorganic resists are also known to overcome the low tolerance of traditional organic polymers towards the etching conditions.[110] In most cases, inorganic resists comprise a core of one or more metal cations surrounded by organic ligands.[26,62,86] Exposure to the EUV photons (and the electron cascade that derive from them) induces chemical reactions on the organic ligands that result in the change of solubility properties of the resist material in the exposed areas, which ultimately leads to the pattern formation on resist layers.[55,68,111–115]

Metal-oxoclusters (MOCs) stand out among EUV inorganic resists since they are molecularly defined (small and homogeneous in size) and therefore, are anticipated to prevent variations in the nanopatterns, i.e. low LWR/LER values in the printed features.[68,70,80,116] In addition, MOCs provide great synthetic flexibility, since virtually any desired organic terminal functionality can be incorporated in their organic shell, allowing for an easy way of tuning the processability and chemical reactivity of the material.[65,66,113,114]

In the present work, we investigate the lithographic capabilities of a Zn-based MOC and study the EUV-induced chemistry that enables nanopatterning on this material. An overview of the fabrication process is shown in Figure 3.1(b). This MOC consists of a tetranuclear Zn-compound that belongs to the group of basic zinc carboxylates[117–119] and is found in the nodes of a prototypical metal-organic framework, MOF-5.[98,120,121] Previous studies have investigated dinuclear Zn-complexes as EUV resists.[68] Here, we aimed at enhancing the EUV absorbance thanks to the more condensed Zn-based oxo core and to the integration of fluorine atoms[49] as part of trifluoroacetate ligands (TFA) in the organic shell. Moreover, we incorporated methacrylate ligands (MA), which can undergo cross-linking upon EUV irradiation.[65,115]

This reaction is in fact common in MA-based clusters when irradiated with lower energy (UV) light sources,[122–125] and we anticipated that it would contribute to the solubility switch in this new Zn-based material as well. These considerations gave rise to a Zn-oxocluster shown in Figure 3.1(a) and labelled as Zn(MA)(TFA). This molecular material is a mixture of clusters with an average composition of $Zn_4O(MA)_5(TFA)$.

Zn(MA)(TFA) has previously shown a high linear absorption coefficient at 13.5 nm (12.4 μm^{-1}) and high sensitivity.[71] Here, we used EUV interference lithography (EUV-IL)[126,127] to achieve dense line/space (L/S) patterns of half-pitch (HP) down to 22 nm at low doses (~20 mJ/cm^2) on this material, a response that is close to commercial EUV resists.[61,78,83] The lithography experiments were also combined with several ex situ spectroscopic techniques, which allowed to elucidate a novel mechanism behind the nanopattern formation involving C-F bond cleavage in the TFA ligands and cross-linking of the double bond of MA ligands initiated by different radical species.

3.2 Materials and Methods

3.2.1 Zn(MA)(TFA) material and thin film deposition

The Zn(MA)(TFA) compound was synthesized by ligand exchange from a commercial Zn-oxocluster as precursor having the same tetranuclear oxo-core unit and six TFA ligands, $Zn_4O(OOCCF_3)_6$, following the protocol explained in Chapter 2. The deposition of thin films was performed from a Zn(MA)(TFA) solution of 2% (w/v) in a mixture of chloroform ($CHCl_3$), and propylene glycol methyl ether acetate (PGMEA), 9:1 v/v followed by sonication (4 min) and filtration using a 0.22 µm PTFE filter. Spin-coating of the resist solution was done at 2100 rpm spinning speed (acceleration 3000 rpm/s) for 30 s. Post application baking was applied for 30 s at 90 °C to remove the excess of the residual solvent. Same conditions were used for spin coating of Zn(TFA) (the precursor used for synthesis) using acetonitrile as the casting solvent.

Samples for UV-vis absorption spectroscopy were spin-coated on quartz substrates (500 µm thick) and for FTIR spectroscopy on double-side polished Si substrates (200 µm thick). Samples for X-ray photoelectron spectroscopy (XPS) analysis were spin coated on Cr/Au (3 nm/19 nm) sputter-coated on Si substrate. The thickness of the thin films spin coated for spectroscopic analysis was in the range of 25-30 nm and was measured by using AFM.

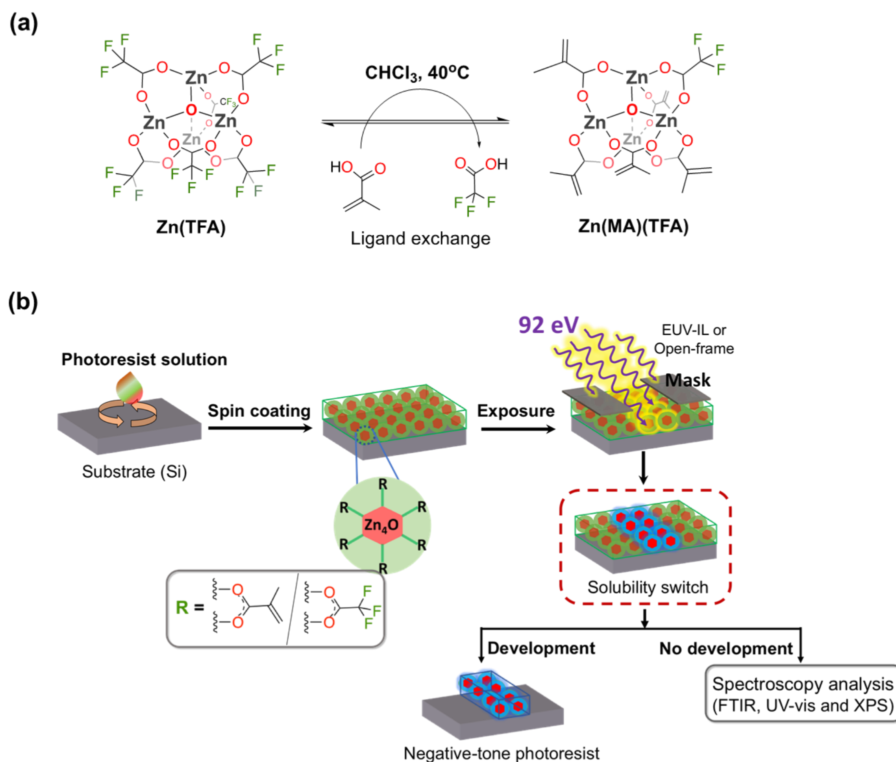

Figure 3.1: (a) Scheme of Zn(MA)(TFA) oxocluster synthesis, and (b) schematic of photolithography process and sample fabrication for different spectroscopy analysis performed on Zn(MA)(TFA) thin films.

3.2.2 EUV exposure and development

All EUV exposures were carried out at a wavelength of 13.5 nm (92 eV), at the XIL-II beamline of the Swiss Light Source (SLS) synchrotron. For spectroscopic studies open frame, 1.7 × 1.7 mm^2 area mask and pin-hole (PI), 70 µm was used. For L/S features, the EUVL-IL[126] tool was equipped with a transmission mask that resolved half-pitch (HP) of 22, 30, 40, and 50 nm combined with a PI 70 µm.

Diluted propionic acid (0.05%) in $CHCl_3$ was used as a developer (8-10 s). Zn(MA)(TFA) behaved as a negative tone photoresist and therefore the exposed areas turn less soluble in the chosen developer.

All the mentioned doses in this work are specific to this EUV-IL setup. The tool factors for the specific mask and PI combinations are calculated by cross-calibration with a bench-mark resist material. Thus, this might not correspond to an absolute number and doses might differ slightly when using a different EUV exposure tool.[61]

3.2.3 Post-exposure analysis

UV-vis absorption spectroscopy was performed in a Shimadzu UV2600 spectrophotometer. FTIR spectroscopy of the thin films was performed in transmission mode under vacuum in a Bruker Vertex 80v spectrometer. To remove the interference fringes in the FTIR of thin films Fast-fourier transform (FFT) with low-pass filtering was applied. XPS was performed using a monochromatic Al K_α source (1486.6 eV) in ultra-high vacuum ($p \leq 5\times10^{-9}$ mbar) setup equipped with Scienta R4000 HiPP-3 analyser. Fitting of the peaks was done using UNIFIT 2018 Scientific software. SEM imaging on L/S features was performed with a top-down view using a FEI Verios 460 operating at a current of 100 pA, dwell time of 10 µs and altering voltage of 5 kV and 2 kV. LWR evaluation was carried out using SMILE, a SEM image analysis software developed at the Paul Scherrer Institute. Unbiased LWRs values[128] were obtained using the average power spectral density (PSD) of the lines in their respective SEM images, the unbaising was performed using a standard PSD model.[129] AFM measurements were done using a Bruker Dimensions Icon in ScanAsyst-air mode.

As a control experiment, for UV-vis and FTIR analysis spectra of a freshly spin-coated thin film was used (fresh reference) to inspect the effect of aging/partial degradation of the sample occurring between the exposure and the spectroscopy experiments (shown in SI).

3.3 Results and Discussions

3.3.1 EUV lithography performance

To evaluate Zn(MA)(TFA) oxocluster as a photoresist (thickness ~37 nm) for EUV lithography application, dense L/S patterns of HP 50 nm, 40 nm, 30 nm and 22 nm were printed using the EUV-IL tool at the Paul Scherrer Institute.[130] The L/S patterns printed on the thin film after exposure and subsequent development were inspected using both AFM and SEM. Selected SEM images (in Figure 3.2) show the transfer of L/S patterns with a notably low dose. No scumming (scattered rests of material) between lines was observed in the SEM images. To

highlight the importance of the ligand exchange here, Zn(TFA), the precursor with the same tetranuclear Zn oxo-core used for the synthesis of Zn(MA)(TFA), was also exposed to EUV radiation. The spin coated thin films of Zn(TFA) had high surface roughness and a clear aggregation of the oxoclusters can be seen in the AFM optical images in the exposed area due to the chemical changes upon EUV exposure (shown in Appendix II).

An important aspect in resists' performance is the dose-to-size, which is the incident exposure dose that is needed to attain features of the intended critical dimension. The plot of printed linewidth as a function of EUV dose for Zn(MA)(TFA) (Figure 3.3)[10] showed that the dose-to-size (open markers) in all cases is close to 20 mJ/cm^2, which is the current requirement for EUV resists. Selected SEM images (operated at 2 kV) used to calculate the dose-to-size for HP 30 nm and 22 nm as a function of EUV dose are shown in Figure S3.2. Furthermore, the aspect ratio of the printed L/S patterns were estimated using the height measured from the corresponding AFM contour profiles (shown in SI, Figure S3.1) and aspect ratios of ~1:3 for HP 50 nm, 30 nm, 22 nm and ~1:2 for HP 44 nm were obtained.

Additionally, the unbiased LWRs of dense L/S features were also calculated for the doses of HPs nearest to the printed dose-to-size values (Figure 3.3). The LWR values and their corresponding SEM images are represented in the Figure 3.4. As a result of line wiggles seen in SEM image of HP 22 nm the results of unbiased LWR values are relatively higher as compared to other printed HPs. However, the LWR values of the other HPs fulfil the industry requirement (LWR < 20% of CD).[83] Table 3.1 summarizes the performance of some hybrid inorganic-organic based materials as EUV photoresists using EUVL-IL tool at PSI.

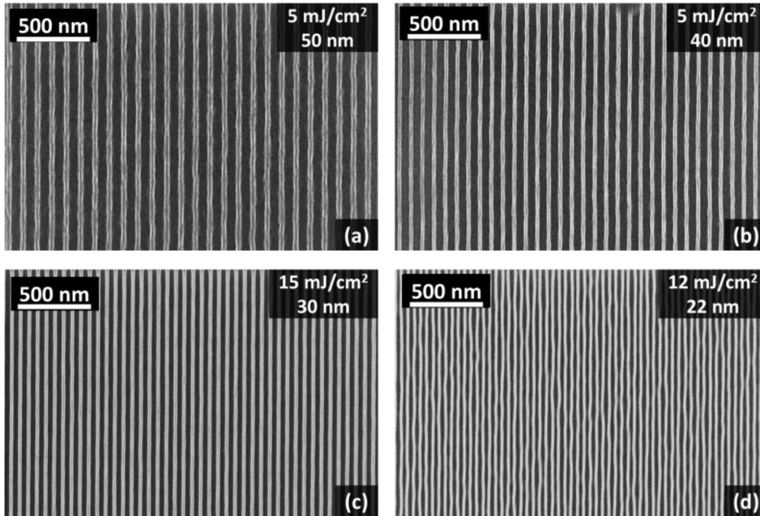

Figure 3.2: Selected SEM (operated at 5 kV) images of patterned line/space features of half pitch 50 nm, 40 nm, 30 nm, and 22 nm using EUV-IL tool.

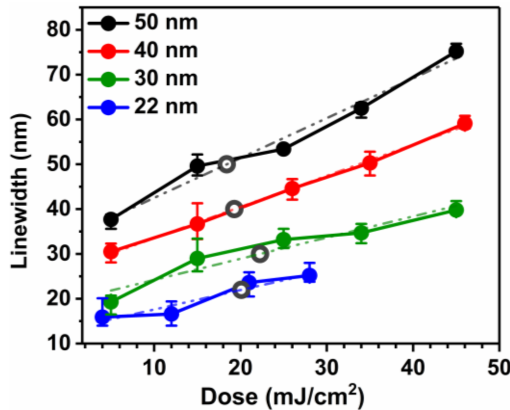

Figure 3.3: Dose dependency of linewidth of line/space printed patterns of four half-pitch: 50 nm, 40 nm, 30 nm and 22 nm measured with SEM (operated at 2 kV), where grey open markers represents the dose-to-size.

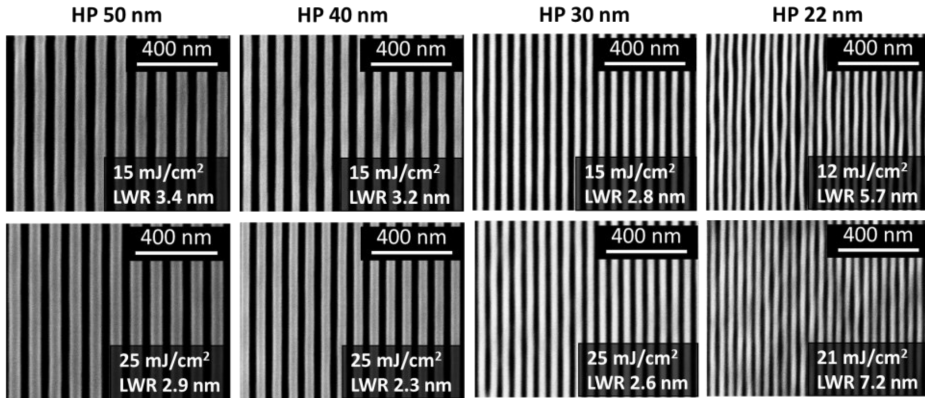

Figure 3.4: LWR (unbiased) results obtained from PSD of respective SEM (2 kV) images of line/space features.

Table 3.1: Performance of some inorganic/ hybrid inorganic-organic EUV photoresists tested with the EUV-IL tool at PSI grouped by their content of metallic element.

Resist	CD [HP] (nm)	Dose (mJ/cm²)	LWR/LER (nm)
Inpria YA-BA[131]	14.9 [16]	48	1.8
	10 [11]	---	1.7
$[(PhSn)_{12}O_{14}(OH)_6]Cl_2$[132]	[18]	350	---
$[(BuSn)_{12}O_{14}(OH)_6](OH)_2$[133]	[50]	131	---
$[(BuSn)_{12}O_{14}(OH)_6(AcO)_2$[133]	[40]	74	---
HSQ[134]	[22]	40-90	~2-3
$Zr_6O_4(OH)_4Mc_{12}$[65]	[50]	57	---
$Zn_2(CO_2R)_4$ Zn-mTa[68]	[16]	45	---
	[13]	35	---
Zn(MA)(TFA)	30	22	2.8-2.6
	22	20	5.7-7.2

3.3.2 Mechanistic Insights

The promising and outstanding performance of this new material prompted us to investigate the underlying mechanism in the pattern formation. In particular, we wanted to gain insight in the role of each type of ligand in the solubility switch that it undergoes after EUV irradiation. For that purpose, the chemical changes after EUV exposure were investigated using ex situ spectroscopic techniques. FTIR and UV-vis absorption spectroscopy were employed to identify modifications in the organic ligands, whereas XPS allowed to detect changes in both inorganic and organic components, as it gives information on elemental ratio and on the chemical environment of all elements.

Thin films were exposed to four doses of EUV light from a dose above the threshold necessary to render a fully insoluble thin film (> 20 mJ/cm^2)[71] up to a high dose where a full conversion of the pristine materials is expected. Thus allowing the identification of the spectral features from the EUV irradiation product in Zn(MA)(TFA) resist.

A thin film of Zn(MA)(TFA) on Si was exposed to increasing EUV doses on different areas on the thin film (Figure 3.5(b)) of the same sample and the FTIR of each area was collected (Figure 3.5(a)). The peaks were assigned according to the literature of Zn-based tetranuclear clusters.[71,98,100] A decrease in the area of the peaks (Figure 3.5(c)) assigned to the carboxylate groups of both ligands, TFA (ν_{as} 1676 cm^{-1}) and MA (ν_{as} 1544 cm^{-1}), was detected with the increasing dose. The same trend was observed for the peaks assigned to C-F stretching (1205 and 1155 cm^{-1}). However, a relative increase of the peaks in the aliphatic C-H stretching region (2929 - 2885 cm^{-1}) was observed. This indicates that EUV photons promote the decarboxylation of both TFA and MA. In addition, the simultaneous decrease of the ν_{as}(COO) and ν(C-F) peaks suggests that TFA ligands are partially lost, either as complete units or as a result of the ligand fragmentation arising from a decarboxylation process. However, in the case of the MA ligands, the preservation and increase of aliphatic C-H stretching peaks is in line with cross-linking reactions between terminal double bonds.

To further investigate the changes in MA ligands upon EUV exposure we monitored the changes in the UV-vis absorption spectrum of the material after irradiation with different doses of EUV light. The unexposed material displays an absorption band at 198 nm, which arises from electronic $\pi \rightarrow \pi^*$ transition localized in the MA ligands of Zn(MA)(TFA) (Figure 3.6(a)). The bleaching of this band as the EUV dose increases clearly indicates the loss of double bonds with EUV exposure (Figure 3.6(b)). Taking into account that the FTIR experiments confirmed the presence and slight increase of C-H bonds in aliphatic carbons, this result is in line with the promotion of cross-linking reactions between terminal double bonds of the MA ligands, which yields saturated carbon chains in the thin film.[65,115]

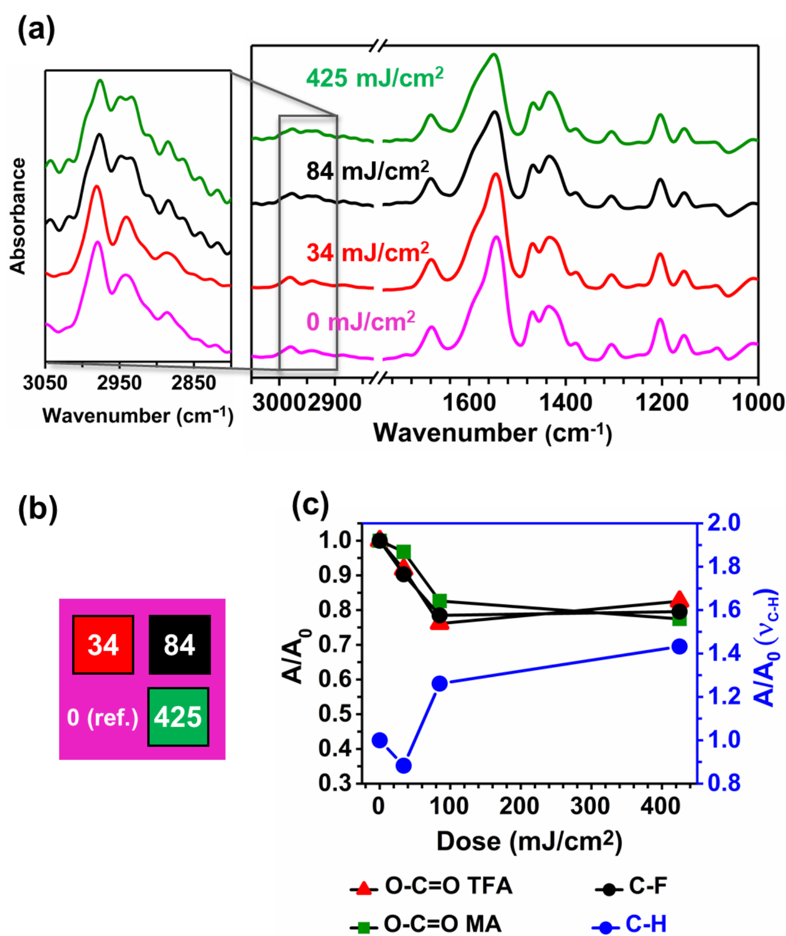

Figure 3.5: (a) FTIR spectra of a Zn(MA)(TFA) resist film before and after EUV exposure, (b) scheme of an exposed sample where delimited areas were exposed to different EUV doses (in mJ/cm^2), and (c) changes in the area of the peaks related to MA and TFA ligands as a function of EUV dose relative to the unexposed region.

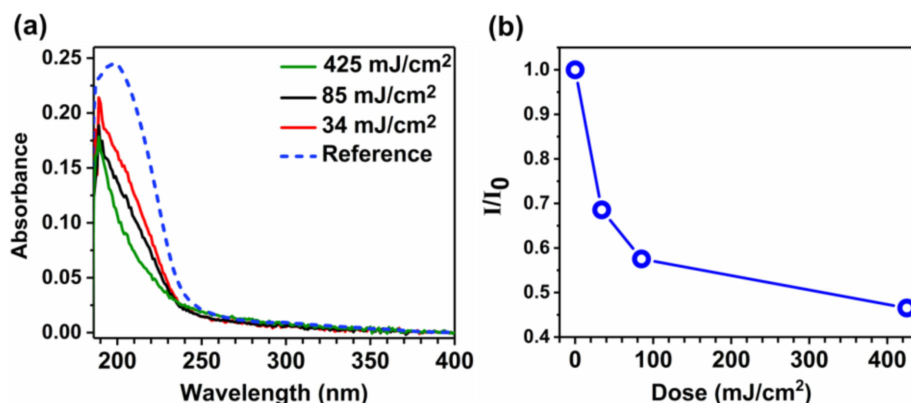

Figure 3.6: (a) UV-vis absorption spectra of the resist film, and (b) changes in the UV-vis absorbance maxima relative to the reference as a function of the EUV dose.

As vibrational modes and electronic transitions arising from the inorganic core fall out of the spectroscopic windows in both FTIR and UV-vis experiments, XPS was used to investigate other processes that might occur in the Zn(MA)(TFA) molecule after EUV irradiation. We focused on the detection and tracking of different C, O, F, and Zn-species as the function of the EUV dose. To do so, we fitted the C 1*s*, O 1*s*, F 1*s*, and Zn 2$p_{3/2}$ high resolution spectra for the unexposed material and tracked the species of interest as a function of dose (Figure 3.7(a) and Figure S3.5).

Although the C 1*s* spectra could be fitted with 4 components, here we will only consider the components with higher oxidation states, assigned to O-C=O (289.1 eV) and C-F (292.8 eV). O 1*s* spectra were fitted using 2 components, assigned to O atoms participating in Zn-O bonds (oxo and hydroxo groups, 532.1 eV) and O atoms in O-C=O groups (530.4 eV). A peak assigned to F atoms in the TFA ligands was found in the F 1*s* accompanied by a small peak with smaller chemical shift (see explanation later in the same section). The Zn 2$p_{3/2}$ peak was fitted using only one component indicating no major chemical differences between the Zn atoms in the inorganic core.

The evolution of the C 1*s* and O 1*s* high resolution spectra signified the loss of O-C=O species upon EUV exposure (Figure S3.5), in line with the FTIR results. Yet the most prominent changes were observed in the high-resolution spectra of the F 1*s* (Figure 3.7(a)). In the latter, it was noticed that the peak at 684.5 eV increases as a function of EUV dose. This peak is assigned to fluoride ions, likely bonded to Zn metal (Zn-F) in the thin film after EUV exposure.[135–137] The formation of such metal-fluoride bond has been observed in metal complexes after exposure to focused electron beam and was explained by C-F bond cleavage and appearance of F^- species.[138] The presence of this peak in low intensity in the

unexposed sample is attributed to the chemical changes induced by X-ray photons used for the XPS measurement, as a rise of this peak was observed as a result of prolonged irradiation with X-ray after consecutive measurements on the same spot (Figure S3.7).

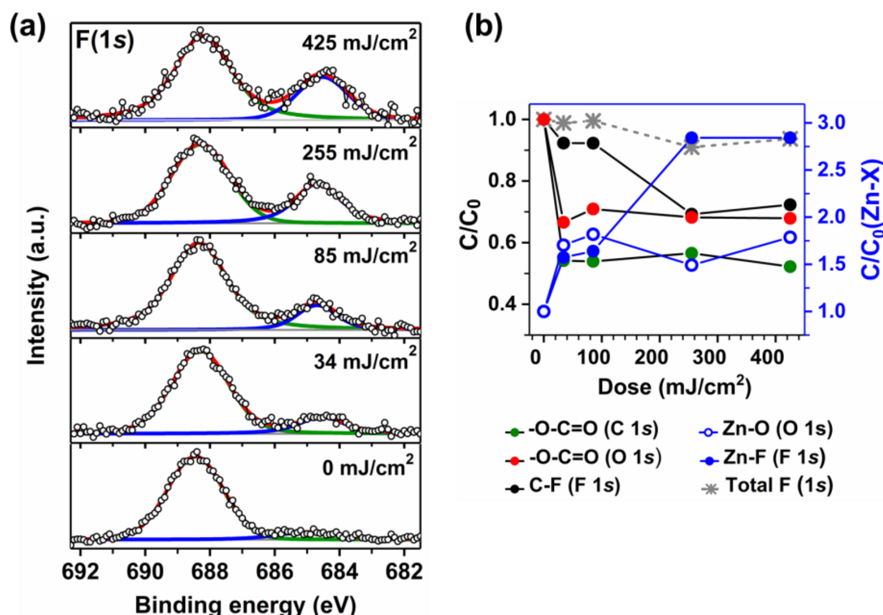

Figure 3.7: (a) Experimental data (dots) and fitting (solid line) of the F 1*s* high-resolution spectra for the unexposed and EUV exposed Zn(MA)(TFA) resist, (b) changes in the elemental ratio of the components of O-C=O (C 1*s*), O-C=O (O 1*s*) and Zn-O (O 1*s*), C-F (F 1*s*), Zn-F (F 1*s*) and in the total F ratio (F 1*s*) relative to Zn as a function of EUV dose.

Since our X-ray photoelectron spectrometer does not have spatial resolution, for this experiment each dose required the preparation and exposure of a different sample. Therefore, to track the effect of EUV, we calculated the ratio of each species relative to Zn for each sample and the ratio found at each dose was compared to the initial ratio of each species in the unexposed sample. The ratios relative to Zn 2$p_{3/2}$ of selected components in C 1*s* (O-C=O), O 1*s* (O-C=O and Zn-O) and F 1*s* (C-F and Zn-F) spectra were plotted as a function of dose (Figure 3.7(b)). Loss of carboxylate (O-C=O, C 1*s* and O 1*s*) was detected, yet the contribution of TFA and MA to it cannot be distinguished with this technique, as both carboxylate peaks have the same chemical shift. An increase in Zn-O component as a function of dose was also observed, which can be attributed to the formation of ZnO_x species after the EUV exposure. That is, after

decarboxylation/ligand loss during exposure, the Zn atoms left in the film can react with water and oxygen in the atmosphere after the samples are taken out of the exposure chamber in the air. As the Zn-F species increase with EUV dose, a decrease in the C-F components is observed, simultaneously. The total concentration of fluorine (grey asterisks in Figure 3.7(b)), decreased by 10% at high EUV doses. Overall, the changes detected in XPS in the fractional ratio with EUV exposure are fairly comparable to the results obtained from FTIR regarding decarboxylation and C-F bond loss.

From the combination of all spectroscopic results, we propose the reactions in Figure 3.8 as important contributions to the solubility switch in the Zn(MA)(TFA) resist upon EUV exposure**.** Ionization of the oxoclusters after absorption of EUV radiation results in the emission of a photoelectron and formation of a radical cation that can further yield the decarboxylation of ligands (MA or TFA)(Figure 3.8(a)). This process can also be initiated by an electron with kinetic energy higher than the ionization potential of the molecule.[66,139,140] The resulting fragments would be an allyl or a trifluoromethyl radical and an outgassing neutral CO_2 molecule. These sites are likely to react with water or oxygen when the film is exposed to ambient atmosphere after EUV exposure and can further lead to aggregation with neighbouring clusters.[141–143] Meanwhile, the radicals formed in path (a) can initiate cross-linking reactions of the terminal double bonds in the MA ligands (process (c) in Figure 3.8).

In addition to dissociative ionization processes, secondary electrons with lower energy than the ionization potential can interact with Zn(MA)(TFA) oxocluster and induce the C-F cleavage. This process, known as dissociative electron attachment (DEA), has been reported for halogen-containing molecules and in particular for trifluoroacetic acid.[144–148] The resultant fragments would be F^- and a difluoroacetyl radical (process (b) in Figure 3.8). Although a detailed structure of the final product cannot be inferred, XPS studies have clearly shown the presence of new F^- species in the thin film after EUV exposure. We assume that they are stabilized by the Zn^{2+} metal cations, as explained above. In turn, the difluoroacetyl radical is expected to react with the neighbouring ligands, such as methacrylate ones. Reoxidation of Zn-sites after ligand loss could occur after the exposed sample is exposed to air, as indicated by the XPS studies.

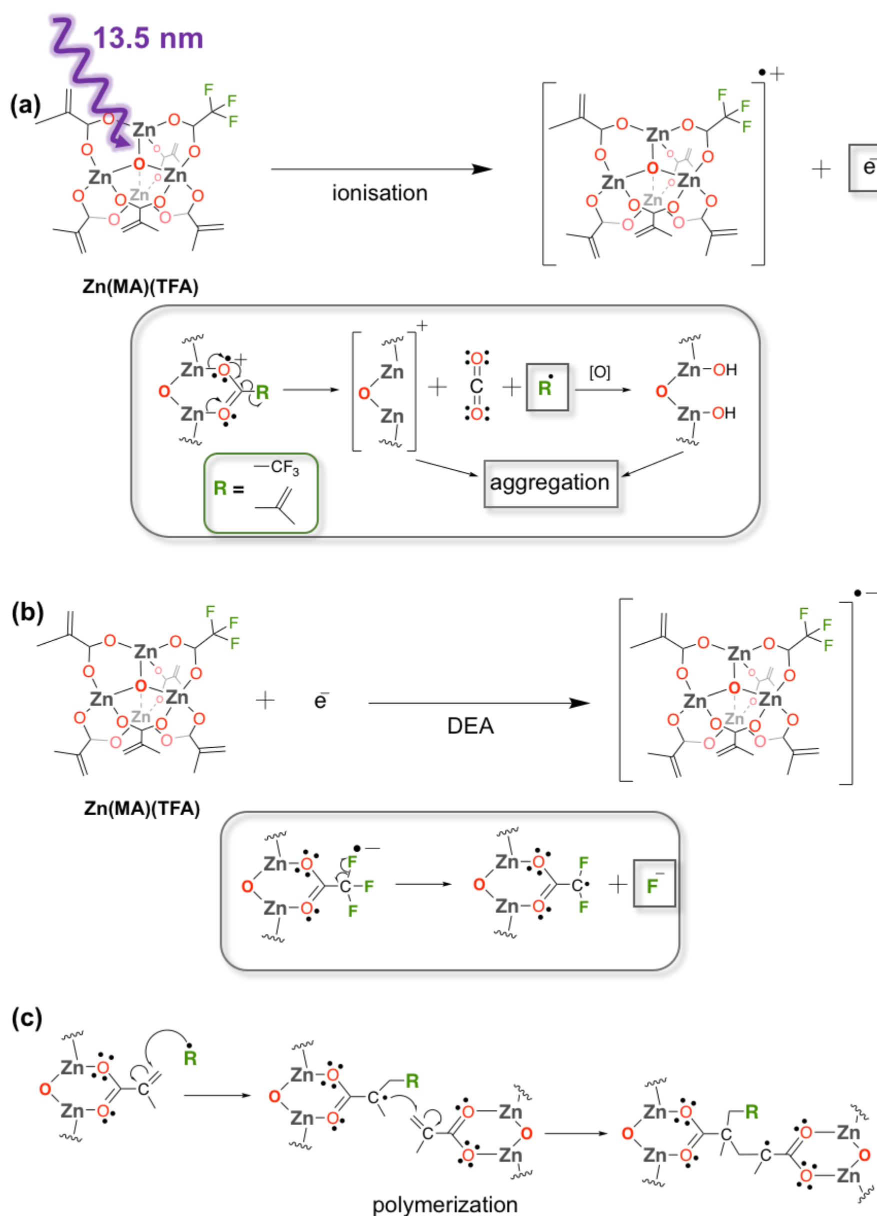

Figure 3.8: Proposed reaction paths from the spectroscopy results that contribute towards the solubility switch in Zn(MA)(TFA) upon irradiation to EUV photons: (a) ionisation of the oxocluster upon absorption of EUV and subsequent decarboxylation, (b) DEA: cleavage of the C-F bond in the oxocluster, and (c) radical initiated polymerization of the oxocluster.

3.4 Conclusions

The Zn(MA)(TFA) oxocluster has shown the potential to be a competitive material for EUVL applications. EUV interference lithography tests on the Zn(MA)(TFA) resist showed that targeted half-pitch of line/space features for 50 nm, 40 nm, 30 nm and 22 nm can be patterned with a dose of ~20 mJ/cm^2 with unbiased LWR values that comply with the industry requirements. From spectroscopic studies combining FTIR, UV-vis absorption and XPS, we propose a plausible mechanism behind the high sensitivity of this resist that consists of three major reaction paths:

(a) Ionization and decarboxylation of either the methacrylate or trifluoroacetate ligand to give rise to radical species. The decarboxylated site can evolve into hydroxo and oxo species that could bridge neighbouring clusters.

(b) XPS studies suggest the migration of fluorine atoms from the organic shell to the metal core, most likely promoted by the dissociative electron attachment reaction pathway.

(c) Oligomerization of the terminal double bonds in neighbouring methacrylate ligands.

These novel insights into the reaction mechanisms and their correlation to the lithography performance of Zn(MA)(TFA) will help the EUV lithography community to have a better understanding of the molecular design required for new efficient EUV resist materials.

4

PHOTON-INDUCED FRAGMENTATIONS OF ZINC OXOCLUSTER*

Abstract

The mechanisms responsible for the solubility switch in hybrid inorganic-organic based photoresists materials are not well understood. In this regard, UV/ VUV (4 to 14 eV) photon-induced fragmentations of Zn-based oxoclusters, $Zn_4O(MA)_{6-x}(TFA)_x$ (MA: methacrylate ligand and TFA: trifluoroacetate ligand) in the gas phase are investigated to study the fundamental reactivity of their cationic form. Irradiation of the parent cations results mainly in the ligand dissociation and fragmentation of the inorganic clusters at energies below the second ionization threshold (~12 eV). Above ~12 eV, second photo-ionization processes compete with the photo-fragmentation pathway. This ionization energy is correlated to the methacrylate ligand in the organic shell of the Zinc oxocluster. We presume that this type of fragmentations can also occur when the oxoclusters are ionized in the thin film upon EUV irradiation and this study therefore gives the fundamental insights into the reactive sites and stability of the cationic species of $Zn_4O(MA)_{6-x}(TFA)_x$ after exposure to ionizing radiation.

*Published as: N. Thakur, A. Giuliani, L. Nahon, and S. Castellanos, Journal of Photopolymer Science and Technology, 2020, 33(2), 153-158. DOI: 10.2494/photopolymer.33.153.

4.1 Introduction

As the lithography technology shifted from 193 nm (deep ultraviolet, DUV) towards a shorter wavelength of 13.5 nm (extreme ultraviolet, EUV), metal-based resist systems emerged as a promising alternative to the traditional organic chemically amplified resists (CARs).[62,65,76,81] This unprecedented growing interest in metal-based resists systems is due to one key contribution of the metals in the lithographic process: the enhancement of the projected image absorption by the resist.[45,48,61,92] This is because the absorption cross-section of EUV photons is generally higher for metals as compared to C, H, O, N, which are constituting elements of organic CARs.

Metal-oxo clusters (MOCs), a class of hybrid inorganic-organic molecular material, have emerged as promising photoresists for EUV lithography (EUVL) applications. MOCs have a molecularly defined small structure and offer synthetic versatility, as they can undergo ligand-exchange reactions.[63,64,149] In our previous studies, Zn-MOCs, $Zn_4O(MA)_{6-x}(TFA)_x$ having a mixed organic shell containing both methacrylate (MA) and trifluoroacetate (TFA) ligands have shown high sensitivity/ reactivity towards EUV photons and good EUVL performance. The experimental absorption coefficient of Zn-MOCs is relatively high (12.4 μm^{-1}) as compared to the traditional photoresist (5 μm^{-1}).[71,150] However, the mechanism behind the solubility switch upon EUV exposure to such high energy EUV radiation is not yet well established for the resist materials, in general.[71,151,152] Thus, the reaction paths triggered by EUV irradiation on hybrid inorganic-organic based resists that enable patterning in lithography is currently a very active research area. EUV photons at 13.5 nm (92 eV) exceed the ionization potential of the photoresist material (usually in the range of 6 to 14 eV) such that exposure to EUV photons results in the ionization of the material. The ionization can be accompanied by the emission of a photoelectron with an energy up to ~80 eV (from the valence band) that is capable to trigger an electron cascade, i.e. the formation of several secondary electrons and holes.[86,153–156]

The study at a molecular level of the complex reaction mechanisms and of the resultant chemical changes occurring in resists' thin films (tenths of nanometers thickness) upon EUV exposure is challenging.[157] Alternatively, to overcome this challenge the reactivity of metal-oxoclusters can be studied in the gas phase. This method has been utilized previously to study the decay reaction paths that an excited MOC can undergo and how these paths can differ when different organic ligands are used.[66,157]

In this work, we studied photon-induced fragmentation of Zinc-based MOCs, $Zn_4O(MA)_{6-x}(TFA)_x$. Zn-MOCs were brought into the gas phase in their cationic form (with a net charge of +1), trapped and exposed to ultraviolet (UV) and vacuum ultraviolet (VUV) photons (4 to 14 eV range). The resultant photon-induced fragments and ionization products were identified with a mass

spectrometer coupled to the ion trap. These experiments reveal the reactions that ionized Zn-based oxocluster molecules can undergo and give us insights into the possible species that can derive from the holes formed in the thin film upon exposure to the ionizing radiations.

4.2 Materials and Methods

4.2.1 Synthesis of photoresist: Zn(MA)(TFA)

The Zn(MA)(TFA) compound was synthesized by the ligand exchange method from a commercially available Zn-oxocluster as a precursor having the same tetranuclear oxo-core unit and six TFA ligands in the organic shell of the oxocluster, $Zn_4O(OOCCF_3)_6$, following the same protocol as described in our previous studies.[71]

4.2.2 Sample preparation and Experimental details

To perform the photo-induced fragmentation experiments, a solution of $Zn_4O(MA)_{6-x}(TFA)_x$ was prepared (1.5 mg in 1 mL of an acetonitrile/acetone mixture in 3:2 ratio, 4 min sonication) and filtered using 0.22 μm PTFE filter.

A commercial linear quadrupolar ion trap (Thermo Scientific LTQ XL) mass spectrometer using an atmospheric pressure photoionization (APPI) source coupled to the DESIRS beamline at SOLEIL synchrotron radiation facility (France) was used for the experiments.[158,159] A syringe pump with a flow rate of 10 μl min^{-1} was used for all the experiments. The molecules were ionized by the Krypton discharge lamp of the APPI source. The parent cations were selectively trapped in the linear quadrupole ion trap and exposed to monochromatic and high-harmonics free photons (by using Kr-filled gas filter and a quartz window when required). Figure 4.1 shows the simplified schematic of the experimental setup.

All the spectra were normalized to the photon flux variations over the energy range of 4 to 14 eV (measured by using a Si photodiode) to obtain relative cross section or photon-normalized ion yield. DFT calculations were performed with Gaussian 16[160] using the functional UB3LYP and the Def2TZVP basis set.

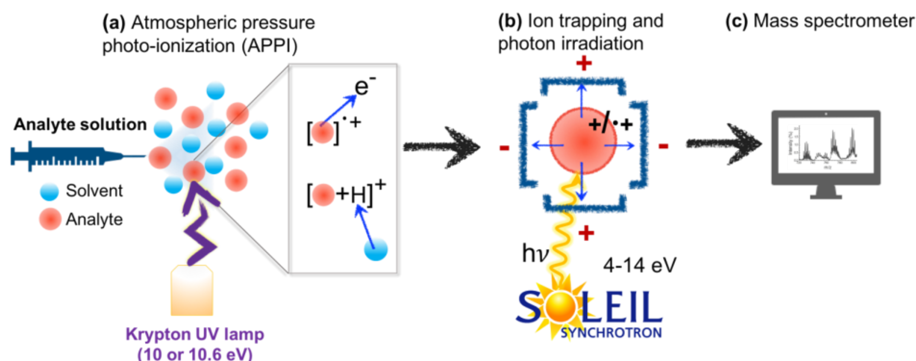

Figure 4.1: Schematic representing the experimental setup: (a) Ionization of molecules using atmospheric pressure photo-ionization (APPI) method, (b) linear quadrupolar ion trap and photon ionization by SOLEIL synchrotron radiation, and (c) recording mass spectra.

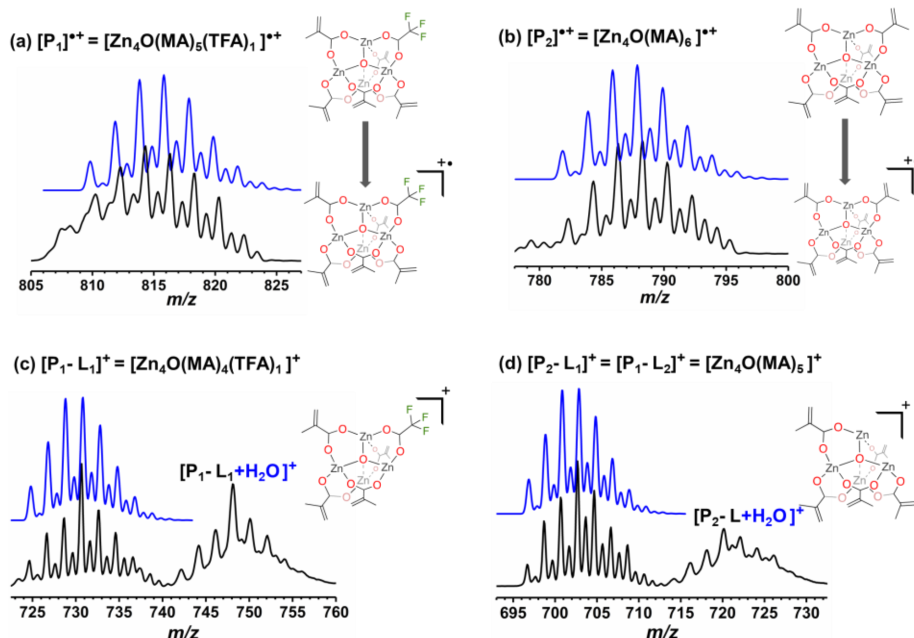

Figure 4.2: Mass spectra of the four trapped parent ions before the photon irradiation. Simulated isotopic distribution using ChemCal[161] is shown in blue.

4.3 Results and Discussions

$Zn_4O(MA)_{6-x}(TFA)_x$ (x= 0 or 1) MOCs studied in this work have 4 Zn atoms in a tetrahedral geometry bridged by an O in the centre (μ_4-oxo) in their inorganic core. They were synthesized by a ligand exchange method as previously reported[71] using $Zn_4O(TFA)_6$ as a precursor, which has the same oxo-core and 6 TFA ligands in the organic shell. TFA ligands were exchanged by MA ligands (a ligand of interest for nanolithography applications).[63,65,69,71] The ligand exchange reaction proceeds in an equilibrium and therefore, the composition of the resulting Zn-MOCs reflects a statistical distribution with the combination of both MA and TFA ligands in the organic shell, where MA is the more abundant ligand. Through our previous analytical spectroscopy studies, we deduced that the synthesized Zn-MOCs will have an average of MA/TFA ratio of approximately 5:1, i.e. the average formula of the synthesized oxocluster is close to $Zn_4O(MA)_5(TFA)$.[71]

To generate the parent ion species from the neutral Zn-oxoclusters, the APPI method was used. Figure 4.2 displays the mass spectra of the four trapped parent ions before irradiation. As expected from the statistical distribution of the ligand composition, two of the trapped parent ions were identified as: 1) the product of ionization of the Zn-MOC with a 5:1 MA/TFA (organic shell) ratio at *m/z* 816.05, labeled as $[P_1]^{\bullet+}= [Zn_4O(MA)_5(TFA)]^{\bullet+}$, and 2) its analogue with all 6 MA ligands at *m/z* 788.12, $[P_2]^{\bullet+}= [Zn_4O(MA)_6]^{\bullet+}$. The ability to isolate the parent ion with 5:1 MA/TFA ligands and with all 6 MA ligands allows us to study the influence of the TFA ligand on the reactivity of the radical cation of the Zn-MOCs.

In addition, the ions that result from one ligand loss from the starting neutral molecules, with $[P_1\text{-}L_1]^+ = [Zn_4O(MA)_4(TFA)]^+$; *m/z* 730.97, and $[P_1\text{-}L_2]^+ = [P_2\text{-}L_1]^+ = [Zn_4O(MA)_5]^+$; *m/z* 703.04, where L_1 = MA and L_2 = TFA, could also be trapped. However, in the latter cases the trapping always led to the co-existence of the hydrated species $[P_1\text{-}L_1\text{+}H_2O]^+$ and $[P_2\text{-}L_1\text{+}H_2O]^+ = [P_1\text{-}L_2\text{+}H_2O]^+$, which might result from the hygroscopic nature of the Zn-based inorganic core.

The simulated isotopic distribution (mass spectra shown in blue using online tool Chemcal[161]) in Figure 4.2 remains the same for all the four trapped oxoclusters (at the corresponding *m/z* values), regardless of the presence of 5 or 6 ligands in their organic shell. This is because this pattern results from the 4 Zn atoms and is the fingerprint of the tetranuclear inorganic core of the oxoclusters. A broadening of the peaks was observed for $[P_{1/2}\text{-}L_{1/2}\text{+}H_2O]^+$ adducts. The origin of this feature is unclear and needs further investigations that are out of the scope of the work in this chapter.

As an example of the photo-fragmentation products formed from the different parent ions, the mass spectra acquired after irradiation of $[P_1]^{\bullet+}$ and $[P_1\text{-}L_1]^+$ at a high photon energy of 13.5 eV is shown in Figure 4.3. The counterparts derived from $[P_2]^{\bullet+}$ and $[P_2\text{-}L_1]^+$ ($=[P_1\text{-}L_2]^+$) yielded analogous results and are not shown.

At this energy, the second ionization products of all parent ions were detected. For the parent ions identified as $[P_{1/2}]^{\bullet+}$, with 6 ligands, the double charged ions, labeled as $[P_{1/2}]^{2+}$, were accompanied by the adducts resulting from the coordination of one or two water molecules, $[P_{1/2}+xH_2O]^{2+}$, x=1-2, whereas in the case of the doubled charged species with 5 ligands, only the hydrated adducts, $[P_1\text{-}L_{1/2}+xH_2O]^{2\bullet+}$, x=1-3, were observed (insets in Figure 4.3).

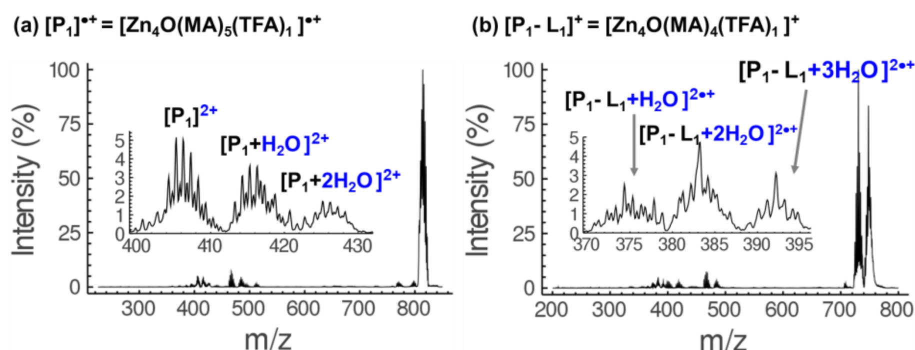

Figure 4.3: Mass spectra after irradiation with 13.5 eV photons. Zoomed in regions represent the second ionization products accompanied by their water adducts.

Noticeably, a fragmentation product was detected at *m/z* 467.46 and identified as $[Zn_3O(MA)_3]^+$ in the spectra of all the four irradiated parent ions (Figure 4.4(a)). The isotopic mass distribution detected experimentally clearly matched the simulated mass distribution for 3 Zn atoms in the oxo-core (Figure 4.4(b)). The formation of this species reveals that the inorganic cluster can dissociate such that one Zn atom can detach from the molecule.

In the particular case of the parent ions $[P_{1/2}]^{\bullet+}$, the product of ligand dissociation $[P_{1/2}\text{-}L_1]^+$ and its adduct with acetonitrile, $[P_{1/2}\text{-}L_1+CH_3CN]^+$ was mostly observed at a lower energy range (Figure 4.5 shows an example at 9 eV). Furthermore, in this m/z range, species that match the molecular weight of $[P_{1/2}\text{-}OH]^+$ was also detected. We hypothesize that protonation of the μ_4-oxo group might open up this reaction path. Interestingly, the detected di-cation preserved the molecular structure with all ligands and seemed to have high affinity towards water molecules (Figure 4.3) as compared to its parent ions.

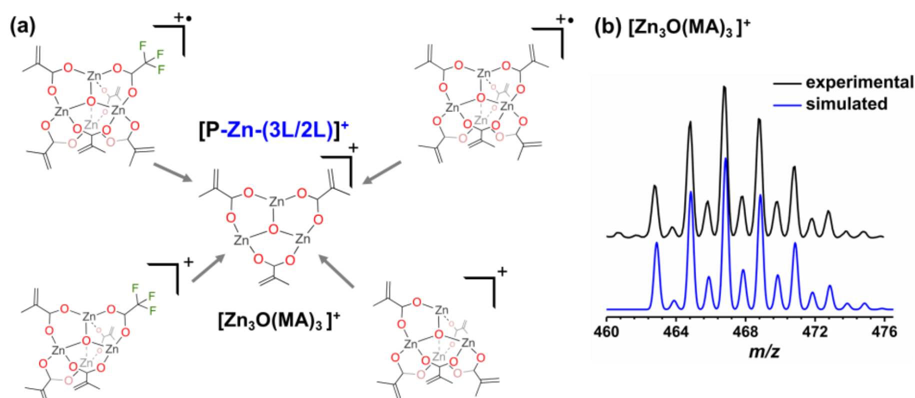

Figure 4.4: (a) Formation of $[Zn_3O(MA)_3]^+$ as a photo-fragmentation product from all four trapped parent species, and (b) observed (black) and simulated (blue) mass distribution of $[Zn_3O(MA)_3]^+$ product.

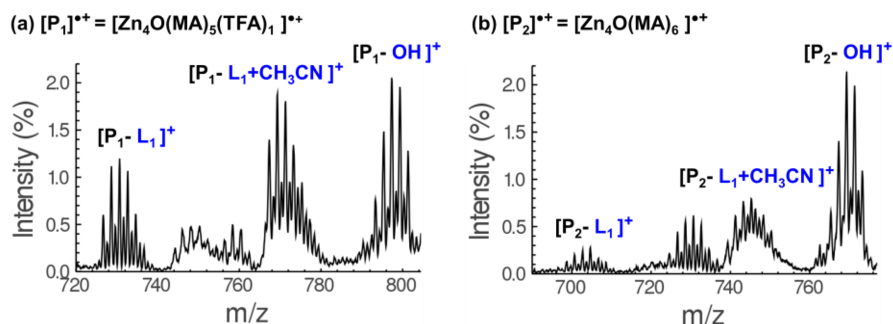

Figure 4.5: Ligand dissociation products, $[P_{1/2}\text{-}L_1]^+$ and product assigned to OH loss observed after irradiation with 9 eV photons of the parents ions $[P_{1/2}]^{\bullet+}$.

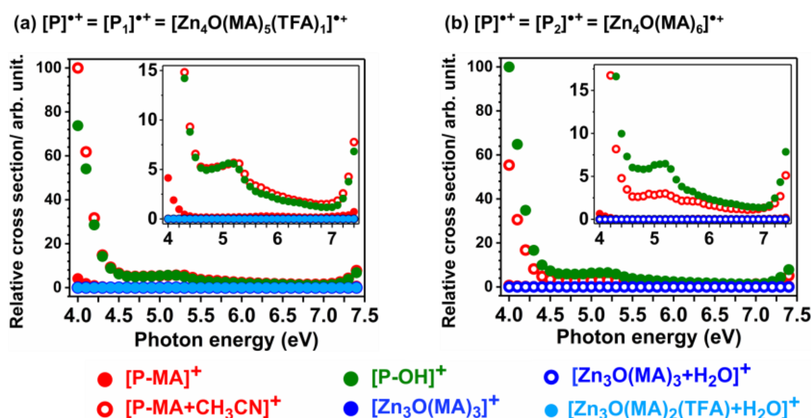

Figure 4.6: Photon normalized yield of the products formed in the 4 to 7.4 eV photon range from $[P_{1/2}]^{\bullet+}$.

The relative yield of the photo-fragmented products obtained after photon irradiation were plotted as a function of the photon energy. Figure 4.6 represents the relative yield form lower energy range of 4 to 7.4 eV and Figure 4.7 shows the relative yield of the photo-products from energy range of 7 to 14 eV.

Photo-fragments in the lower energy range were only detected for the parent ions, $[P_{1/2}]^{\bullet+}$, with 6 carboxylate ligands in the organic shell of the Zn-MOCs, as shown in Figure 4.6. The relative yield of the photo-fragmented products from the parent; $[P]^{\bullet+} = [P_{1/2}]^{\bullet+}$ for detected fragments of: $[P\text{-}MA]^+$, $[P\text{-}MA+CH_3CN]^+$, $[P\text{-}OH]^+$, $[Zn_3O(MA)_3]^+$, $[Zn_3O(MA)_3+H_2O]^+$ and $[Zn_3O(MA)_2(TFA)+H_2O]^+$ is plotted in Figure 4.6. Upon photon irradiation from 4 to 7.4 eV ligand dissociation products $[P\text{-}MA]^+$ and $[P\text{-}MA+CH_3CN]^+$; and $[P\text{-}OH]^+$ species were detected while no formation of Zn-trinuclear species: $[Zn_3O(MA)_3]^+$, $[Zn_3O(MA)_2(TFA)]^+$ and its water adducts was detected in this range. In addition, no ionized products were detected in lower energy range.

Ligand dissociation products were also predominant in the higher energy range of 7 to 14 eV for the $[P]^{\bullet+} = [P_{1/2}]^{\bullet+}$ parent ions, as shown in Figure 4.7(a) and (b). Additionally, ligand dissociation products from the $[P]^+ = [P_{1/2}\text{-}L_{1/2}]^+$ parent ions were also detected, as shown in Figure 4.7(c) and Figure 4.7(d). Yet, for all the four trapped parent ions, the Zn-trinuclear species $[Zn_3O(MA)_3]^+$ formation was detected above 7 or 8 eV. In the case of $[P_1]^{\bullet+}$, the analogue of $[Zn_3O(MA)_3]^+$ species: $[Zn_3O(MA)_2(TFA)]^+$ and its adduct with water was also detected. The relative yield of both the dissociation product and the ionized products as a function of photon energy is shown in Figure 4.7. At higher energies above 12 eV formation of ionized species from all four parent ions and its water adducts was also observed.

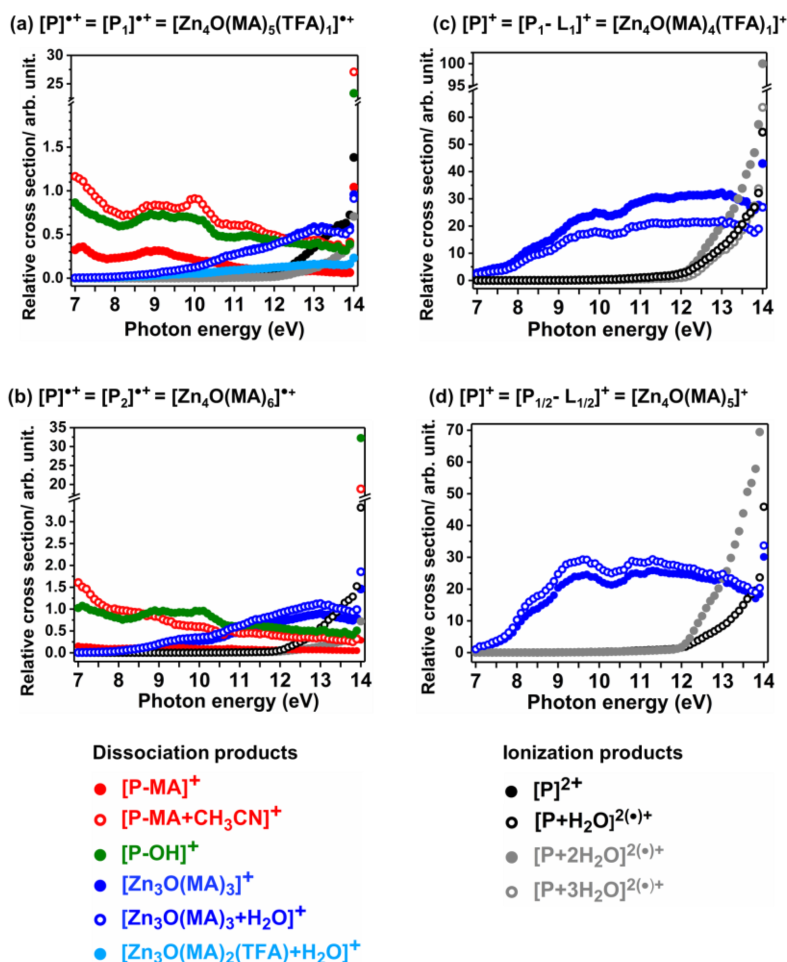

Figure 4.7: Photon-normalized ion yield of the products formed from their respective parent ions.

The proposed photo-fragmentation reactions from all the four parent ions combined are shown in Figure 4.8. We presume that when more than one ligand is lost from the organic shell of the oxocluster, the inorganic core is destabilized, as one of Zn atom in the tetranuclear structure is left with only one bridging carboxylate ligand. Thus, the tetranuclear cluster has an excess of positive charge. Consequently, one of the Zn atoms is lost, along with the ligands. This is why $[P\text{-}MA]^+$ type, or $[P\text{-}OH]^+$ products are not seen in Figure 4.7(c) and (d) for the parent ion $[P_1\text{-}L_1]^+ = [Zn_4O(MA)_4(TFA)_1]^+$ and $[P_{1/2}\text{-}L_{1/2}]^+ = [Zn_4O(MA)_5]^+$.

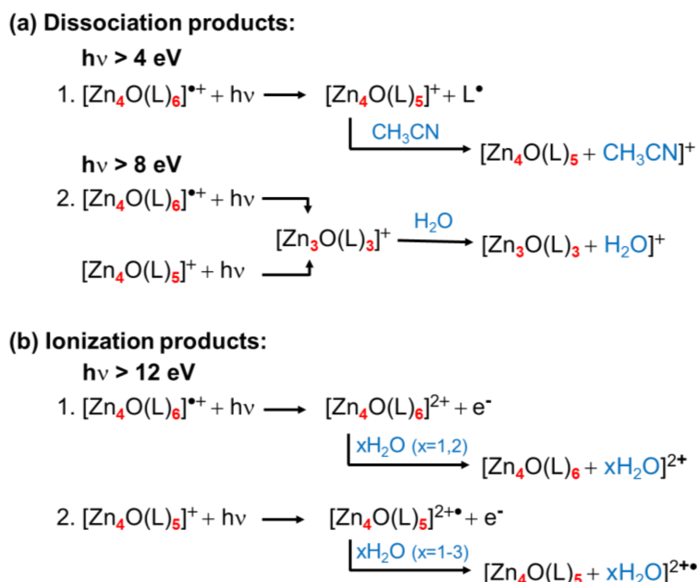

Figure 4.8: Proposed photo-fragmentation reactions of the parent ions.

The onset of the second photo-ionization for all the four trapped parent ions and related adducts with solvent molecules is observed around 12 eV. This result suggests that the ionization energy of the parent ions is determined by the molecular orbitals on the MA ligand. Indeed, the ionization potentials estimated with DFT calculations for parent ions $[P_1]^{\bullet+}$ and $[P_2]^{\bullet+}$ are 11.4 eV and 11.1 eV, respectively and the highest occupied molecular orbital (HOMO) for both the radical cations is mainly located on the MA unit, as shown in Figure 4.9.

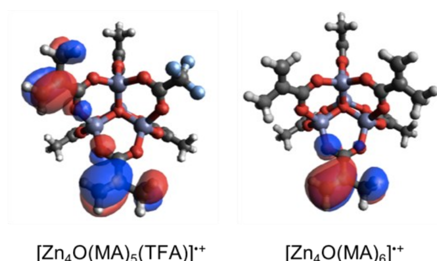

Figure 4.9: Highest occupied molecular orbitals (HOMO) of parent ions $[P_1]^{\bullet+}$ and $[P_2]^{\bullet+}$ calculated with DFT (UB3LYP, Def2TZVP).

4.4 Conclusions

Photo-induced fragmentation studies on the mixed ligand Zn-MOCs, $Zn_4O(MA)_{6-x}(TFA)_x$, exposed to UV/VUV (4 to 14 eV) photons in the gas phase helps to identify the most favourable reaction pathways that this molecular EUV resist follows when it is ionized and brought to different excited states. Ligand dissociation proved to be a main reaction path at energies below the second ionization energy threshold (~12 eV) for the parent ionic species $[P_{1/2}]^{\bullet+}$. However, further ligand dissociations seems to lead to the dissociation of the inorganic core and loss of one Zn atom. Above ~12 eV, second photo-ionization processes compete with the photo-fragmentation ones, which indicates that the energy is used for the emission of an electron rather than for bond dissociation. The presence of the TFA ligand in the organic shell does not seem to influence in the photoionization energy, compatible with HOMO orbitals localized on the MA ligand(s). Despite the fact that the EUV energy is higher than the range of energies used in this study, this work gives fundamental insights into the reactive sites and the stability of the cationic species of $Zn_4O(MA)_{6-x}(TFA)_x$, which can be formed in thin films upon exposure to the ionizing EUV radiation.

5

ROLE OF ELECTRONS IN THE SOLUBILITY SWITCH OF ZINC OXOCLUSTER*

Abstract

The electron-induced chemistry of Zn-based oxocluster with methacrylate (MA) and trifluoroacetate (TFA) ligands for extreme ultraviolet lithography (EUVL) applications is investigated in this Chapter. Electron energies of 80 eV and 20 eV are used which mimics the effect of primary photoelectrons released by the absorption of EUV photons and additional low-energy secondary electrons generated by those primary photoelectrons. The chemical conversion of the resist is studied using mass spectrometry to monitor the desorbing volatile species upon electron irradiation combined with reflection absorption infrared spectra (RAIRS) measured before and after irradiation. The dominant component of the desorbing gas is CO_2, but CO detection also suggests Zn oxide formation during electron irradiation. In contrast, species deriving from the ligand side chains predominantly remain within the resist layer. RAIRS gives direct evidence that, during electron irradiation, C=C bonds of the MA ligands are more rapidly consumed than the carboxylate groups. This supports that chain reactions occur and contribute to the solubility switch in the resist in EUVL. The present results thus provide complementary and new insight to the EUV-induced chemistry in the Zn(MA)(TFA) resist and point towards the important contribution of low-energy electrons therein.

*Published as: M. Rohdenburg, N. Thakur, R. Cartaya, S. Castellanos, and P. Swiderek, Physical Chemistry Chemical Physics, 2021, 23(31), 16646-16657. DOI: 10.1039/D1CP02334A. The electronic supplementary information is available at https://dare.uva.nl/en.

5.1 Introduction

Extreme ultraviolet lithography (EUVL, 13.5 nm) is the state-of-the-art tool for the fabrication of nanoscale devices and the successor of deep ultraviolet (DUV, 193 nm) lithography in the semiconductor industry.[43,162] EUVL aims at pushing the limit of the achievable nanostructure sizes down to the sub-10 nm regime owing to its smaller wavelength.[16] However, to advance EUVL applications, tailored novel materials are currently required.[52,62] This is crucial because the well-known polymer-based photoresists for conventional DUV lithography have low absorption cross sections for EUV photons[57] and the size of the polymer molecules exceeds the targeted structure sizes. Hence, the incorporation of elements (usually metals) into the resist material that can provide higher EUV absorption and a decrease in the size of the resist components is desired. Therefore, in recent years, metal oxoclusters as a class of inorganic-organic hybrid materials have emerged as potential novel photoresists for EUVL applications.[26,57,65] In addition to their enhanced EUV absorption, their small and well-defined size is expected to help in the reduction of variations in the nanopattern features typically measured as line-width or line-edge roughness.[57,62]

A detailed understanding of the chemistry that occurs upon EUV irradiation and leads to the solubility switch of the EUV resist material is needed to design efficient novel EUVL resists.[65,108,163] Compared to conventional DUV (193 nm) lithography, the chemical processes underlying EUVL are more complex.[43] At 193 nm (6.4 eV), the absorption of a DUV photon by the resist only leads to a valence excited state that can then decay in a photochemical reaction to produce a desired solubility switch. In contrast, the initial absorption of an EUV photon (92 eV) primarily leads to emission of a photoelectron leaving behind an ionized cationic site in the resist. Similar to an electronically excited state, this site of the resist is a reactive species and can decay by further chemical conversion. In addition, however, the released photoelectron can trigger a cascade of additional secondary processes. The kinetic energy of the photoelectron depends on the binding energy of the orbital from which it has been removed.[164] As a rough estimate based on typical molecular ionization thresholds, this energy can be as high as 80 eV, when the electrons are ejected from the valence band.[42,106] This allows for the production of additional low-energy secondary electrons (LESEs) with typical energies in the 0-20 eV range when the initial photoelectron is slowed down in the resist.[41,165,166] Both the initial photoelectron and the LESEs can induce additional chemical reactions.[165,167] However, information on the role of such reactive electron-molecule interactions in the processing of the resist in EUVL is sparse.

A few studies have addressed the electron-driven chemistry that is fundamental to the conversion of chemically amplified resists (CARs) during EUV exposure.[151,168–171] In these studies, direct insight in the chemical reactions was

obtained by mass spectrometry (MS) that monitored volatile fragments desorbing from the resist layers during electron exposure. More recently, MS was also applied to investigate the electron-induced chemistry of Sn oxoclusters as an example of metal-containing molecular resist.[163,172] In these studies, electron-stimulated desorption (ESD) experiments revealed that 80 eV electrons can induce fragmentation of ligands from the clusters and showed how the structure of the cluster affects the efficiency for removal of particular ligands upon electron impact.[172]

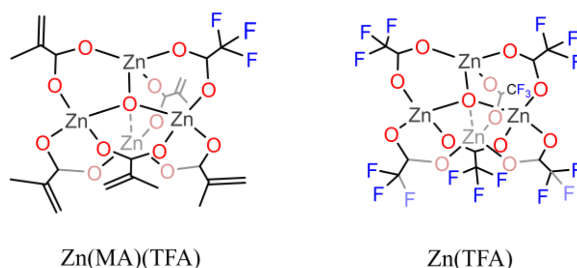

Figure 5.1: Structural representation of Zn(MA)(TFMA) and Zn(TFA) oxoclusters.

As a novel example of metal-oxoclusters, Zn-tetranuclear oxoclusters surrounded by trifluoroacetate (TFA) and methacrylate (MA) ligands (Zn(MA)(TFA)) (Figure 5.1) have been brought forward recently.[71,150] In this type of resist, the solubility switch observed upon EUV irradiation has been explained as an effect of crosslinking of the MA ligands and a low degree of decarboxylation. While the role of electron-induced chemistry has not yet been explored in Zn(TFA)(MA) oxoclusters, a previous study on several Cu carboxylate complexes has revealed that the degradation of the latter materials under electron irradiation is in fact dominated by expulsion of CO_2.[173] This effect was not considered in the previous work on Sn oxoclusters with carboxylate species[174] but might occur as an extra reaction path in metal-oxocluster resists that contain carboxylate moieties and thus benefit or interfere with the solubility switch.

The present study aims at unravelling the chemistry induced in the Zn(MA)(TFA) resist by photoelectrons released upon absorption of EUV radiation and by LESEs to elucidate their role in EUVL. The degradation of the resist when exposed to electron irradiation at relevant electron energies was studied by reflection absorption infrared spectroscopy (RAIRS) and by mass spectrometry (MS) experiments that monitor the electron-stimulated desorption (ESD) of neutral volatile species. For reference, some experiments were also performed on a related Zn-oxocluster Zn(TFA) (Figure 5.1). The electron-induced

reactions observed thereby are in line with the mechanisms deduced recently from spectroscopic studies on the effect of EUV irradiation on Zn(MA)(TFA) resist layers. Furthermore, both ESD and RAIRS results obtained here yield new insights that further support these mechanisms. Overall, we show that not only the absorption of the EUV photon but also the photoelectron released upon absorption as well as LESEs produced by inelastic scattering of the photoelectron induce the characteristic chemical changes in the investigated Zn oxocluster EUVL resist.

5.2 Materials and Methods

5.2.1 Preparation of Zn(MA)(TFA) resist layers

Resist layers of Zn(MA)(TFA) and ZnTFA were spin coated (using Delta 80RC (BM, -T- Model) from SUSS MicroTec) on a silicon substrate (500 µm thick) covered with 5 nm Cr and 40 nm Au layers using a sputter coater (Leica ACE600). The thickness of the spin coated thin films was determined by scratching the layer and measuring AFM on the silicon substrate (without sputter coated Cr/Au layer) and was presumed to be same as on silicon substrate sputter coated with Cr/Au. All the AFM measurements were done using a Bruker Dimensions Icon in ScanAsyst-air mode.

ZnTFA (oxo[hexa(trifluoroacetato)] tetrazinc trifluoracetic acid adduct, CAS 12994899-47-6) was purchased from STREM chemicals and used without further purification. The resist solution of Zn(TFA) (2 w/v %) was prepared in acetonitrile followed by sonication (2 min) and filtration by 0.22 µm PTFE filter. The resist was spin coated onto the substrate at an acceleration of 3000 rpm/s and a speed of 2000 rpm for 30 s. Further a post-apply bake processing of thin films was done at 90°C for 30 s. The thickness of the spin coated thin films was ~14 nm.

Zn(MA)(TFA) was synthesized by following the ligand exchange protocol as described previously.[71] A resist solution of (2 w/v %) was prepared in chloroform and propylene glycol methyl ether acetate (PGMEA), 9:1 v/v solvent mixture followed by sonication for 4 min and filtration by 0.22 µm PTFE filter. The resist layers of Zn(MA)(TFA) were spin coated onto the substrate at an acceleration of 3000 rpm/s and a speed of 2100 rpm for 30 s. Post-apply bake of the thin films was done at 90°C for 30 s. The thickness of Zn(MA)(TFA) thin films for ESD experiments was 12-15 nm.

5.2.2 Reflection absorption infrared spectroscopy

RAIR spectra were acquired with an evacuated FTIR spectrometer (IFS 66v/S, Bruker Optics GmbH) equipped with a grazing incidence reflection unit and a

liquid nitrogen-cooled MCT detector (sensitivity limit down to 750 cm^{-1}). The spectra were collected with a resolution of 4 cm^{-1} and an aperture of 1.5 mm by averaging 400 scans. The sample chamber was evacuated to 5-8 mbar during measurements while the overall system was purged with N_2. A fully deuterated hexadecanethiol (HDT) SAM grown on an Au surface was used as background sample.

5.2.3 Electron irradiation and monitoring of evolving volatile species

Electron irradiation and electron-stimulated desorption (ESD) experiments were conducted in a home-built UHV analysis chamber equipped with a quadrupole mass spectrometer (QMS, SRS RGA 300, mass range m/z 1-300) and a flood gun (Specs FG15/40) for electron exposure.[173,175] Samples were introduced via a preparation chamber which can be separately evacuated and vented for loading of samples. The resist samples were mounted on Cu sample holders and inserted into the preparation chamber. After the pressure in the preparation chamber had dropped to $1x10^{-8}$ mbar, the samples were transferred to the analysis chamber which was continuously kept below $p = 5x10^{-9}$ mbar and covered with a clean Cu mask to reduce ESD from the Cu sample holder. The mask, which is electrically insulated from the sample and held at chamber ground potential, exposes approximately 2 cm^2 of the sample surface to the electron beam.

Electron exposure experiments were conducted at room temperature by either collecting full mass spectra or monitoring selected m/z ratios with an improved time-resolution. The flood gun delivers a defocused electron beam of tunable energy E_0 in the range of 1-500 eV at current densities in the order of 10-30 $\mu A/cm^2$. ESD experiments were conducted at 20 eV which falls within the energy range of LESEs and at 80 eV which is representative of the initial photoelectron released upon EUV absorption. To allow for accurate sample current measurements and thus exposure calculations at 80 eV, the flood gun energy was set to 70 eV and a bias of +10 V was applied to the sample to prevent LESEs produced upon irradiation from escaping. Mass spectra (MS) acquired during electron irradiation have been corrected for contributions of the chamber background vapours by subtracting a MS measured immediately before starting the irradiation. ESD data as function of time were recorded for the most intense signals and are shown without such a correction because the respective signal levels in the background were small. We note that desorption cross sections for neutrals are typically higher than for ions.[176] Therefore, the ESD MS included in here refer to neutral species that have desorbed from the surface. The observed positive ions have been produced in the RGA’s ionizer after desorption and fragment after this ionization step.

5.3 Results and Discussions

5.3.1 Electron-stimulated desorption from Zn(MA)(TFA) and Zn(TFA) resist layers

The electron-stimulated desorption (ESD) of volatile species from Zn(MA)(TFA) and Zn(TFA) resist layers was first studied with an electron energy of 80 eV (Figure 5.2). This energy is characteristic of the most energetic photoelectrons that are typically released by absorption of EUV radiation.[164,166] The data are normalized to the dominant signal ascribed to $CO_2^{\cdot+}$ (m/z 44).

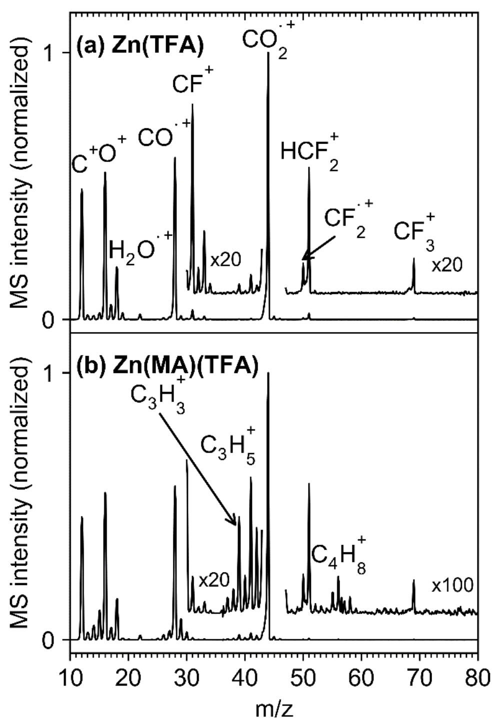

Figure 5.2: Mass spectra revealing the ESD of volatile species that desorb upon electron irradiation (80 eV) from: (a) Zn(TFA) and (b) Zn(MA)(TFA) resist thin film. The incident currents were 30 μA/cm^2 for Zn(TFA) and 34.2 μA/cm^2 for Zn(MA)(TFA). The spectra were acquired within 15 s at the beginning of electron irradiation experiments and are normalised to the intensity of the dominant m/z peak at 44 (CO_2).

Desorption of CO_2 was observed earlier in the ESD from copper carboxylates and explained by ionization, i.e., removal of an electron from the carboxylate group

which leads to expulsion of neutral CO_2.[173,177] Beside m/z 44, ESD is dominated by peaks at m/z 28 ($CO^{\cdot+}$), m/z 16 ($O^{\cdot+}$), and m/z 12 ($C^{\cdot+}$). These latter signals are significantly more intense than expected from the fragmentation pattern of CO_2 measured previously.[177] This indicates that the carboxylate group is not exclusively lost as CO_2 under electron exposure as observed in the case of copper carboxylates[173,177] but fragments further, probably driven by the formation of Zn oxide[150] that was also observed upon electron irradiation in other Zn carboxylates.[178]

Another pronounced signal is at m/z 18 ($H_2O^{\cdot+}$), pointing to desorption of H_2O. ESD of H_2O is present with similar intensity for both the nominally hydrogen-free Zn(TFA) resist (Figure 5.2(a)) and Zn(MA)(TFA) (Figure 5.2(b)). It therefore evidences uptake of water upon handling of the samples under ambient conditions. The relative amount of desorbing H_2O as compared to CO_2 can be roughly estimated based on the ESD intensities (Figure 5.2). The underlying procedure is described in the supporting Information. Based on this procedure and considering that the QMS used in the experiments discriminates high against small m/z ratios (see Supporting Information Figure S5.1), the relative amounts of H_2O and CO_2 that desorb during electron exposure from Zn(TFA) results as roughly 1:30. Note, however, that this underestimates the H_2O content in the samples because H_2O desorbs more slowly (see further on). It can further fragment under electron irradiation and react with components of the resist instead of desorbing. Therefore, H_2O can play a role in the formation of products under electron irradiation.

Figure 5.2 also shows that the intensity of signals ascribed to the desorption of ligand fragments other than CO_2 is generally small. In the case of Zn(TFA) signals at m/z 69 (CF_3^+), 50 ($CF_2^{\cdot+}$), 31 (CF^+), and 19 (F^+) relate to loss of the CF_3 group that is expected upon expulsion of CO_2 from the carboxylate. Although desorption of CF_3 itself cannot be ruled out, such radical species are highly reactive and can be converted to stable products before desorption occurs. In fact, relatively strong signals are also observed at m/z 51 (HCF_2^+) and at m/z 33 ($H_2CF^{\cdot+}$). These latter signals cannot stem from desorbing CF_3 radicals but reveal that the CF_3 group or fragments thereof react with H_2O or the MA ligands to pick up hydrogen prior to desorption. Note that C-F bond dissociation is required for formation of a volatile product that fragments to $H_2CF^{\cdot+}$ when entering the QMS. C-F bond cleavage was also observed when Zn(MA)(TFA) was exposed to EUV radiation[150], supporting the present interpretation. Products such as CHF_3 and CH_2F_2 are conceivable as origin of the signals at m/z 51 and m/z 33. The ESD spectrum shown in Figure 5.2(a) thus represents contributions from different F-containing species. However, the MS signals of CHF_3 and CH_2F_2[179] overlap with different masses of those of CF_3.[180] Considering also that the QMS used in the present experiments discriminates higher masses in favour of lower ones (see Supporting Information, Figure S5.1), reference MS of the anticipated volatile

products measured with the same instrument would be required to estimate the relative amounts of the different desorbing F-containing species. As this is not possible for CF_3, such a quantitative analysis is beyond the scope of this work.

In the case of Zn(MA)(TFA), ESD shows the same signals of fluorinated fragments. However, the ESD rate of CF_3 and of other fluorinated products from the mixed cluster is about five times lower than from Zn(TFA). This reflects roughly the increase in the number of TFA ligands from one in the mixed cluster to six in Zn(TFA). ESD from Zn(MA)(TFA) further produces signals which can be tentatively assigned by comparison with literature MS.[179] The pattern in the range m/z 37 to 42 with prominent peaks at m/z 39 and 41 agrees closely with the MS of propene ($CH_3CH=CH_2$) which derives from the 2-propenyl radical released by loss of CO_2 from the MA ligand. Smaller signals in the m/z 52-58 range point to small amounts of larger products. Here, the most pronounced signals at m/z 55 and m/z 56 are characteristic of compounds with a double bond. The dimerization of two 2-propenyl radicals is a likely explanation although larger fragments of such C_6H_x species are difficult to detect due to the discrimination of higher masses within the QMS. A further small signal at m/z 58 cannot stem from an unsaturated hydrocarbon but may point to an alcohol resulting from reaction of a 2-propenyl radical with H_2O.

The time evolution of the ESD signals for the characteristic m/z ratios gives more insight into the electron-induced chemistry of the Zn oxocluster resist. Figure 5.3 shows such data for a sufficiently long electron irradiation of a Zn(MA)(TFA) resist layer to observe the decay of the ESD signals to baseline levels. The m/z 44 signal represents the desorption of CO_2 while m/z 39 and 41 monitor desorption of a product deriving from the MA ligand, assigned to propene above, and m/z 50, 51, and 69 reveal the desorption of products relating to cleavage of the TFA ligand. Most importantly, all signals relating to the TFA and MA ligands decay with the same rate as CO_2. The relative ESD yields of products emerging from the ligands of the Zn oxoclusters are therefore constant throughout the entire electron irradiation. This indicates that a common process initiates the observed ESD. We propose that this common process is the electron-induced ionization of the resist that results in the decarboxylation of some of the ligands and consequent ejection of CO_2 while leaving behind the rest of the ligand as reactive 2-propenyl and CF_3 radicals. As shown below, most of these radicals remain within the resist layer where they presumably bind to components of the Zn(MA)(TFA) clusters to induce, for instance, crosslinking reactions. A small fraction, however, can desorb as such (see CF_3) or following reactions in the resist that converts them to stable volatile products (see CHF_3 and propene). Figure 5.3(b) reveals a slower decay of ESD of H_2O as compared to ESD of fragments resulting from cleavage of the ligands. This shows that H_2O is a persistent species that can act, for instance, as source of hydrogen in the conversion of the 2-propenyl and CF_3 radicals to the stable products. In fact, previous studies on the

photofragmentation of Zn(MA)(TFA) show that this oxocluster has a quite hygroscopic character since coordinated H_2O molecules were observed when the clusters is brought to the gas phase.[181]

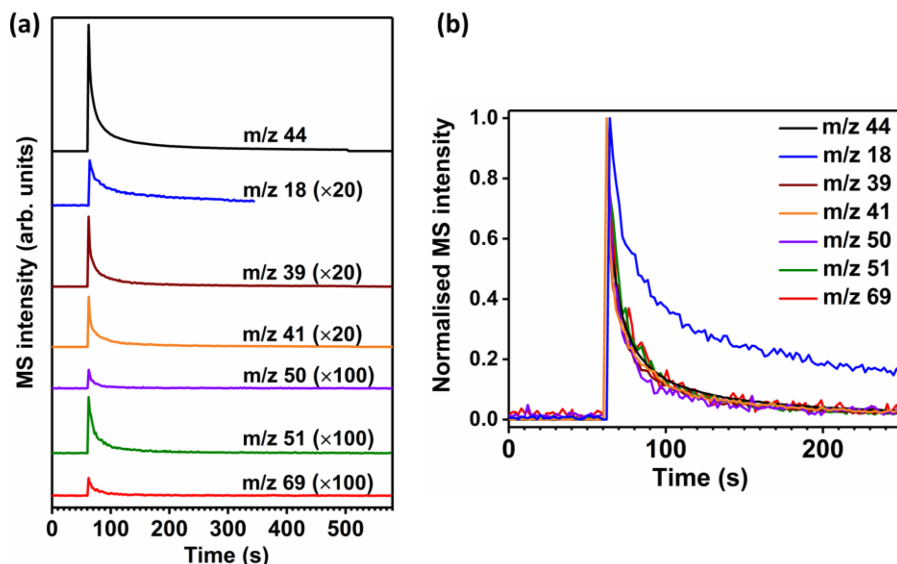

Figure 5.3: (a) ESD curves of the prominent m/z ratios acquired during electron irradiation of Zn(MA)(TFA) thin film upon 80 eV electron irradiation. The signals represent desorption of CO_2 (m/z 44), of the presumed product propene on MA ligand dissociation (m/z 39 and 41), and of CF_3 and related products from TFA ligand cleavage (m/z 50, 51 and 69). The total electron exposure was 15 mC/cm^2. The end of the irradiation is obvious from the small intensity drop at 510 s, clearly visible in the curve of m/z 44, and (b) shows the ESD curves scaled to their maximal intensity.

The relative ESD yields of volatile species deriving from the 2-propenyl and CF_3 radicals as compared to CO_2 were estimated to support that the majority of the radicals released upon loss of CO_2 remains in the resist layer. The details of this calculation are presented in the Supporting Information. Note that a precise quantification is not possible because the assignment of the m/z ratios to specific products is not unique. For instance, contributions of CF_3 radicals overlap with products deriving from them such as CHF_3 and CH_2F_2 deduced above. However, an order of magnitude for this yield can be obtained by assuming as limiting cases that only CF_3 or only CHF_3 desorbs. Under these assumptions, we derive for Zn(TFA) relative yields of 1:5 (CF_3:CO_2) and 1:10 (CHF_3:CO_2) as an upper and lower limit for the desorption of fluorinated products as compared to CO_2. This indicates that the majority of the reactive CF_3 radicals becomes incorporated in

the resist. A similar estimate of the total amount of desorbing hydrocarbon species from Zn(MA)(TFA) was obtained based on the assumption that propene is the dominant product producing the MS pattern seen in the m/z 36 to 42 range. Based on ionization cross sections we arrive at a relative yield of desorbing propene as compared to CO_2 of 1:50 (propene:CO_2). This indicates that, even more than the CF_3 radical, the 2-propenyl radical is predominantly retained in the resist. In conclusion, irradiation of the resist layers with 80 eV electrons leads to dominant desorption of CO_2 and, to a minor extent, of fragments thereof as a result of ligand decarboxylation. However, the majority of the ligand terminal groups released after the ejection of CO_2 remains in the resist layer and most likely contributes to crosslinking between the Zn oxoclusters. This is in line with a mechanism proposed recently according to which the radical species initiate crosslinking reactions.[150]

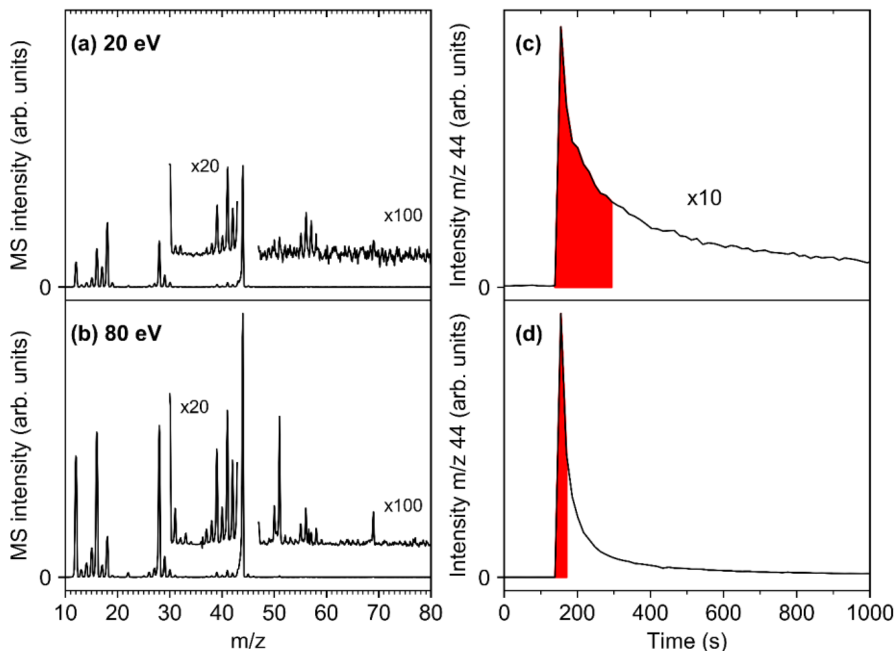

Figure 5.4: Mass spectra revealing ESD of volatile species from Zn(MA)(TFA) resist layers during irradiation with (a) an incident current of 3.9 μC/cm² at 20 eV, and (b) an incident current of 34 μC/cm² at 80 eV. The decay of ESD signal at 44 with irradiation time is shown in (c) for 20 eV, and in (d) for 80 eV. The MS were accumulated during injection of an electron dose of 527 μC/cm² at both energies (marked by red).

The results so far represent the effect of 80 eV photoelectrons as emitted in the resist layer upon absorption of EUV photons. Such photoelectrons can promote further ionization events and thus generate LESEs that might also contribute to the reactions occurring in the resist. We have studied the effect of such LESEs on the resist using an energy of 20 eV. This lies within the typical energy distribution of LESEs[41,165] and, at the same time, warrants a sufficiently high ESD rate. Figure 5.4 compares the ESD data acquired from Zn(MA)(TFA) resist layers during irradiation at 80 eV with an experiment performed at 20 eV. Note that the electron current delivered by the electron gun at 20 eV was an order of magnitude smaller than at 80 eV. To achieve a quantitative comparison, the MS shown in Figure 5.4(a) and (b) have been accumulated over the same electron exposure range at the beginning of irradiation and are plotted on the same scale. This exposure range is marked in red in the time evolution of the dominant m/z 44 ESD signal (Figure 5.4(c) and (d)). Despite the much lower energy, the CO_2 ESD yield at 20 eV still amounts to nearly half of the yield at 80 eV. The same applies to the hydrocarbon fragments from the MA ligands. This remarkably similar ESD rate was also confirmed by a second set of experiments where the integrated m/z 44 signal for a total exposure of 2.5 mC/cm^2 has been evaluated (see Supporting Information Figure S5.2).

In contrast, the intensity of F-containing fragments in ESD is strongly reduced at 20 eV (Figure 5.4(a)). We note that the thickness of the resist layers used in the experiments (12-15 nm) is significantly larger than the typical electron mean free path which is of the order of 1-2 nm at the energies studied here.[166] Slight variations in thickness should thus not have an effect on the ESD results described here. We can conclude from the comparison in Figure 5.4 that the efficiency of 20 eV LESEs in initiating ligand fragmentation is lower but still within the same order of magnitude as in the case of the initial 80 eV photoelectrons. LESEs therefore make a noticeable contribution to the conversion of the Zn oxocluster resists investigated here and very likely also for similar types of metal oxocluster resists.

5.3.2 RAIRS of Zn(MA)(TFA) and Zn(TFA) resist layers

The ESD results are complemented by RAIRS that monitors the material which remains in the resist layers after electron irradiation. As reference for the irradiation experiments, Figure 5.5 compares the RAIR spectra of pristine resist samples of Zn(MA)(TFA) and Zn(TFA). Based on a close similarity with the spectrum of sodium trifluoroacetate,[182] the bands in the spectrum of the Zn(TFA) sample are assigned as:

RAIR Zn(TFA): ν_{as}(TFA,CO_2) (1683 cm^{-1}), ν_s(TFA,CO_2) (1456 cm^{-1}), ν_s(CF_3) (1223 cm^{-1}), ν_{as}(CF_3) (1168 cm^{-1}), ν(TFA,CC) (853 cm^{-1}), δ(CO_2) (799 cm^{-1}), and $\delta_{umbrella}$(CF_3) (735 cm^{-1}). These bands are also present in the spectrum of the Zn(MA)(TFA) resist layer (see Supporting Information, Table S5.3).

RAIR Zn(MA)(TFA): Additional bands marked by * in Figure 5.5 relate to the MA ligands and are assigned as ν(C=C, 1646 cm^{-1}), $ν_{as}$(MA, CO_2, 1595 cm^{-1} and 1569 cm^{-1}), $ν_s$(MA, CO_2) coupled with the δ(CH_2) and δ(CH_3) (1427 cm^{-1} and 1375 cm^{-1}), ν(C-C) + ρ(=CH_2) (1244 cm^{-1}), ω(CH_3, 1009 cm^{-1}), & ω(CH_2) (944 cm^{-1}) based on the close agreement with the spectrum of $Zr_4O_2(MA)_{12}$ clusters[64] and a previous analysis[71] and CH_2 bending mode (835 cm^{-1}).[183]

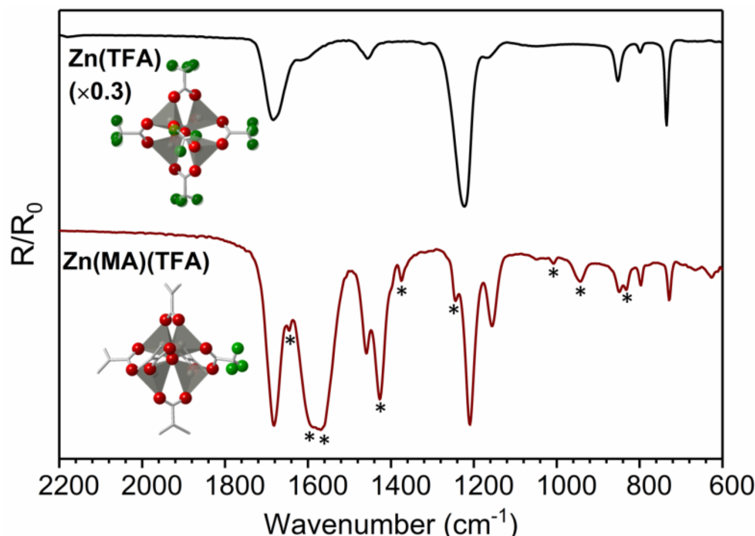

Figure 5.5: RAIR spectra of pristine Zn(TFA) and Zn(MA)(TFA) thin films. Bands related to MA ligand are marked by *. In the 3D representation, grey tetrahedra represent the coordination geometry of the Zn^{2+} atoms (grey spheres in the center), red spheres represent oxygen atoms, green spheres represent fluorine atoms, and grey sticks are chemical bonds.

5.3.3 Electron-stimulated conversion of Zn(MA)(TFA) resist layers monitored by RAIRS

The effects of electron irradiation at 80 eV and 20 eV were monitored on a series of Zn(MA)(TFA) resist samples by recording RAIRS before and after electron exposure. For reference, some experiments were also performed with Zn(TFA) samples. Representative data are shown in Figure 5.6 while all spectra are presented in the Supporting Information, Figures S5.3 and S5.4. The electron exposures of 0.2 mC/cm^2 at 80 eV and 1.0 mC/cm^2 at 20 eV corresponds to an energy input of 16 mJ/cm^2 and 20 mJ/cm^2, respectively. These values are close to the doses that are required in EUVL to achieve the solubility switch in the Zn(MA)(TFA) resist.[150] Despite the different electron energy but in line with the

similar energy input, the intensity reduction in the RAIR spectra is comparable for these two electron exposures, indicative of a remarkable contribution of LESEs in the resist conversion.

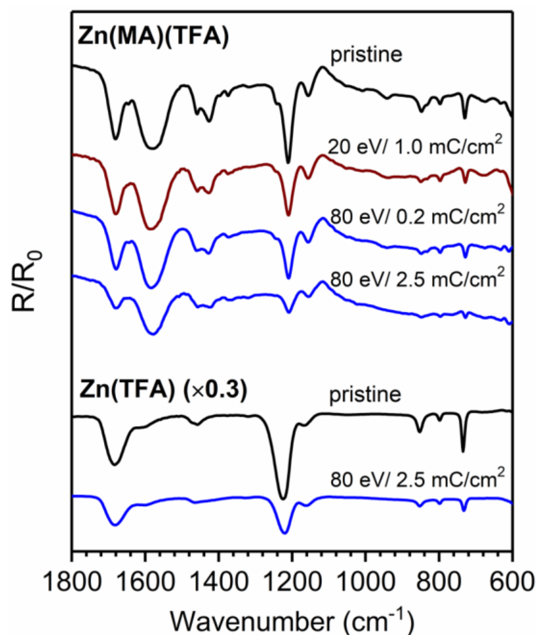

Figure 5.6: RAIRS of 12 nm Zn(MA)(TFA) and 14 nm Zn(TFA) resist layers recorded before (pristine) and after electron irradiation at 80 eV and 20 eV.

Notably, a strong decay of the ν(C-C) + ρ(=CH_2) vibration at 1244 cm^{-1} is observed at both energies, indicative of the rapid consumption of C=C double bonds. This band was not resolved previously,[150] so that the present results provide new direct support of the proposed reaction mechanisms regarding the crosslinking reactions that underlie the solubility switch of the Zn(MA)(TFA) resist (see Section 5.3.5). In addition and as shown in Figure 5.6 by data for 2.5 mC/cm^2 at 80 eV, the conversion of both Zn(MA)(TFA) and Zn(TFA) resist layers under electron irradiation clearly continues beyond the exposures that correspond to typical EUVL doses. This is again in contrast to the FTIR results obtained previously from the EUV irradiated resist (Chapter 3).[150] We note, however, that the spectra do not provide evidence for specific new products despite the fact that the majority of the ligand side groups remain in the resist layer according to the ESD results. This points to the formation of a rather unspecific material with differing vibrational signatures that spread over a wide range of wavenumber or to new functional groups with bands that lie outside of

the range of wavenumbers accessible with RAIRS. For instance, the loss of CF_3 stretching bands ($\nu_s(CF_3)$ at 1223 cm^{-1} and $\nu_{as}(CF_3)$ at 1168 cm^{-1}) points to C-F bond dissociation. Such dissociation is in line with the appearance of fragments ($H_2CF^{\cdot+}$) in ESD (see Section 5.3.1) and has also been confirmed by previous XPS results on EUV-irradiated Zn(MA)(TFA) that revealed the formation of Zn-F bonds in the thin films.[150] Also, the pattern of the C-H stretching bands changes after prolonged electron irradiation (see Supporting Information, Figure S5.5) indicating that the structure of the MA hydrocarbon group is modified.

To evaluate the decay of the vibrational signatures after electron irradiation quantitatively, the integrated intensity of characteristic bands relating to the MA ligands and to the TFA ligands are plotted as function of electron exposure in Figure 5.7. The RAIRS intensities were obtained by integration of Gaussians fitted to the individual peaks as shown in the Supporting Information, Figure S5.6. The ESD intensities were obtained by normalising the m/z 44 signal to the value obtained at the start of the irradiation (Figure 5.4 for Zn(MA)(TFA)). In fact, the characteristic MA band ν(C-C) + $\rho(=CH_2)$ at 1244 cm^{-1} decays most rapidly in line with a rapid crosslinking. In contrast, $\nu_{as}(MA,CO_2)$ at 1595 cm^{-1} and 1569 cm^{-1} decays at a lower rate which implies that a single loss of CO_2 from the MA ligands is accompanied by loss of more than one double bond. The double bond of the MA ligands is thus not merely lost by release of a 2-propenyl radical but also through additional reactions. Such a difference is not seen for the TFA ligand. Instead, $\nu_{as}(TFA,CO_2)$ at 1683 cm^{-1} and $\nu(CF_3)$ 1223 cm^{-1} and 1168 cm^{-1} decay at a similar rate in both resists and at both electron energies indicating that the loss of the CF_3 groups is related to the expulsion of CO_2 alone. The underlying reaction mechanisms are discussed in detail in Section 5.3.5.

We note that the RAIRS signals do not decay towards baseline levels within the investigated range of exposure of up to 7.5 mC/cm^2 while ESD of CO_2 (included as crosses in Figure 5.7) nearly does so. This reflects the limited penetration depth of the electrons resulting from the very small mean free path that is typically below 1 nm at the investigated electron energies.[166] ESD is a surface process and thus reflects the material that is lost from the topmost part of the resist while RAIRS probes the entire layer and thus also material that is less efficiently reached by the electron beam accounting for the remaining intensity after 7.5 mC/cm^2 (Figure 5.7). The somewhat slower decay of $\nu_{as}(TFA,CO_2)$ 1683 cm^{-1} and $\nu(CF_3)$ at 1223 cm^{-1} and 1168 cm^{-1} from Zn(TFA) (see also Supporting Information, Figure S5.3 and S5.4) as compared to Zn(MA)(TFA) most likely reflects the slightly larger thickness of Zn(TFA) but may also be an effect of different electron scattering probabilities in the two materials that can, however, not be quantified here.

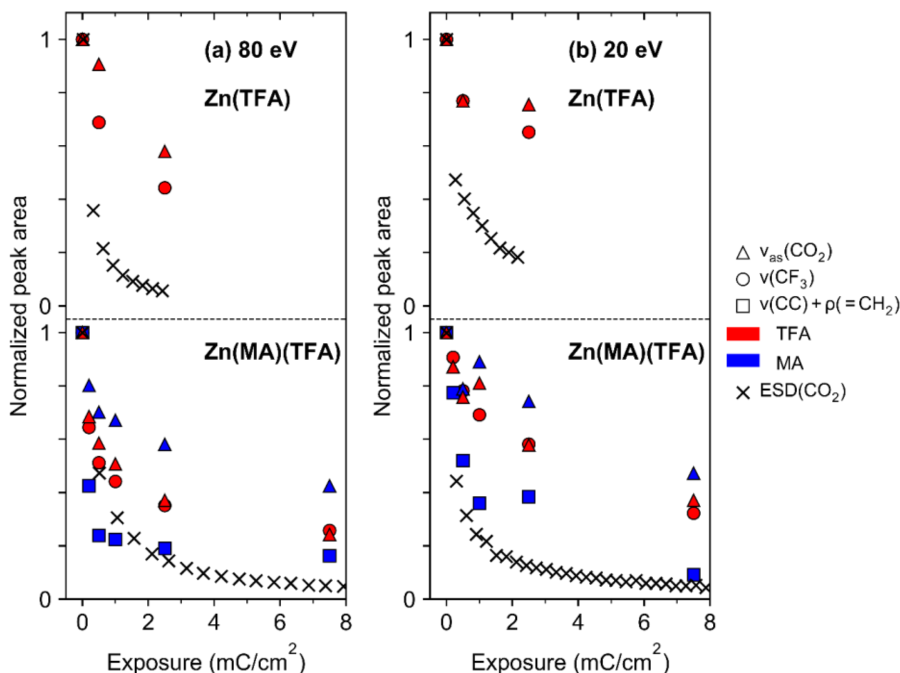

Figure 5.7: Evolution of the characteristic MA and TFA RAIRS bands with electron exposure at (a) 80 eV and (b) 20 eV for Zn(TFA) (top) and Zn(MA)(TFA) (bottom). To enhance the readability, the number of ESD points displayed were reduced to 20% (Zn(TFA), 80 eV and Zn(MA)(TFA), 20 eV) and 3% (Zn(TFA), 20 eV), respectively.

5.3.4 Comparison with the EUV results

The present results complement the EUV irradiation study of Zn(MA)(TFA) resist samples[150] by revealing that a typical photoelectron released upon absorption of an EUV photon, represented here by electron irradiation at an energy of 80 eV, induces similar chemical changes in the sample as the actual photoabsorption and consequent ionization process. The effect at 20 eV, i.e., for electrons with an energy in the upper part of the range characteristic of LESEs, is somewhat weaker but still remarkable. The ESD data and the changes in RAIRS following electron irradiation thus give compelling evidence that not only the initial 80 eV photoelectron but also lower energy LESEs contribute to the processing of the Zn oxocluster resists.

As also seen for the previous EUV irradiation study of Zn(MA)(TFA) resist layers[150] (Chapter 3), carboxylate bands and vibrations relating to the CF_3 groups in RAIRS lose intensity upon electron irradiation (Figure 5.7). Based on this decay, we can compare in a semiquantitative manner the effect of EUV

absorption and electron irradiation. Following an incident EUV dose of 85 mJ/cm^2, the carboxylate bands were observed to decay by roughly 20%.[150] Based on the linear EUV absorption coefficient of 12.4 μm^{-1} of the Zn(MA)(TFA) resist[71] and considering that the thickness of the samples used in EUV irradiation amounted to 25-30 nm, the EUV transmission through the resist is roughly 70% and consequently the estimated absorbed energy is 26 mJ/cm^2. The energy input to the sample during an electron exposure of 0.2 mC/cm^2 at 80 eV is even smaller (16 mJ/cm^2) but leads to a 25-30% decay of the carboxylate bands (Figure 5.7(a)). Similarly, an intensity loss around 20% was also observed after an electron exposure of 1 mC/cm^2 at 20 eV (20 mJ/cm^2). Considering further that not even the entire resist layer is processed under electron irradiation due to the limited penetration depth of the low-energy electron beam, this underlines that the contribution of photoelectrons and LESEs to the conversion of the Zn(MA)(TFA) resist is substantial.

As observed above and most clearly visible upon electron irradiation at 80 eV, the intensities of most RAIRS bands of the Zn(MA)(TFA) resist continue to decay beyond the typical energy input required for solubility switching in the EUVL process (Figure 5.7(a)). This gives evidence of continued cleavage of the carboxylate groups. In contrast, the intensities remained constant when the EUV irradiation was extended beyond an incident dose of 85 mJ/cm^2 (Chapter 3).[150] We speculate that this different response to the EUV and electron irradiation may be an effect of a different charge state of the sample. While EUV absorption can lead to accumulation of positively charged ions in the resist layer which decreases the efficiency of further ionization, an impinging electron beam can compensate for such a charging effect[184] and thus enable continued conversion of the sample.

5.3.5 Reaction mechanism

The chemical changes that occur in Zn(MA)(TFA) resists upon absorption of EUV radiation were recently studied by FTIR, UV-vis spectroscopy, as well as XPS techniques. Based on these results, a reaction scheme for the conversion of the resist was conceived in Chapter 3.[150] Briefly, it was proposed that absorption of an EUV photon leads to emission of a photoelectron and formation of a radical cation of the Zn oxocluster which then decays by expulsion of CO_2 releasing an organic radical (2-propenyl or CF_3). The latter can initiate crosslinking between the clusters by adding to the C=C double bond of an intact MA ligand. Furthermore, based on the formation of Zn-F bonds seen in XPS, it was proposed that LESEs with near-thermal energy can attach to the Zn oxocluster to initiate C-F bond cleavage by dissociative electron attachment (DEA).[146] This releases F^- ions which then bind to vacant Zn sites in the oxo-core. The present results reveal that electron irradiation induces a closely related chemistry in the Zn(MA)(TFA) resist. In addition, the ESD and RAIRS results provide new details about the

reactions in the resist. This is summarized in the extended reaction sequence shown in Figure 5.8 and discussed in detail further on.

The present ESD data reveal, in line with earlier studies on different carboxylate compounds,[173,179] that CO_2 is in fact the dominant outgassing species. This is also the first time that the release of CO_2 from Zn(MA)(TFA) is directly observed. 80 eV is within the energy range were electron impact ionization (EI) is most efficient.[165] It is thus plausible that impact of a photoelectron released upon EUV absorption will induce the same sequence of reactions as the actual EUV absorption. Therefore, the present results are also relevant to the EUVL process itself. As expected from the general energy dependence of EI, the yield of CO_2 is lower at 20 eV but still significant. At both energies, we observe, however, that CO desorbs as a by-product. As shown in Figure 5.8, we propose that this is accompanied by formation of Zn-O bonds. This decarboxylation channel was not previously considered for Zn(MA)(TFA) but has been reported to lead to formation of Zn oxide upon electron irradiation of Zn acetate ($Zn_4O(CH_3COO)_6$)[185] and of a Zn-based metal organic framework.[178] The loss of a carboxylate ligand from Zn(MA)(TFA) yields a structure that is related to oxygen vacancies at the surface of ZnO.[186] Such oxygen vacancies have been shown to enhance the reduction of CO_2 to CO at the surface of ZnO electrocatalysts.[186] We propose that a similar reactivity leads to the formation of CO as observed here. In fact, a previous study of photofragmentation pathways of Zn(MA)(TFA) in the gas phase[181] revealed that the loss of one ligand due to dissociative ionization led to products with m/z values that would be in agreement with loss of CO and one oxygen atom remaining in the cluster.

However, these species overlap with products in which H_2O molecules coordinate to the cation resulting after loss of a ligand. We also note that the structure of the Zn oxocluster after release of CO as proposed in Figure 5.8 is tentative. Further theoretical studies would be needed to confirm this reaction pathway but are beyond the scope of the present work. However, considering the high electronegativity of oxygen, it is conceivable that the positive charge can also be localized on the ligand side group after fragmentation and that the oxygen can capture a further electron upon encounter with a radical species.

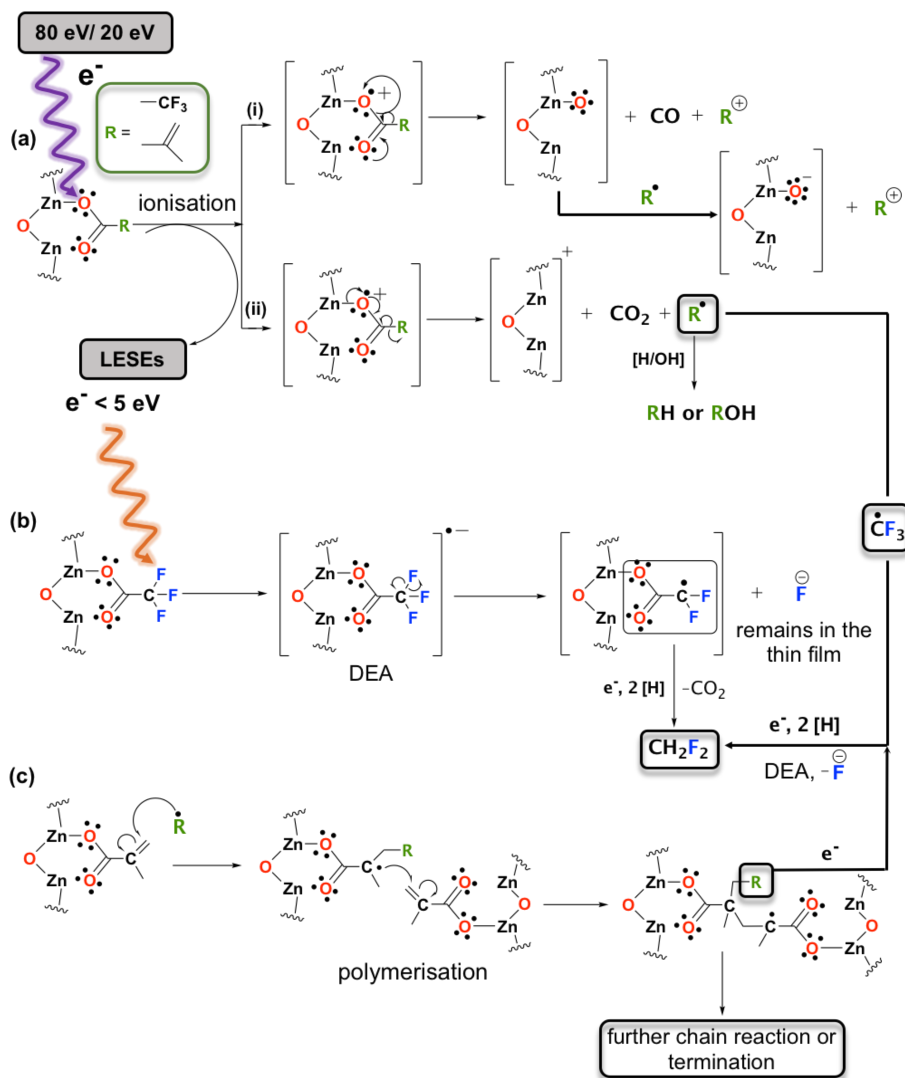

Figure 5.8: Proposed reaction mechanism for Zn oxoclusters exposed to 80 eV & 20 eV electrons: (a) ionisation of the Zn oxocluster followed by fragmentation of a ligand leading to (i) loss of CO and formation of a cation, (ii) loss of CO_2 and formation of a radical: ionization leads to the generation of LESEs, (b) interaction of LESEs (<5 eV) with surrounding Zn oxoclusters and fragmentation via DEA, and (c) radical-initiated chain polymerization reaction in the resist layer. For simplicity, only part of the Zn oxocluster where the ligand dissociation occurs is shown and the carboxylate ligand is represented as a monodentate ligand. Note that this represents a particular mesomeric structure, radical sites and positive charge after ionization can be delocalised.

ESD also evidences that ligand side groups desorb in fact to a much smaller extent than CO_2. This supports that the 2-propenyl and CF_3 radicals released upon expulsion of CO_2 or CO react in the resist as proposed recently.[150] The present RAIRS results also provide direct evidence that the C=C double bonds of the MA ligands are more rapidly consumed than the carboxylate groups. The intensity of the ν(MA,C-C) + ρ(=CH_2) band was not reported before so that its rapid decay observed (Figure 5.7) is a particularly important result. For instance, an electron exposure of 0.5 mC/cm^2 at 80 eV is sufficient to reduce the intensity of this band by roughly 75% while the intensity of the MA carboxylate bands still amounts to roughly 2/3 of their initial intensity. This indicates that more than one C=C double bond is lost per cleaved carboxylate and supports the reaction mechanism proposed previously for EUV irradiation[150] and extended in Figure 5.8.

Based on the close correlation between the analytical results obtained previously for Zn(MA)(TFA) resists following EUV absorption[150] and the present results for electron irradiation we can conclude that, regardless of the incident particle, the most important events defining the chemistry are ionization and the generation of secondary electrons. This was also stressed recently with regards to the related Hf oxocluster EUVL resists.[183] Note here that 20 eV and 80 eV electrons have energies well above typical ionization thresholds. In all cases, the primary interaction expected between these electrons and the thin film is thus the ionization of the molecules in the film. However, a larger number of LESEs will be produced by an 80 eV electron than at 20 eV which rationalizes the lower reaction rate at 20 eV.

A difference between the reactions induced by 80 eV and 20 eV electrons is that desorption of F-containing species is more strongly reduced at 20 eV than the outgassing of other products (Figure 5.4). This may relate to differences in the ionization energy and energy-dependent cross sections of fluorinated and non-fluorinated ligands. For instance, the ionization energies of methacrylic acid and trifluoroacetic acid are reported as 10.15 eV and 11.5 eV, respectively.[187] This brings the fluorinated compound closer to the threshold than the non-fluorinated compound leading to a smaller ionization cross section. This is more clearly revealed by comparing the available total electron impact ionization cross sections for propene and the CF_3 radical as model for the MA and TFA ligands. While the cross section for propene drops by roughly a factor of three from 8.819 Å^2 to 3.069 Å^2 when the electron energy is decreased from 80 eV to 20 eV, it decreases by nearly a factor of ten from 4.782 Å^2 to 0.502 Å^2 in the case of CF_3.[188] Note also that a lower electron energy will release less LESEs. In particular, near-thermal LESEs can induce cleavage of C-F bonds by DEA.[146] C-F bond dissociation is evidenced here by the m/z 51 (HCF_2^+) and m/z 33 (H_2CF^+) signals in ESD and also in line with formation of Zn-F seen in XPS.[150] The strong suppression of the m/z 51 and m/z 33 ESD signals at 20 eV can thus also relate

to a lower yield of LESEs. The present results do not allow us to distinguish between C-F bond dissociation in the TFA ligand prior to loss of CO_2 and dissociation of the CF_3 radical after loss of CO_2. In fact, DEA has also been reported for the CF_3 radical.[189] Therefore, both reaction pathways are tentatively included in Figure 5.8.

5.4 Conclusions

The electron-induced chemistry of the novel Zn oxocluster, Zn(MA)(TFA) as EUVL resist has been studied under irradiation with electron energies of 80 eV and 20 eV. The former energy is representative of photoelectrons ejected from the cluster upon absorption of an EUV photon, while 20 eV falls within the range of energies that is characteristic of low-energy secondary electrons produced by interaction of the initial photoelectron with the clusters. The results reveal that the chemistry induced by electrons is closely related to the effect of EUV photon absorption. In fact, for an energy input that is comparable to typical doses in the range of the EUVL process (dose to size, 20 mJ/cm^2), a similar conversion of the resist was achieved under electron irradiation.

Both electron energies promote ionization of the resist leading to the desorption of volatile decomposition products. The dominant component of the desorbing gas is CO_2. Remarkably, even 20 eV electrons are fairly efficient and still evolve near 50% of the amount of gas that is observed for the same electron dose at 80 eV. Notably, CO is also produced pointing to formation of Zn oxide in the thin films. In contrast, only small amounts of species deriving from the ligand side chains desorb, indicating that they predominantly remain within the resist layer. However, species such as m/z 51 (HCF_2^+) and m/z 33 (H_2CF^+) seen in MS support that C-F bond cleavage occurs under electron irradiation. As an important finding, the present infrared spectroscopic results provide the first direct evidence that C=C bonds are more rapidly consumed than the carboxylate groups following ionization and consequent expulsion of CO_2. This supports that chain reactions occur. These reactions are held responsible for crosslinking of the clusters and thus to the solubility switch of the resist in EUVL.

Because of the close correlation between EUV- and electron-induced reactions, the present results provide complementary and new insight into the chemistry that occurs in the investigated resist. Overall, we have demonstrated that the contribution of photoelectrons and LESEs to the conversion of the Zn(MA)(TFA) resist and similar resist materials cannot be neglected.

6

FLUORINE-RICH ZINC OXOCLUSTER AS EUV PHOTORESIST*

Abstract

The absorption of extreme ultraviolet (EUV) radiation by a photoresist strongly depends on its atomic composition. Consequently, elements with a high EUV absorption cross section can assist in meeting the demand for higher photon absorbance by the photoresist to improve the sensitivity and reduce the photon shot-noise induced roughness. In this work, we enhanced the EUV absorption of the methacrylic acid ligands of Zn oxoclusters by introducing fluorine atoms. We evaluated the lithography performance of this fluorine-rich material as a negative tone EUV photoresist along with extensive spectroscopic and microscopic studies, providing deep insights into the underlying mechanism. UV-vis spectroscopy studies demonstrate that the presence of fluorine in the oxocluster enhances its stability in the thin films to the ambient atmosphere. However, the EUV photoresist sensitivity (D_{50}) of the fluorine-rich oxocluster is decreased compared to its previously studied methacrylic acid analogue. Scanning transmission X-ray microscopy and in situ X-ray photoelectron spectroscopy in combination with FTIR and UV-vis spectroscopy are used to get insights into the chemical changes in the material responsible for the solubility switch. The results support decarboxylation of the ligands and subsequent radical-induced polymerization reactions in the thin film upon EUV irradiation. The rupture of carbon-fluorine bonds via dissociative electron attachment also offers a parallel way of generation of radicals.

---

*Published as: N. Thakur, M. Vockenhuber, Y. Ekinci, B. Watts, A. Giglia, N. Mahne, S. Nannarone, S. Castellanos, and A. M. Brouwer, ACS Materials Au, 2022. DOI: 10.1021/acsmaterialsau.1c00059. The electronic supplementary information is available at https://dare.uva.nl/en.

6.1 Introduction

The dimensions of the smallest components that can be fabricated using photolithography are directly proportional to the wavelength of the radiation used in the process. Over decades, the wavelength of the imaging light used in the semiconductor industry for photolithography has decreased from g-line (436 nm) to i-line (365 nm) to KrF (248 nm) to ArF (193 nm) immersion lithography (ArFi).[15,62] Presently, extreme ultraviolet (EUV) at 13.5 nm has emerged as the successor of the ArFi as next-generation lithography to reach the industry's objective of patterning feature sizes of 10 nm and below in a cost-effective manner.[16,190]

The steep jump in the wavelength from 193 nm to 13.5 nm has posed numerous challenges and a key factor that will determine the future improvements success of EUV lithography is the choice of the photoresist and its solubility-switching chemistry.[62,191] For UV lithography, organic materials are used as photoresists, and their reactions are based on photochemical acid generation via electronically excited states. The photon energy of EUVL (13.5 nm, ~92 eV), however, is ~14× higher than that of its predecessor, ArF (193 nm, 6.4 eV) and the EUV absorption mechanism and resulting chemical reactions are different. EUV photons are highly energetic and surpass the ionization potential of resist. Thus, the EUV absorption by the material results in ionization and subsequent ejection of photoelectron(s). These electrons have sufficiently high energy to further interact with the neighboring molecules in the thin film giving rise to secondary electron processes.[23,42,106,192] Thus, EUV photon absorption by the resist initiates a cascade of reactions in the thin films[42,108,193] and because of this complexity, understanding the fundamentals is challenging. Moreover, the deconvolution of these events is not straightforward, especially in the thin film samples. Henceforth, the fundamental understanding of the induced chemical changes or reaction path mechanisms upon irradiating the photoresist material with ionizing EUV radiation is crucial.[43]

The primary challenge posed by the conventional organic resists (mainly constituting C, H and O) is their low EUV absorption and this drew the attention of researchers towards incorporating elements (especially metals) having high photon absorption cross section at 92 eV to potentially increase sensitivity and reduce stochastic effects.[26,62,193–196] Our previous studies on a hybrid zinc-based oxocluster, $Zn(MA)_5(TFA)_1$ (MA is methacrylate ligand and TFA is trifluoroacetate ligand, Figure 6.1(a)), demonstrated an EUV linear absorption coefficient of 12 μm^{-1}, much higher than that of traditional organic photoresists (~5 μm^{-1}).[71] Further, mechanistic insights for the solubility switch in Zn(MA)(TFA) photoresist upon EUV exposure using spectroscopic studies demonstrated polymerization of the terminal double bond of MA ligand and formation of fluoride ion species in the thin films from TFA via dissociative

electron attachment (DEA).[150] The same reaction paths were found when the material was irradiated with low energy electrons of 20 eV and 80 eV.[197]

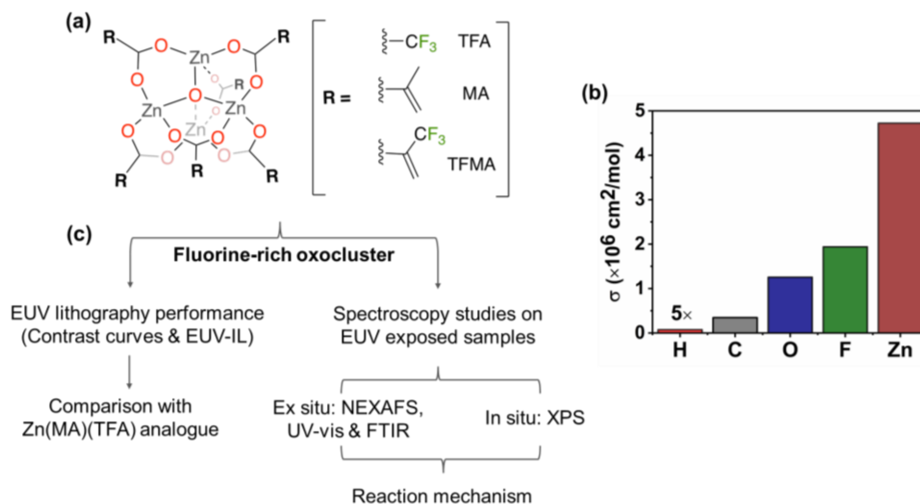

Figure 6.1: (a) Schematic representation of Zn oxoclusters; fluorine-rich oxocluster Zn(TFMA) (average composition $Zn(TFMA)_{5.9}(TFA)_{0.1}$) and Zn(TFMA)(MA)(TFA) (average composition $Zn(TFMA)_{2.4}(MA)_{2.9}(TFA)_{0.8}$) and the previously studied analogue, $Zn(MA)_5(TFA)_1$, (b) EUV atomic absorption cross section at 92 eV of elements H(×5), C, O, F and Zn obtained from the CXRO database,[67] and (c) schematic representation of the study flow for fluorine-rich Zn oxocluster for EUVL applications.

In this work, we study fluorine-rich Zn-based oxoclusters, designed using 2-(trifluoromethyl)acrylate (TFMA) ligand instead of MA. The terminal double bond of the ligand was kept intact to allow polymerization upon EUV irradiation, yet at the same time, more fluorine was introduced. The molar absorption cross section of fluorine at 92 eV is ~26 × larger than that of H and ~5.6 × that of C (Figure 6.1(b)). Hence its incorporation, along with the metals, in the resist material has the potential to increase the EUV absorbance. Moreover, some studies have demonstrated an overall enhanced EUV lithography performance upon the incorporation of fluorine in the photoresist material.[23,49,50,114]

This work focuses on the detailed study of fluorine-rich Zn oxocluster for EUVL application (Figure 6.1(c)) mainly in two ways:

i) investigating the changes in processability, stability of oxocluster in thin film, EUV lithography performance upon fluorine incorporation in comparison with its previously studied Zn(MA)(TFA) analogue,[150] and

ii) monitoring chemical changes on the fluorine-rich zinc oxocluster thin films upon EUV irradiation using near-edge X-ray absorption fine structure (NEXAFS), FTIR and UV-vis spectroscopy and X-ray photoelectron spectroscopy (XPS) studies.

For comparison, we include a mixed-ligand compound Zn(TFMA)(MA)(TFA) with average composition $Zn(TFMA)_{2.4}(MA)_{2.9}(TFA)_{0.8}$ in the study. The present studies reveal that the incorporation of more fluorine in methacrylate-Zn oxoclusters is not a magic bullet. Replacing MA with TFMA did aid in increasing the thin film stability over time, but the formation of smooth thin films on substrates proved to be difficult. Although the EUV absorption of the fluorine-rich oxocluster Zn(TFMA) (Figure 6.1(a)) must be theoretically higher than that of its previously studied analogue Zn(MA)(TFA), the sensitivity (D_{50}) for EUV lithography turns out to be unexpectedly lower. Spectroscopy studies show loss of CO_2 from carboxylate ligand, and a strong decrease of C=C/ C=O fraction as a function of EUV dose supports radical initiated polymerization in the thin film. Furthermore, fluorine migration from the CF_3 groups towards Zn was observed, forming new Zn-F species. This likely occurs via a dissociative electron attachment (DEA) path (low-energy electrons). We believe that the present results enhance our understanding of Zn based fluorine-rich photoresists and similar systems for lithography application and will propel advance focused investigations for fluorine-rich photoresist materials.

6.2 Materials and Methods

6.2.1 Synthesis of fluorine-rich oxocluster: Zn(TFMA) and Zn(TFMA)(MA)(TFA)

In this study fluorine-rich oxoclusters were synthesized from a commercially available precursor having a Zn tetranuclear oxo-core and an organic shell of 6 trifluoroacetate (TFA) ligands, following the same exchange procedure as described in our previous work.[71] The effect of fluorine incorporation in the reactive organic ligands of the Zn-oxocluster was studied by investigating Zn(TFMA) (still containing a minor fraction of TFA, average composition $Zn(TFMA)_{5.9}(TFA)_{0.1}$) and a similar cluster with a mixed ligand shell, Zn(TFMA)(MA)(TFA) (average composition $Zn(TFMA)_{2.4}(MA)_{2.9}(TFA)_{0.8}$), see Figure 6.1(a). The EUVL performance of the materials was compared to the previously studied analogue, Zn(MA)(TFA).[71,150]

Synthesis of Zn(TFMA): Oxo[hexa(trifluoroacetato)] tetrazinc trifluoracetic acid adduct (Zn(TFA); 500 mg, 0.52 mmol, 1 eq.) and 2-(trifluoromethyl)acrylic acid (TFMAA; 870 mg, 6.2 mmol, 12 eq.) were dissolved in acetonitrile and the solution was stirred for 5 hours at 45 °C. The remaining solvent was then evaporated using a rotary evaporator and an oily residue was

obtained. The oily residue was re-precipitated by adding toluene to the residue and evaporating it on a rotary evaporator. The process was repeated about 4-5 times to remove excess of the remaining acid and obtain a white solid product. This was dried in a vacuum oven at 40 °C and stored under nitrogen. The reaction scheme is shown in the SI, Figure S6.1.

^{1}H NMR (300 MHz, DMSO-d_6) δ: 6.52 (1H, =CH_2) and 6.30 (1H, =CH_2).

^{19}F NMR (300 MHz, DMSO-d_6) δ: -73.69 (-CF_3, TFA) and -63.92 ((-CF_3, TFMA); integration of 46.3 and 1.0 of peaks, respectively, showing that most of the TFA ligand in the precursor has been exchanged by TFMA and on average 5.9 TFMA ligand and 0.1 TFA ligand is present in the organic shell of Zn(TFMA) oxocluster.

NMR are shown in Appendix III, Figure AIII.1.

FTIR: 695 (COO angle bending), 828 (s, CH_2 bending mode), 993 and 912 (bending out of plane, γ (CH)C=CH_2), 1130 and 1167 (ν C-F), 1380-1487 (CH_x + ν_s COO), 1583 (ν_{as} COO (TFMA)), 1631 (ν C=C (TFMA) monodentate), 1660 (ν C=C) and 1678 (ν_{as} COO (TFMA) monodentate) cm^{-1}; spectra shown in SI (Figure S6.2).

Mass spectra: the observed isotopic distribution corresponds to the presence of the tetranuclear Zn core of the oxocluster (Figure S6.3). The Zn oxocluster is susceptible to form complexes with acetonitrile (electrospray solvent) also observed in our previous studies.[71,181] The isotopic distribution observed in the mass spectra was assigned to the oxocluster complex: Zn_4O with 5 TFMA ligands and 2 CH_3CN molecules, which is in concordance with simulated spectra using ChemCal.[161]

The deposition of the thin films on substrates of Zn(TFMA) was done by spin coating 2 w/v % of resist solution from $CHCl_3$: PGMEA (7:3, v/v). All thin films were spin-coated at an acceleration of 3000 rpm/s and 2100 rpm speed for 30 s immediately followed by post-application bake (PAB) at 90 °C/ 30 s. The thickness of the thin films obtained using the above parameters on Si substrates is 14-20 nm, determined using atomic force microscopy (AFM), Bruker ScanAsyst-air probe.

Synthesis of Zn(TFMA)(MA)(TFA): Zn(TFA) (500 mg, 0.52 mmol, 1 eq.), 2-(trifluoromethyl)acrylic acid (TFMAA; 270 mg, 3.1 mmol, 6 eq.) and methacrylic acid (MAA; 440 mg, 3.1 mmol, 6 eq.) were used as precursors for the reaction and the same synthesis procedure as described above for the Zn(TFMA) synthesis was used with acetonitrile as solvent.

^{1}H NMR (300 MHz, DMSO-d_6) δ: 6.52 (1H, =CH_2, TFMA), 6.30 (1H, =CH_2, TFMA), 5.85 (1H, =CH_2, MA), 5.36 (1H, =CH_2, MA) and 1.85 (-CH_3, MA); integration of 2.4 (2H, =CH_2, TFMA), 2.0 (2H, =CH_2, MA) and 3.1 (-CH_3, MA) was obtained for peaks.

^{19}F NMR (300 MHz, DMSO-d_6) δ: -73.58 (-CF_3, TFA) and -63.85 (-CF_3, TFMA); integration of 0.30 and 1.0 was obtained for peaks, respectively.

NMR are shown in Appendix III, Figure AIII.2.

From the ^{1}H and ^{19}F NMR analysis of Zn(TFMA)(MA)(TFA) oxocluster the composition of the organic shell was determined as an average of 2.4 TFMA, 2.9 MA and 0.8 TFA. The deposition of the thin films of Zn(TFMA)(MA)(TFA) oxocluster was done by spin coating $CHCl_3$: PGMEA (7: 3, v/v) as the casting solvent for 2 w/v % of resist solution. All thin films were spin-coated at an acceleration of 3000 rpm/s and 2100 rpm speed for 30 s followed by immediate post-application bake (PAB) at 90 °C/ 30 s.

6.2.2 Silanization process

Clean Si substrates were treated with an ozone photoreactor to maximize the reactive terminal hydroxyl groups on the Si substrate surface, immediately followed by a silanization process. Silanes used in this study were: 3-(chloropropyl)triethoxysilane, 3-(mercaptopropyl)trimethoxysilane, 3-(triethoxysilyl)propyl methacrylate, 3-(aminopropyl)triethoxysilane, 1H,1H,2H,2H-perfluorooctatriethoxysilane and Bis(trimethylsilyl)amine (HMDS). Silanization was carried in the liquid phase except for HMDS which was deposited in the vapour phase. For liquid phase silanization a reaction mixture was prepared in 80 ml of 96% ethanol to which a catalytic amount of 99% acetic acid was added to adjust the pH of the solution at ~6. To this solution, 2 ml of silane was added and the clean treated Si substrates were placed in the reaction solution for ~40 minutes at room temperature with constant stirring, washed with ethanol (96%) and dried with nitrogen. The silanized substrates were annealed in an oven at ambient pressure, 130 °C/ 24 hours.

6.2.3 Sample preparation for spectroscopy studies

Two types of substrates were used for near edge X-ray absorption fine structure (NEXAFS) measurements on Zn(TFMA) samples: 1) for reference (unexposed) spectra, a 5 × 5 mm^2 substrate with an array of 5 × 5 free-standing SiN_x windows (0.15 × 0.15 mm^2) was used; and 2) for EUV exposure a 7.5 × 7.5 mm^2 substrates with a SiN_x membrane window (30 nm thick) of 3 × 3 mm^2 was used. Zn(TFMA) was spin coated on the membrane and exposed to EUV photons at different doses (exposed area of 0.5 x 0.5 mm^2 per dose) on a single SiN_x membrane window (3 × 3 mm^2). The substrates were then attached to the sample holder (as shown in Figure S6.5) having holes such that the free-standing windows of SiN_x were on top of those holes for NEXAFS measurements and the measurements were performed in the transmission mode.

For FTIR spectroscopy, thin films were spin coated on double side polished Si substrates (200 μm thick) while for UV-vis analysis the thin films were spin

coated on quartz substrates (500 μm thick). For the XPS study, oxocluster was spin coated on the Si substrate sputter coated with Cr/Au (5 nm/ 40 nm).

6.2.4 EUV Exposures

EUV (13.5 nm) exposures were performed using synchrotron radiation at the Paul Scherrer Institute (PSI), Switzerland at the Swiss Light Source XIL-II beamline for contrast curves, L/S features (EUV-interference lithography, EUV-IL)[126,127] and ex situ spectroscopy measurements. Open frame exposures for contrast curves and NEXAFS measurements were performed over a range of doses, using a 0.5×0.5 mm^2 aperture mask with a pinhole of 30 μm. For FTIR and UV-vis spectroscopy studies exposures were done using a 1.7×1.7 mm^2 aperture mask with a pinhole of 30 μm. EUV-IL was used to test nano-patterning performance using a mask with periodic line/space (L/S) half-pitch (HP) of 50 nm, 40 nm, 30 nm and 22 nm with a pinhole of 70 μm.

6.2.5 Post exposure analysis and ex situ spectroscopy study

A scanning transmission X-ray microscope (STXM) (PolLux beamline[198] at PSI) was used to perform NEXAFS spectroscopy measurements as illustrated in Figure S6.4. The measurements were done under normal incidence using a line scan over a length of 25 μm. The beam was defocused to a spot size of ~1 μm to avoid radiation damage. For each energy, a sample scan was made on the sample, exposed to EUV and developed using diluted 0.1% propionic acid in 2-heptanone for 10 s and a reference scan was made on a nearby area on SiN_x membrane that was cleaned (unexposed photoresist) by the development. Carbon K-edge spectra were recorded for an energy range of 270-350 eV, and different step sizes were used for different regions (270-282 eV; 0.5 eV, 282.1-293 eV; 0.1 eV, 293.25-300 eV; 0.25 eV, 300-350 eV; 0.25 eV). For F K-edge measurements, the energy was scanned from 675-710 eV (675-689; 0.5 eV, 689-704; 0.1 eV, 704-710; 0.5 eV). By repeating scans at the same area, we could show that radiation damage is negligible under these conditions. ATHENA software was used for spectra normalisation and fitting of the C K-edge and F K-edge.

UV-vis spectroscopy was performed on thin films deposited on quartz using a Shimadzu UV2600 spectrophotometer and FTIR was performed in transmission mode under vacuum using a Bruker Vertex 80v spectrometer. The samples for UV-vis and FTIR spectroscopy were not developed after exposure.

A Bruker Dimension Icon AFM was used for thickness measurements to obtain contrast curves and inspect the thin film quality or line/space (L/S) pattern printed on Si substrates in Bruker ScanAsyst-air mode.

Top-down SEM images of L/S patterns were recorded using a FEI Verios 460 scanning electron microscope operating at a current of 100 pA and a voltage of 5.0 kV.

6.2.6 In situ XPS study

EUV exposure and XPS measurements were performed at the BEAR beamline of the ELETTRA synchrotron radiation facility, at a base pressure of 10^{-9} mbar.[199,200] The sample was exposed to 13.5 nm, using a silicon filter for higher order rejection, the monochromator deviation angle at 155.2°, the polarization selector at ±0.3 mrad and the vertical slits at 50 µm. High-resolution XPS was acquired with the full beam and no filter. A sample was exposed to 92 eV for a range of doses at different spots (50 × 300 µm) and subsequently, XPS was measured at the exposed spots. The incident dose at 92 eV was determined in a separate scan by measuring the number of photons reaching the sample with the same beamline parameters used for the exposure using an absolute photodiode (AUXUV100 by OptoDiode corp.). The binding energy (BEs) of the core levels were referenced to the C-F peak at 292.81 eV for C(1*s*) and 688.21 eV for F(1*s*) as an internal reference to calibrate the binding energy scale of each spectrum.[150] A bias of -50 eV was applied to the sample and a pass energy of 10 eV for the electron analyzer (ORTEC 996) and a step size of 0.2 eV were used. XPS was acquired for C (1*s*), O(1*s*) and F(1*s*) with photon energies of 400 eV, 650 eV and 800 eV, respectively, and fresh spots on the thin films were used for each exposure followed by XPS measurements. The XPS spectra were fitted using UNIFIT 2008 software.

6.3 Results and Discussions

6.3.1 Processability and stability studies

Compared to the previously studied Zn(MA)(TFA), the solubility of the new fluorine-rich oxocluster Zn(TFMA) was increased in most organic solvents, especially in $CHCl_3$ which was used for casting thin films. In the case of Zn(MA)(TFA), a saturated solution (2w/v % in $CHCl_3$:PGMEA, 9:1 v/v) had to be used, which limited the control over the thin film thickness of the resist. The increased solubility of fluorine-rich Zn(TFMA) allows for varying the thickness of the thin resist films.

In addition, the stability of fluorine-rich Zn(TFMA) thin films to ambient conditions was also enhanced. Since some studies presented in our work are conducted ex situ the material stability over time plays a vital role for analysis. To track the chemical changes in the terminal double bond (π to π* transition, ~190 nm) of the TFMA ligand under ambient conditions, UV-vis spectroscopy was used. The absorption band of the double bond hardly changes for up to 5 hours (shown in Figure S6.6) at ambient conditions. Some loss in the absorption band was observed after 7 hours, possibly due to polymerization of the double bonds. Moreover, the absorption band shape was not severely affected as was observed in the case of its analogue Zn(MA)(TFA).[71] This increase in the stability

of Zn(TFMA) thin film over its analogue Zn(MA)(TFA) can be attributed to the more hydrophobic nature of the material due to the presence of fluorine.

6.3.2 Thin films and Contrast curves

Thin films of the trifluoromethacrylate-containing Zn oxoclusters could be used for EUV exposure experiments, but they showed irregularities (Figure S6.9) that are probably related to poor adhesion to the substrate. Efforts were made to prevent this undesirable behaviour by varying the surface energy of the substrate prior to spin coating by functionalization using silanes: 3-(mercaptopropyl)trimethoxysilane, 3-(triethoxysilyl)propyl methacrylate, 3-(aminopropyl)triethoxysilane and 3-(chloropropyl)triethoxysilane. Water contact angles (Θ_c) of the substrates coated with these silanes were 26, 44, 46 and 65°, respectively. Unfortunately, none of these attempts leads to the formation of high-quality thin films (Figure S6.7). In addition to the silanes mentioned above, Si surfaces were functionalized/modified using 1H,1H,2H,2H-perfluorooctatriethoxysilane (Θ_c = 88°), HMDS and hydrogen fluoride (HF, 2%; dip for 1 min), but no continuous thin film was obtained on the modified substrates.

The incorporation of fluorine in the resist material was anticipated to increase the EUV absorption of the material, which is expected to improve the EUVL performance of the photoresist. The EUV absorption coefficient of the Zn oxoclusters was estimated from the elemental absorption cross section at 92 eV using the CXRO database and the relative amount of each element in the oxocluster, and the estimated density.[48,201] The density of the Zn(TFMA) and Zn(MA)(TFA) oxoclusters was estimated using the molecular weight of the respective oxocluster and its CPK molecular volume calculated using Spartan 18. A scaling factor of 2 was used, based on the comparison of calculated and experimental densities for the acetate and pivalate clusters.[202,203] The estimated EUV absorption coefficient obtained through this for Zn(TFMA) and its analogue Zn(MA)(TFA) are 14.3 μm^{-1} and 10.6 μm^{-1}, respectively. The latter agrees well with the experimentally determined value of 12.4 μm^{-1}.[71]

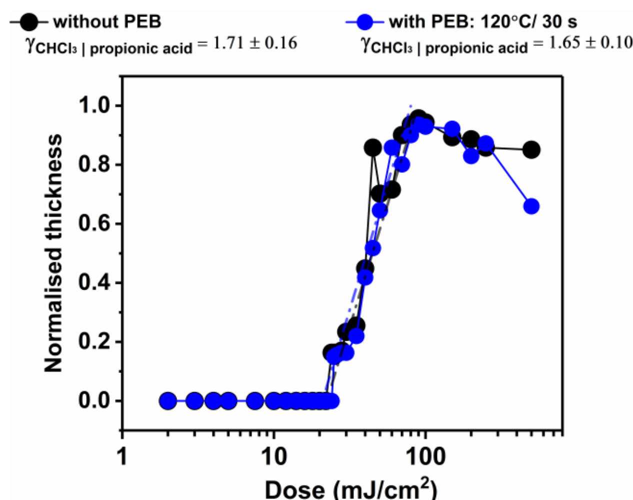

Figure 6.2: Contrast curves for Zn(TFMA) thin films using $CHCl_3$: PGMEA as casting solvent and developed using propionic acid (0.05%) in $CHCl_3$ for 8 s. Thicknesses are normalised relative to the thickness of the unexposed thin film (~14 nm). The contrast values γ are the slopes of the curves between D_0 and ~D_{90}.

The sensitivities of the fluorine-rich oxoclusters for EUV photons were quantified experimentally using the contrast curves (exemplified in Figure 6.2) and were compared to its analogue Zn(MA)(TFA) which exhibited high sensitivity in our previous studies. The performance of the Zn(TFMA)(MA)(TFA) oxocluster was also studied using contrast curves and is shown in SI, Figure S6.8. Table 6.1 summarizes the results from contrast curves of three Zn-oxoclusters with increasing fluorine content: Zn(MA)(TFA),[71] Zn(TFMA)(MA)(TFA) (Figure S6.8) and Zn(TFMA) (Figure 2). For direct comparison here the contrast curves were only compared for the samples developed by using diluted propionic acid in $CHCl_3$. Unexpectedly, the studies using contrast curves revealed that the overall EUVL performance of the new fluorine-rich Zn oxoclusters was not enhanced. It was observed that the sensitivity (dose for 50% thickness loss, D_{50}) and the contrast (γ)[204] of the fluorine-rich oxocluster, Zn(TFMA); D_{50} = 40 mJ/cm^2 and γ = 1.71 was decreased as compared to its analogue Zn(MA)(TFA); D_{50} = 3.3-10.8 mJ/cm^2 and γ = 2.95-0.95.

This decrease in the sensitivity could arise from various factors. The electron density on the terminal double bond of TFMA ligand is relatively low because of the neighbouring electron-withdrawing CF_3 group.[205] Previous studies have shown that introduction of a $-CF_3$ group at the α position decreases the rate of radical homopolymerization of the TFMA unit.[206,207] Different molecular packing of the oxoclusters in Zn(TFMA) compared to its analogue Zn(MA)(TFA)

or a reduced ratio of the solubility rates of the unexposed and exposed regions in the developer of choice can also contribute towards this observed decrease in the sensitivity. Therefore, incorporation of more fluorine in such systems does not always directly translate into better EUVL performance of the photoresist, in contrast to the previous reported studies.[114,208] Further, contrast curve studies demonstrated that post-exposure bake (PEB) applied at 120 °C/ 30 s led to a further slight decrease in the sensitivity (also see section 6.3.4). Spectroscopic studies to identify the chemical changes induced by PEB in the oxocluster were also done and discussed in section 6.3.7.

Table 6.1: Comparison of sensitivity (D_{50}) and contrast (γ) of the three Zn-based oxoclusters for EUV lithography performance; without and with PEB and developed using diluted propionic acid in $CHCl_3$; concentration of the propionic acid used is mentioned in their respective contrast curves figures.

without PEB	**Zn(MA)(TFA)**[71]	**Zn(TFMA)(MA)(TFA)**	**Zn(TFMA)**
D_{50}(mJ/cm^2)	3.3-10.8	40.6	40.0
Contrast (γ)	2.95-0.95	3.10	1.71
with PEB	**100 °C/ 30 s**	**120 °C/ 30 s**	**120 °C/ 30 s**
D_{50}(mJ/cm^2)	6.4	50.5	45.0
Contrast (γ)	0.92	3.01	1.65

6.3.3 EUV-IL performance of fluorine-rich Zn oxoclusters

EUV-IL experiments were performed on Zn(TFMA) and Zn(TFMA)(MA)(TFA) oxoclusters to print L/S patterns of HP 50 nm, 40 nm, 30 nm and 22 nm. Selected SEM images of L/S patterns printed in Zn(TFMA) using EUV-IL and developed using diluted propionic acid in $CHCl_3$ and with 2-heptanone are shown in Figure 6.3 and in SI, S6.13, respectively. Irregularities in the films can be seen along with the scumming (residual resist between lines) and bridging between the printed lines. The decrease in the sensitivity demonstrated via contrast curves experiments is also observed here. The L/S patterns printed with the fluorine-rich oxocluster are only observed at a relatively higher dose than required for its analogue Zn(MA)(TFA).[150]

Zn(TFMA)(MA)(TFA) oxocluster was studied with EUV-IL in the same way as Zn(TFMA). Figures S6.10-S6.12 show selected SEM and AFM images of L/S features of HP 50 nm, 40 nm, 30 nm, and 22 nm developed using both 2-heptanone and diluted propionic acid in $CHCl_3$. The SEM and AFM images show considerable scumming after development also in this case.

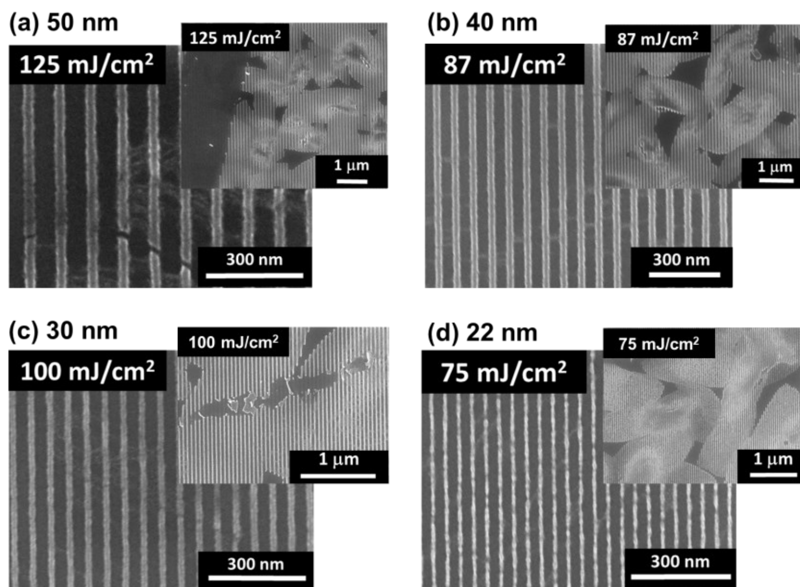

Figure 6.3: SEM images of line space patterns of half pitch: (a) 50 nm, (b) 40 nm, (c) 30 nm, and (d) 22 nm; printed using EUV-IL exposures on Zn(TFMA) oxocluster and developed using diluted propionic acid (0.1%) in 2-heptanone (10 s). The inset images show the irregularities of the thin film (zoom out).

6.3.4 Effect of PEB on EUV-IL performance

Application of post-exposure bake (PEB) did not show significant improvement in the EUV-IL performance for both Zn(TFMA)(MA)(TFA) and Zn(TFMA) oxocluster (120 °C/30 s). On the contrary, the application of PEB enhanced crystallization, bridging and scumming between L/S patterns. Figure S6.14 compares the performance of Zn(TFMA) oxocluster before and after PEB at the same dose of 75 mJ/cm^2.

Although the thin films show irregularities upon spin coating, the chemical changes induced by exposure to EUV irradiation can be studied using different spectroscopic techniques. Ex situ: STXM-NEXAFS, FTIR and UV-vis spectroscopy and in situ XPS studies were used to gain insights into the chemical changes in Zn oxoclusters as a function of the EUV dose. To monitor the chemical changes induced by EUV irradiation, the spectroscopic studies were focused on fluorine-rich Zn(TFMA) oxocluster.

6.3.5 STXM measurements

To gain insights into the chemical changes upon EUV exposure in fluorine-rich Zn(TFMA) oxocluster, ex situ X-ray absorption spectroscopy (XAS) studies were performed using STXM at the PolLux beamline at PSI.[198,209,210] The changes in the material as a function of EUV dose were observed especially in the near-edge region of the C K-edge spectra as it provides quantitative information on the types and amount of covalent bonding components. The spectra were measured in transmission mode and thus, the whole thin film thickness was probed. Chemical changes in the material upon applied doses of 25 mJ/cm^2, 50 mJ/cm^2 and 250 mJ/cm^2 were monitored. The remaining thickness after development and quality of the exposed area on the SiN_x membrane after development was inspected using AFM, shown in SI, Figure S6.15.

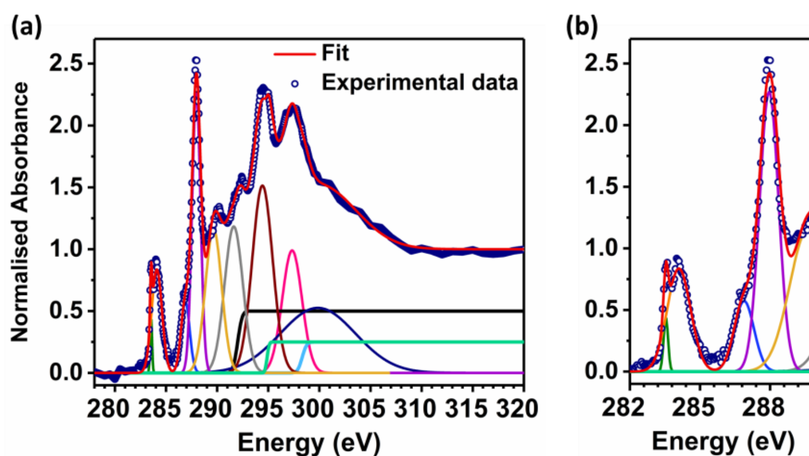

Figure 6.4: STXM-XAS C K-edge spectra of unexposed Zn(TFMA) thin film. (a) complete spectrum, and (b) zoom-in on the low energy features .

All the spectra were normalised to the continuum above ~310 eV. The interpretation of the spectra was based on the "building-block model" and hence molecular oxocluster was considered as being composed of the individual local units.[211–213] In the fitting procedure, the step function representing the ionization to the continuum[214,215] was represented by three steps corresponding to the C-C/C-H (292.0 eV), -COO (294.9 eV) and –C-F (298.3 eV) units of the Zn-oxocluster, which have characteristically different binding energies, as discussed below.

The fitted spectra of the reference (unexposed) sample of Zn(TFMA), shown in Figure 6.4, presents clear, sharp peaks at 284.2 eV and 284.7 eV. Quantum chemical calculations indicate that these correspond to the electronic transitions

from C 1*s* orbitals on C1 and C2 to the lowest unoccupied MO, which is a π* orbital delocalized over the C=C-C=O unit, C 1s→ $\pi^*_{C=C-C=O}$ (Figure S6.18). The strong absorption at 287.9 eV and the shoulder at 286.8 eV are mainly due to transitions from C 1*s* of C1, C2 and C3 to the next higher π* MO (Figure S6.18). The peaks at higher energies are not assigned here; they represent a complex mix of transitions involving σ* and Rydberg orbitals.[216–219]

Upon conversion due to EUV irradiation, the peaks at 284.2 and 284.7 eV decrease in intensity relative to the main peak at 286.8/287.9 eV. This is consistent with the disappearance of the C=C bonds due to cross-linking reactions. In the reaction product, the C=O bond remains, and the LUMO becomes the localized $\pi^*_{C=O}$, which has nearly the same energy as the LUMO+1 orbital in the intact TFMA ligand. The ratio $A_{C=C}/A_{C=O}$ (where A is the area under the peaks after fitting) decreased as a function of EUV dose as shown in Figure 6.5. Radical polymerization of the C=C is one of the major channels leading to a significant decrease in the component as a function of dose after decarboxylation reaction. The C K-edge fitted spectra measured for the exposed area on Zn(TFMA) thin film are shown in Figure S6.16. No significant changes were observed in the shape of the recorded F K-edge spectra as a function of EUV dose (Figure S6.17).

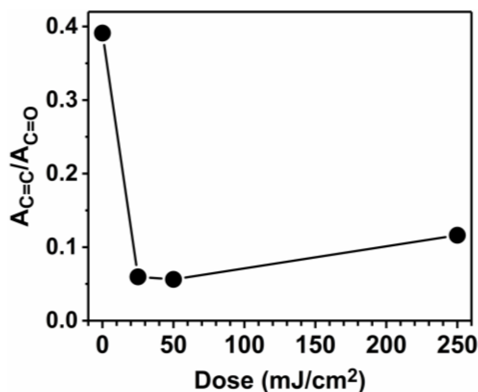

Figure 6.5: $A_{C=C}$/ $A_{C=O}$ as function of EUV dose for the area under the peaks, C=C units (284.2 and 284.7 eV), C=O units (286.8 and 287.9 eV) in C 1*s* K-edge NEXAFS.

6.3.6 UV-vis spectroscopy

The chemical changes in the material upon EUV irradiation, especially in the C=C double bond of the ligand can be effectively tracked using UV-vis spectroscopy. A decrease in the absorption band at ~190 nm (π to π* transition)[150] was observed as a function of EUV dose, shown in Figure 6.6(a). This bleach can be mainly attributed to the polymerization, in agreement with the STXM results. In

addition, a simultaneous increase in absorbance around ~275 nm was observed which can be due to the scattering of light or absorption by the network of oxoclusters/aggregates formed after EUV exposure (Figure 6.10(a)).[220] Figure 6.6(b) represents the decrease in A/A_0 at ~190 nm as a function of EUV dose. Considering that the absorbance reaches a steady value $A/A_0 \approx 0.55$ at high conversion, we can estimate that roughly 69% of the C=C double bonds are converted at the D_{50} dose (Table 6.1).

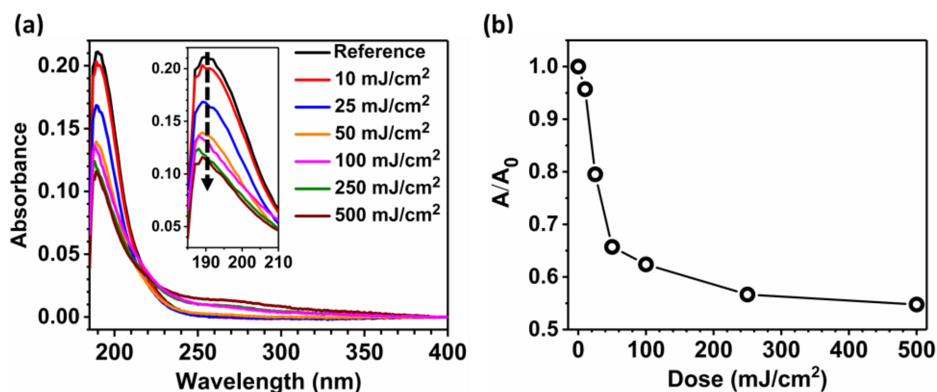

Figure 6.6: UV-vis spectroscopy on Zn(TFMA) thin film (a) as a function of EUV dose without application of PEB and no development, and (b) A/A_0 at ~190 nm as a function of dose.

6.3.7 Infrared spectroscopy

Chemical changes in the organic part of the oxocluster (ligands) upon EUV exposure were further tracked using FTIR. Figure S6.3 shows the FTIR of Zn(TFMA) oxocluster in powder form and in thin film. Loss of two peaks, (marked by asterisks) assigned to ν_{as} COO (TFMA) monodentate (1678 cm^{-1}) and ν C=C (TFMA) monodentate (1631 cm^{-1}) occurs upon thin film formation.[71]

Figure 6.7(a) represents the evolution of FTIR peaks of Zn(TFMA) thin films as a function of EUV dose. A decrease in the absorbance ratio A/A_0 (A_0 is the area under the peak of unexposed thin film) of ν C=C (1660 cm^{-1}, Figure 6.7(b)) was observed in agreement with NEXAFS and UV-vis spectroscopy. The conversion at D_{50} is approximately half of the maximum conversion achieved at high dose. Simultaneously, a decrease in the A/A_0 of -COO (TFMA, 1678 cm^{-1}) was observed with increasing dose due to decarboxylation and outgassing of CO_2 upon EUV exposure. A/A_0 of C-F (1130 and 1167 cm^{-1}) also decreased and as shown in our previous studies. This is likely due to the formation of F^- species formed via dissociative electron attachment (DEA). More details about C-F bond cleavage in

the organic shell of the oxocluster can be found in the XPS section below. The negative peak at 1100 cm^{-1} is assigned to Si-O bond stretching and is probably the result of a slightly thicker SiO_2 layer on the surface of Si substrate in the reference than in the sample.

In addition, the effect of post-exposure bake (PEB) (120 °C/ 30 s) on chemical changes was studied using ex situ UV-vis spectroscopy (Figure S6.19) and FTIR (Figure S6.20). The effect of PEB depends on the post-exposure chemistry. In non-chemically amplified photoresists PEB sometimes, but not always, results in the improvement of lithography performance.[133,221,222] Contrast curve studies presented above revealed a slight decrease in the sensitivity (D_{50}) of Zn(TFMA)(MA)(TFA) and Zn(TFMA) oxoclusters, but this is probably within the margins of error. The UV-vis and FTIR results showed no significant extra decrease in the absorption intensity of -C=C- upon PEB application. The lack of a strong effect of PEB in the present case is consistent with the proposed mechanisms, in which reactive intermediates that would survive ambient conditions do not play a role.

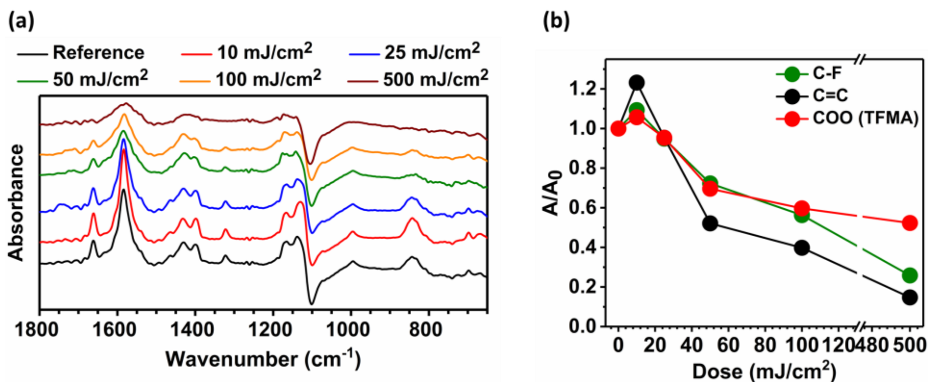

Figure 6.7: FTIR spectra of Zn(TFMA) thin film (a) as a function of EUV dose (no PEB, no development), and (b) A/A_0 as a function of dose for peaks in the spectra shown in (a); C-F (1130-1167 cm^{-1}), C=C (1631 cm^{-1}) and COO TFMA (1678 cm^{-1}).

6.3.8 Post-EUV exposure in situ XPS

To investigate the chemical changes induced by EUV irradiation of Zn(TFMA) in more depth, we combined ex situ spectroscopy studies with in situ XPS spectroscopy. In situ spectroscopy allows avoiding the chemical changes in the material due to the reaction between the sample and the ambient air, and carbon contamination of the surface. XPS spectra were recorded for C (1*s*), O (1*s*) and F (1*s*) as a function of EUV dose in a range of 5 mJ/cm^2 to 500 mJ/cm^2. A film

thickness of 15 nm was measured using AFM on a reference sample spin coated on a Si substrate using the same conditions and same solution. Selected XPS spectra of the C(1*s*) and F(1*s*) ranges are shown in Figure 6.8. The C-F peak at 292.81 eV for C(1*s*) and 688.21 eV for F(1s) were used as internal references to calibrate the binding energy scale of each spectrum.[150] The C (1*s*) spectra can be fitted with four components assigned to sp^2 carbon (285.58 ± 0.25 eV), sp^3 carbon (286.41 ± 0.21 eV)[223], COO(289.38 ± 0.22 eV) and C-F (292.81 ± 0.25 eV).[150] The fitted F(1s) spectra have 2 components assigned to C-F (688.21 ± 0.19 eV) and Zn-F (685.08 ± 0.24 eV).[150]

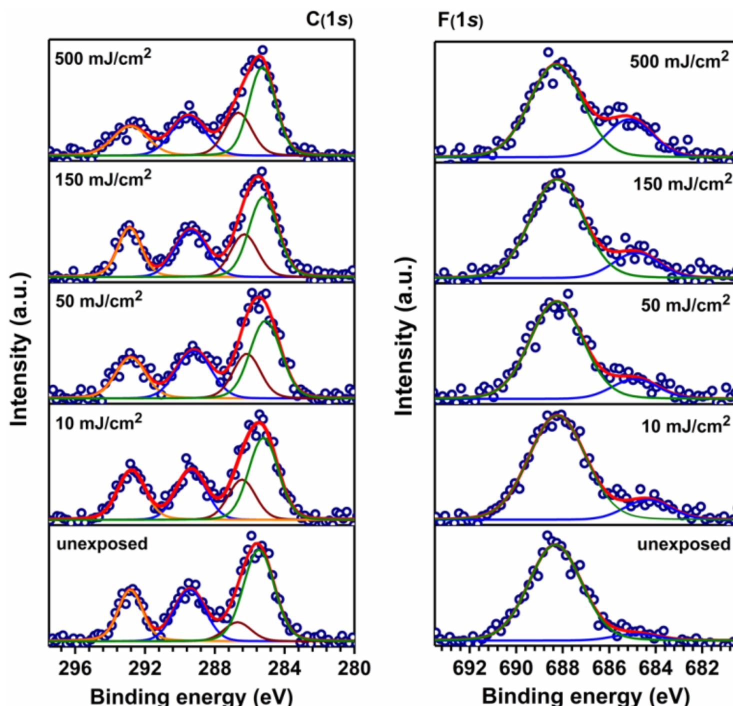

Figure 6.8: Selected C(1s) and F(1s) XPS spectra recorded as a function of EUV doses with photon energies of 400 eV and 800 eV, respectively. Fresh spots on the thin films were used for each EUV exposure (~92 eV) followed by the XPS measurements.

The fitted sp^2 carbon component is observed to decrease while the sp^3 component increases as a function of increasing EUV dose, in agreement with polymerization of the C=C double bonds of TFMA. The fractional area of the components assigned to -COO and C-F in C (1*s*) spectra is observed to decrease as well, as a function of EUV dose, signifying loss of –COO (outgassing as CO_2) and C-F from the organic shell of the ligand, as shown in Figure 6.9(a).

The F (1*s*) XPS spectra also reveal a decrease of the C-F component (Figure 6.9(b)) and a new species assigned to a metal fluoride (Zn-F in this case) was observed. The fractional area of the Zn-F species is observed to increase as a function of EUV dose, as also observed in our previous studies.[150] The decrease in the C-F and simultaneous increase in the Zn-F is attributed to the migration of fluorine from the organic shell to the Zn-core, shown in Figure 6.10(c).

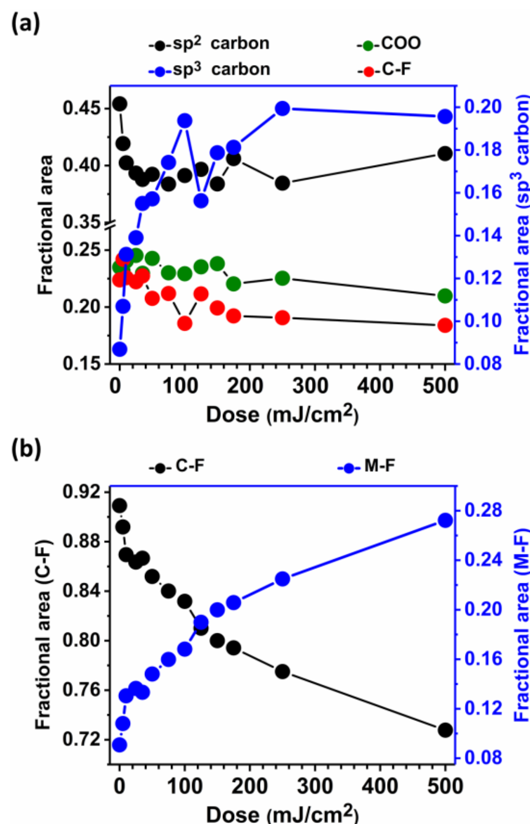

Figure 6.9: Fractional area of the fitted components as the function of EUV dose in XPS spectra of: (a) C(1*s*); sp^2 carbon, -COO and C-F (left axis) and sp^3 carbon (right axis), (b) F(1*s*); two components for C-F and M-F.

In addition, the STXM studies also demonstrated no or very little loss of fluorine from the thin film after EUV exposure. The cleavage of the C-F bond is induced in the ligand via a well-known path: dissociative ion attachment (DEA)[146,197] which is a common reaction pathway upon interaction with low energy electrons. The XPS spectra recorded for O(1*s*) were fitted with only one component (-COO)

at a binding energy of 532.13 ± 0.17 eV. As an example, the fitted spectra for unexposed thin film are shown in SI, Figure S6.21(a) and the decrease in A/A_0 for the fitted –COO component in O(1*s*) recorded spectra as a function of EUV dose also points towards decarboxylation, shown in SI, Figure S6.21(b).

6.3.9 Reaction mechanism

To summarize the results from all spectroscopy analysis and discussions above, the possible reaction pathways are proposed in Figure 6.10. The ionization event of the Zn(TFMA) oxocluster after EUV photon absorption (Figure 6.10(a)) will likely be followed by decarboxylation, consequently leaving active sites on the Zn-core of the oxocluster and formation of reactive radical species in the thin film. These radical species formed in step (a) can further initiate radical polymerization events in the thin film (cross-linking of the terminal double bond of TFMA) with the neighbouring Zn oxocluster (Figure 6.10(b)). Moreover, the low energy secondary electrons generated in the thin films after the ionization process (a) can induce bond cleavage of C-F via well-known DEA process[146] and parallel generation of radical species in thin films. The XPS studies (section 6.3.8) clearly indicate the formation of new Zn-F species after EUV exposure, shown in Figure 6.10(c).

The main contributor to the solubility switch is the cross-linking between ligands of neighbouring clusters. The proposed radical mechanism allows propagation to form extended chains, in competition with termination reactions. Since reactive radicals do not survive long under ambient conditions, the chemical reactions will be finished shortly after exposure, consistent with the lack of a PEB effect.

The different spectroscopic methods applied in the present work agree semi-quantitatively on the extent of conversion that is necessary to reach the solubility switch, which is the key property of a photoresist. Differences arise because different measurements were carried out on different samples and under different experimental conditions. Although the spin-coated films were shown to be fairly stable, some aging could not always be avoided, before and after exposure. Despite these quantitative limitations, it is evident that reaching the point of solubility switch, e.g. defined as the D_{50} value (Table 6.1) which is near 40 mJ/cm^2, requires a considerable conversion of the acrylate double bonds, of the order of 50%.

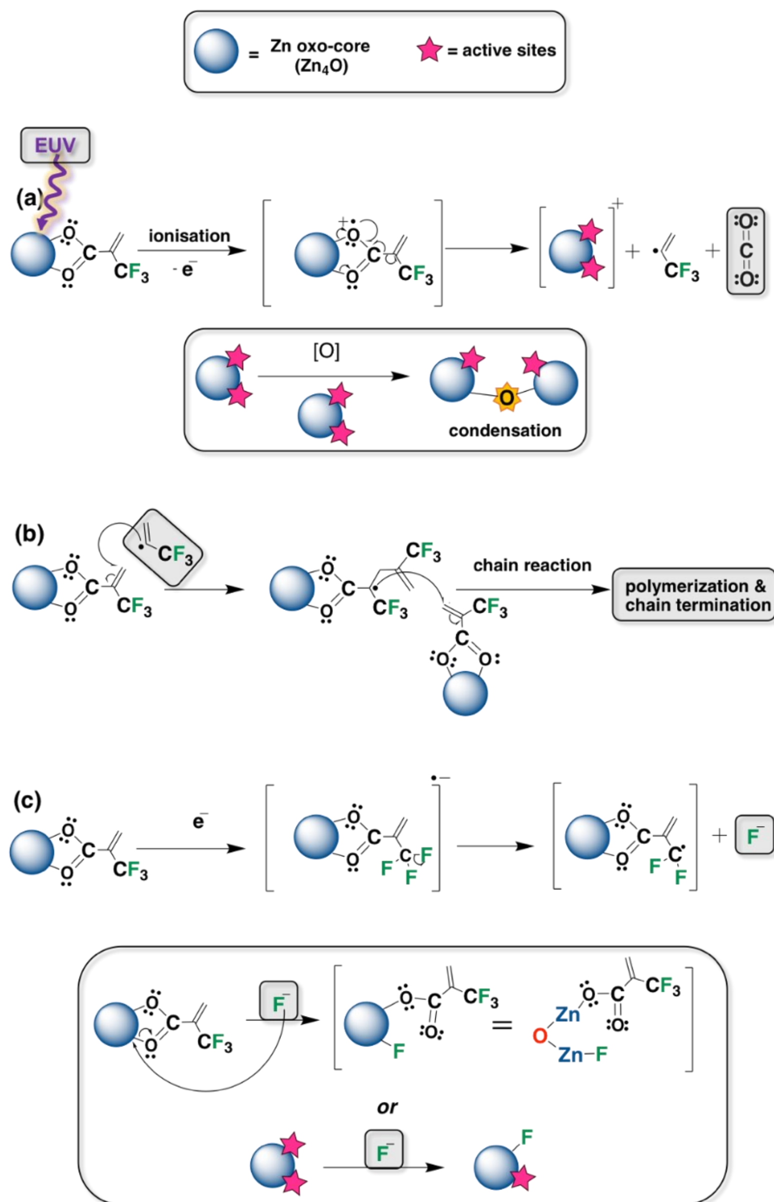

Figure 6.10: Proposed reaction mechanisms for Zn(TFMA) oxocluster upon EUV irradiation: (a) ionization of oxocluster followed by decarboxylation reaction, generation of radical and active sites on oxo-core in the thin film; condensation reaction between two clusters, (b) radical initiated polymerization of the terminal double bond of TFMA ligand in the thin films, and (c) C-F bond cleavage via DEA pathway; formation of Zn-F species.

The proposed mechanism allows for multiple reactions per absorbed photon, in other words a quantum yield of reaction exceeding 1: multiple low energy electrons are expected to be generated per photon, each charge separation event can give rise to two reactive species, and the cross-linking reactions proceeds through a radical chain mechanism. A high quantum yield, however, is not guaranteed, because holes and electrons may recombine, and the chain propagation may be interrupted by termination reactions. A challenge for future research is to quantify the processes in more detail. In particular, it is important to know how long chains are formed in the cross-coupling, what the termination steps are, and how the length of the chains is related to solubility change. Here, we can make an estimate of the average reaction quantum yield for conversion of the C=C bonds. Based on the linear EUV absorption cross section (α) of 14.3 μm^{-1} for Zn(TFMA), and considering the thickness of the exposed thin film (d) of ~20 nm, the EUV transmittance, T = $e^{-\alpha d}$ through the resist is ~75%. Consequently ~25% of the photons are absorbed. At the D_{50} value of 40 mJ/cm^2 dose at least ~50% of the acrylate double bonds has been converted, based on UV, IR and XPS measurements. Using the estimated density of ~2 g/cm^3 we find that the ratio of the number of C=C converted to the number of photons absorbed is ~10 : 1, which suggests an average quantum yield of ~10, in agreement with the mechanism.

6.4 Conclusions

In the present study, we have investigated fluorine-rich Zn oxoclusters for EUV lithography applications. The results have provided us with the following insights:

Stability and EUV lithography performance: Thin film stability of the fluorine-rich Zn(TFMA) oxocluster was increased compared to its previously studied analogue Zn(MA)(TFA), while the sensitivity (D_{50}) for EUV lithography was decreased. The increased stability of Zn(TFMA) oxocluster can be mainly attributed to the hydrophobic nature of the fluorine. The decreased EUV sensitivity of fluorine-rich oxoclusters may arise from several factors: high electronegativity of fluorine slowing down the radical homopolymerization reaction rate; different molecular packing of the oxocluster in the thin-film; and different developer-resist interactions. This study shows that although the incorporation of more fluorine in such systems increases the EUV absorbance, this does not directly translate into higher EUVL sensitivity of the photoresist.

Chemical changes after EUV exposure: A combination of detailed spectroscopic studies shows decarboxylation of the carboxylate ligand upon EUV absorption in the Zn(TFMA) oxocluster. In addition, a strong decrease of the C=C/C=O area in STXM-NEXFAS studies as a function of EUV dose supports radical initiated

polymerization in the thin film, which is also supported by UV-vis, FTIR and in situ XPS studies. Furthermore, in situ XPS studies shows the formation of new zinc fluoride species in the material upon EUV irradiation via dissociative electron attachment pathway.

We believe that the present results enhance our understanding of Zn-based fluorine-rich photoresists and similar systems for lithography application and will propel advance focused investigations for fluorine-rich photoresist materials.

REFERENCES

[1] "IBM Unveils World's First 2 Nanometer Chip Technology, Opening a New Frontier for Semiconductors," can be found under https://newsroom.ibm.com/2021-05-06-IBM-Unveils-Worlds-First-2-Nanometer-Chip-Technology,-Opening-a-New-Frontier-for-Semiconductors, **2021**.

[2] "Noyce receives 1st IC patent, April 25, 1961 - EDN," can be found under https://www.edn.com/noyce-receives-1st-ic-patent-april-25-1961/, **2019**.

[3] "Semiconductor Room : Hitachi High-Tech GLOBAL," can be found under https://www.hitachi-hightech.com/global/products/device/semiconductor/, **2001**.

[4] J. Bardeen, W. H. Brattain, *Phys. Rev.* **1948**, *74*, 230.

[5] D. Lindley, *Phys. Rev. Focus* **2009**, *23*, 16.

[6] G. E. Moore, *IEEE Solid-State Circuits Soc. Newsl.* **2009**, *11*, 33.

[7] G. E. Moore, *IEDM Tech. Dig.* **1975**, *21*, 11.

[8] "Over 50 Years of Moore's Law," can be found under https://www.intel.com/content/www/us/en/silicon-innovations/moores-law-technology.html**.**

[9] H. J. Levinson, *Principles of Lithography Third Edition*, SPIE, **2011**.

[10] C. Mack, *Fundamental Principles of Optical Lithography: The Science of Microfabrication*, John Wiley & Sons, **2008**.

[11] R. Hirose, T. Kozawa, S. Tagawa, T. Kai, T. Shimokawa, *Jpn. J. Appl. Phys.* **2007**, *46*, L979.

[12] J. Nakamura, H. Ban, A. Tanaka, *Jpn. J. Appl. Phys.* **1992**, *31*, 4294.

[13] Rayleigh, *London, Edinburgh, Dublin Philos. Mag. J. Sci.* **1879**, *8*, 261.

[14] B. J. Lin, *Microelectron. Eng.* **2015**, *143*, 91.

[15] T. Ito, S. Okazaki, *Nature* **2000**, *406*, 1027.

[16] C. Wagner, N. Harned, *Nat. Photonics* **2010**, *4*, 24.

[17] S. Park, I. Lee, S. Koo, J. Lee, C.-M. Lim, *Proc. SPIE* **2016**, *9776*, 97761Q.

[18] J. Miyazaki, A. Yen, *J. Photopolym. Sci. Technol.* **2019**, *32*, 195.

[19] W. Yayi, B. David, *SPIE* **2007**, DOI 10.1117/2.1200703.0001.

[20] B. W. Smith, Y. Fan, M. Slocum, L. Zavyalova, *Proc. SPIE* **2005**, *5754*, 141.

[21] T. Haga, *J. Photopolym. Sci. Technol.* **2018**, *31*, 193.

[22] "The International Roadmap for Devices and Systems 2017," can be found under https://irds.ieee.org, **2018**.

[23] G. M. Gallatin, A. K. Narasimhan, R. L. Brainard, M. Neisser, in *EUV Lithogr.* (Ed.: V. Bakshi), SPIE, **2018**, pp. 493–592.

[24] L. Mark, "EUV's Uncertain Future At 3nm And Below," can be found under https://semiengineering.com/whats-next-for-euv/, **2020**.

[25] A. Reiser, H. Y. Shih, T. F. Yeh, J. P. Huang, *Angew. Chemie* **1996**, *35*, 2428.

[26] C. Luo, C. Xu, L. Lv, H. Li, X. Huang, W. Liu, *RSC Adv.* **2020**, *10*, 8385.

[27] "Patterning the World: The Rise of Chemically Amplified Photoresists | Science History Institute," can be found under https://www.sciencehistory.org/distillations/patterning-the-world-the-rise-of-chemically-amplified-photoresists, **2007**.

[28] N. H. Jakatdar, X. Niu, C. J. Spanos, A. R. Romano, J. J. Bendik, R. P. Kovacs, S. L. Hill, *Proc. SPIE* **1998**, *3332*, 586.

[29] H. Ito, C. G. Wilson, J. H. J. Frechet, *1982 Symp. VLSI Technol. Dig. Tech. Pap. IEEE* **1982**, 86.

[30] Q. Wang, C. Zhang, C. Yan, F. You, L. Wang, *Eur. Polym. J.* **2019**, *114*, 11.

[31] D. P. Sanders, *Chem. Rev.* **2010**, *110*, 321.

[32] T. Nagai, H. Nakagawa, T. Naruoka, S. Dei, S. Tagawa, A. Oshima, S. Nagahara, G. Shiraishi, K. Yoshihara, Y. Terashita, Y. Minekawa, E. Buitrago, Y. Ekinci, O. Yildirim, M. Meeuwissen, R. Hoefnagels, G. Rispens, C. Verspaget, R. Maas, *J. Photopolym. Sci. Technol.* **2016**, *29*, 475.

[33] A. Nakano, T. Kozawa, K. Okamoto, S. Tagawa, T. Kai, T. Shimokawa, *Jpn. J. Appl. Phys.* **2006**, *45*, 6866.

[34] S.-J. Kim, G.-J. Yu, J.-Y. Lee, H.-J. Kim, J.-W. Lee, D.-B. Kim, Y. Kang, J. Kim, *Proc. SPIE* **2007**, *6519*, 651947.

[35] T. Fujii, S. Matsumaru, T. Yamada, Y. Komuro, D. Kawana, K. Ohmori, *Proc. SPIE* **2016**, *9776*, 97760Y.

[36] M. Hori, T. Naruoka, H. Nakagawa, T. Fujisawa, T. Kimoto, M. Shiratani, T. Nagai, R. Ayothi, Y. Hishiro, K. Hoshiko, T. Kimura, *Proc. SPIE* **2015**, *9422*, 94220P.

[37] A. Narasimhan, S. Grzeskowiak, C. Ackerman, T. Flynn, G. Denbeaux, R. L. Brainard, *Proc. SPIE* **2017**, *10143*, 101430W.

[38] T. Kozawa, S. Tagawa, *Jpn. J. Appl. Phys.* **2010**, *49*, 030001.

[39] I. Bespalov, Y. Zhang, J. Haitjema, R. M. Tromp, S. J. Van Der Molen, A. M. Brouwer, J. Jobst, S. Castellanos, *ACS Appl. Mater. Interfaces* **2020**, *12*, 9881.

[40] W. F. van Dorp, in *Front. Nanosci.*, Elsevier, **2016**, pp. 115–133.

[41] J. Torok, R. Del Re, H. Herbol, S. Das, I. Bocharova, A. Paolucci, L. E. Ocola, C. Ventrice Jr., E. Lifshin, G. Denbeaux, R. L. Brainard, *J. Photopolym. Sci. Technol.* **2013**, *26*, 625.

[42] D. F. Ogletree, in *Front. Nanosci.*, Elsevier, **2016**, pp. 91–113.

[43] R. A. Lawson, A. P. G. Robinson, in *Front. Nanosci.*, Elsevier, **2016**, pp. 1–90.

[44] R. L. Brainard, G. G. Barclay, E. H. Anderson, L. E. Ocola, *Microelectron. Eng.* **2002**, *61–62*, 707.

[45] T. Kozawa, S. Tagawa, *Jpn. J. Appl. Phys.* **2008**, *47*, 8354.

[46] K. Yoshimoto, C. Higgins, A. Raghunathan, J. G. Hartley, D. L. Goldfarb, H. Kato, K. Petrillo, M. E. Colburn, J. Schefske, O. Wood, T. I. Wallow, *Proc. SPIE* **2011**, *7972*, 79720K.

[47] R. Gronheid, C. Fonseca, M. J. Leeson, J. R. Adams, J. R. Strahan, C. G. Willson, B. W. Smith, *Proc. SPIE* **2009**, *7273*, 727332.

[48] R. Fallica, J. Haitjema, L. Wu, S. C. Ortega, A. M. Brouwer, Y. Ekinci, *J. Micro/Nanolithography, MEMS, MOEMS* **2018**, *17*, 023505.

[49] M. D. Christianson, M. M. Meyer, O. Ongayi, D. Valeri, M. Wagner, *Proc. SPIE* **2013**, *8682*, 868216.

[50] T. Sasaki, O. Yokokoji, T. Watanabe, H. Kinoshita, *Proc. SPIE* **2008**, *6923*, 692347.

[51] J. W. Thackeray, *J. Micro/Nanolithography, MEMS, MOEMS* **2011**, *10*, 033009.

[52] M. Neisser, K. Cho, K. Petrillo, *J. Photopolym. Sci. Technol.* **2012**, *25*, 87.

[53] T. Fujimori, T. Tsuchihashi, S. Minegishi, T. Kamizono, T. Itani, *Proc. SPIE* **2016**, *9776*, 977605.

[54] M. Trikeriotis, M. Krysak, Y. S. Chung, C. Ouyang, B. Cardineau, R. Brainard, C. K. Ober, E. P. Giannelis, K. Cho, *Proc. SPIE* **2012**, *8322*, 83220U.

[55] B. Cardineau, R. Del Re, H. Al-Mashat, M. Marnell, M. Vockenhuber, Y. Ekinci, C.

Sarma, M. Neisser, D. A. Freedman, R. L. Brainard, *Proc. SPIE* **2014**, *9051*, 90511B.

[56] Y. Zhang, J. Haitjema, X. Liu, F. Johansson, A. Lindblad, S. Castellanos, N. Ottosson, A. M. Brouwer, *J. Micro/Nanolithography, MEMS, MOEMS* **2017**, *16*, 023510.

[57] B. Cardineau, in *Front. Nanosci.*, Elsevier, **2016**, pp. 377–420.

[58] M. Wilklow-Marnell, D. Moglia, B. Steimle, *J. Micro/Nanolithography, MEMS, MOEMS* **2018**, *17*, 1.

[59] M. Sortland, R. Del Re, J. Passarelli, J. Hotalen, M. Vockenhuber, Y. Ekinci, M. Neisser, D. Freedman, R. L. Brainard, *Proc. SPIE* **2015**, *9422*, 942227.

[60] J. Sitterly, M. Murphy, S. Grzeskowiak, G. Denbeaux, R. L. Brainard, *Proc. SPIE* **2018**, *10586*, 105861P.

[61] X. Wang, Z. Tasdemir, I. Mochi, M. Vockenhuber, L. van Lent-Protasova, M. Meeuwissen, R. Custers, G. Rispens, R. Hoefnagels, Y. Ekinci, *Proc. SPIE* **2019**, *10957*, 109570A.

[62] L. Li, X. Liu, S. Pal, S. Wang, C. K. Ober, E. P. Giannelis, *Chem. Soc. Rev.* **2017**, *46*, 4855.

[63] L. Wu, M. Vockenhuber, Y. Ekinci, S. Castellanos, *Proc. SPIE* **2019**, *10957*, 109570B.

[64] J. Kreutzer, M. Puchberger, C. Artner, U. Schubert, *Eur. J. Inorg. Chem.* **2015**, *2015*, 2145.

[65] L. Wu, M. Baljozovic, G. Portale, D. Kazazis, M. Vockenhuber, T. Jung, Y. Ekinci, S. Castellanos, *J. Micro/Nanolithography, MEMS, MOEMS* **2019**, *18*, 013504.

[66] L. Wu, M. Tiekink, A. Giuliani, L. Nahon, S. Castellanos, *J. Mater. Chem. C* **2019**, *7*, 33.

[67] B. L. Henke, E. M. Gullikson, J. C. Davis, *At. Data Nucl. Data Tables* **1993**, *54*, 181.

[68] H. Xu, K. Sakai, K. Kasahara, V. Kosma, K. Yang, H. C. Herbol, J. Odent, P. Clancy, E. P. Giannelis, C. K. Ober, *Chem. Mater.* **2018**, *30*, 4124.

[69] V. Kosma, K. Kasahara, H. Xu, K. Sakai, C. Ober, E. Giannelis, *Proc. SPIE* **2018**, *10583*, 105831U.

[70] H. Xu, V. Kosma, K. Sakai, E. P. Giannelis, C. K. Ober, *J. Micro/Nanolithography, MEMS, MOEMS* **2018**, *18*, 011007.

[71] N. Thakur, L.-T. Tseng, M. Vockenhuber, Y. Ekinci, S. Castellanos, *J. Micro/Nanolithography, MEMS, MOEMS* **2019**, *18*, 043504.

[72] B. J. Lin, *Microelectron. Eng.* **2006**, *83*, 604.

[73] B. J. Lin, *J. Micro/Nanolithography, MEMS, MOEMS* **2008**, *7*, 40101.

[74] P. P. Naulleau, C. N. Anderson, L.-M. Baclea-An, P. Denham, S. George, K. A.

Goldberg, G. Jones, B. McClinton, R. Miyakawa, S. Rekawa, *Proc. SPIE* **2011**, *7972*, 797202.

[75] Y. Ekinci, M. Vockenhuber, N. Mojarad, D. Fan, *Proc. SPIE* **2014**, *9048*, 904804.

[76] A. Lio, *Proc. SPIE* **2016**, *9776*, 97760V.

[77] P. Naulleau, in *Front. Nanosci. – Mater. Process. Next Gener. Lithogr.*, Elsevier Ltd, **2016**, pp. 177–192.

[78] D. De Simone, P. Vanelderen, G. Vandenberghe, *J. Photopolym. Sci. Technol.* **2017**, *30*, 613.

[79] D. De Simone, V. Rutigliani, G. Lorusso, P. De Bisschop, Y. Vesters, V. B. Carballo, G. Vandenberghe, *Proc.SPIE* **2018**, *10583*, 105830G.

[80] R. Maas, M.-C. van Lare, G. Rispens, S. F. Wuister, *J. Micro/Nanolithography, MEMS, MOEMS* **2018**, *17*, 041003.

[81] N. Mark, K. Cho, K. Petrillo, *J. Photopolym. Sci. Technol.* **2012**, *25*, 87.

[82] S. W. Chang, D. Yang, J. Dai, N. Felix, D. Bratton, K. Tsuchiya, Y.-J. Kwark, J.-P. Bravo-Vasquez, C. K. Ober, H. B. Cao, *Proc. SPIE* **2005**, *5753*, 1.

[83] O. Yildirim, E. Buitrago, R. Hoefnagels, M. Meeuwissen, S. Wuister, G. Rispens, A. van Oosten, P. Derks, J. Finders, M. Vockenhuber, Y. Ekinci, *Proc. SPIE* **2017**, *10143*, 101430Q.

[84] M. Krysak, M. Leeson, E. Han, J. Blackwell, S. Harlson, *Proc. SPIE* **2015**, *9422*, 942205.

[85] H. Xu, K. Yang, K. Sakai, V. Kosma, K. Kasahara, E. P. Giannelis, C. K. Ober, *Proc. SPIE* **2018**, *10583*, 105831P.

[86] P. D. Ashby, D. L. Olynick, D. F. Ogletree, P. P. Naulleau, *Adv. Mater.* **2015**, *27*, 5813.

[87] C. Ober, J. Jiang, B. Zhang, L. Li, E. Giannelis, J. S. Chun, M. Neisser, R. Sierra-Alvares, *Proc. SPIE* **2015**, *9422*, 942207.

[88] W. D. Hinsberg, S. Meyers, *Proc. SPIE* **2017**, *10146*, 1014604.

[89] K. D. Closser, D. F. Ogletree, P. Naulleau, D. Prendergast, *J. Chem. Phys.* **2017**, *146*, 164106.

[90] E. C. Mattson, Y. Cabrera, S. M. Rupich, Y. Wang, K. A. Oyekan, T. J. Mustard, M. D. Halls, H. A. Bechtel, M. C. Martin, Y. J. Chabal, *Chem. Mater.* **2018**, *30*, 6192.

[91] R. Gronheid, H. H. Solak, Y. Ekinci, A. Jouve, F. Van Roey, *Microelectron. Eng*. **2006**, *83*, 1103.

[92] R. Fallica, J. K. Stowers, A. Grenville, A. Frommhold, A. P. G. Robinson, Y. Ekinci, *J. Micro/Nanolithography, MEMS, MOEMS* **2016**, *15*, 33506.

[93] Y. Hayashi, T. Ohshima, Y. Fujii, Y. Matsushima, K. Mashima, *Catal. Sci. Technol.* **2011**, *1*, 230.

[94] T. Ohshima, *Chem. Pharm. Bull.* **2016**, *64*, 523.

[95] G. Kickelbick, P. Wiede, U. Schubert, *Inorganica Chim. Acta* **1999**, *284*, 1.

[96] S. Gross, G. Kickelbick, M. Puchberger, U. Schubert, *Monatshefte für Chemie* **2003**, *134*, 1053.

[97] D. Prochowicz, K. Sokołowski, J. Lewiński, *Coord. Chem. Rev.* **2014**, *270*, 112.

[98] S. B. Ötvös, O. Berkesi, T. Körtvélyesi, I. Pálinkó, *Inorg. Chem.* **2010**, *49*, 4620.

[99] E. C. Mattson, S. M. Rupich, Y. Cabrera, Y. J. Chabal, *Proc. SPIE* **2018**, *10583*, 1058309.

[100] R. Chen, Y. Li, L. Tang, H. Yang, Z. Lu, J. Wang, L. Liu, K. Takahashi, *RSC Adv.* **2017**, *7*, 40020.

[101] H. Koyama, Y. Saito, *Bull. Chem. Soc. Jpn.* **1954**, *27*, 112.

[102] C. A. Mack, *IEEE Trans. Semicond. Manuf.* **2011**, *24*, 202.

[103] R. M. M. Hasan, X. Luo, *Nanomanufacturing Metrol.* **2018**, *1*, 67.

[104] M. Neisser, *J. Microelectron. Manuf.* **2018**, *1*, 1.

[105] A. Lio, *Synchrotron Radiat. News* **2019**, *32*, 9.

[106] O. Kostko, B. Xu, M. Ahmed, D. S. Slaughter, D. Frank Ogletree, K. D. Closser, D. G. Prendergast, P. Naulleau, D. L. Olynick, P. D. Ashby, Y. Liu, W. D. Hinsberg, G. M. Wallraff, *J. Chem. Phys.* **2018**, *149*, 154305.

[107] A. Narasimhan, S. Grzeskowiak, B. Srivats, H. C. Herbol, L. Wisehart, C. Kelly, W. Earley, L. E. Ocola, M. Neisser, G. Denbeaux, *Proc. SPIE* **2015**, *9422*, 942208.

[108] A. Narasimhan, L. Wisehart, S. Grzeskowiak, L. E. Ocola, G. Denbeaux, R. L. Brainard, *J. Photopolym. Sci. Technol.* **2017**, *30*, 113.

[109] V. Bakshi, Ed. , *EUV Lithography*, Washington USA, **2008**.

[110] M. Trikeriotis, M. Krysaki, Y. S. Chung, C. Ouyang, B. Cardineau, R. Brainard, C. K. Ober, E. P. Giannelis, K. Cho, *J. Photopolym. Sci. Technol.* **2012**, *25*, 583.

[111] M. E. Krysak, J. M. Blackwell, S. E. Putna, M. J. Leeson, T. R. Younkin, S. Harlson, K. Frasure, F. Gstrein, *Proc. SPIE* **2014**, *9048*, 904805.

[112] R. Del Re, J. Passarelli, M. Sortland, B. Cardineau, Y. Ekinci, E. Buitrago, M. Neisser, D. A. Freedman, R. L. Brainard, *J. Micro/Nanolithography, MEMS, MOEMS* **2015**, *14*, 043506.

[113] L. Wu, J. Liu, M. Vockenhuber, Y. Ekinci, S. Castellanos, *Eur. J. Inorg. Chem.* **2019**, *2019*, 4136.

[114] L. Wu, M. Vockenhuber, Y. Ekinci, S. Castellanos, *Proc. SPIE* **2019**, *10957*, 109570B.

[115] E. C. Mattson, Y. Cabrera, S. M. Rupich, Y. Wang, K. A. Oyekan, T. J. Mustard, M. D. Halls, H. A. Bechtel, M. C. Martin, Y. J. Chabal, *Chem. Mater.* **2018**, *30*, 6192.

[116] A. De Silva, N. M. Felix, C. K. Ober, *Adv. Mater.* **2008**, *20*, 3355.

[117] C. S. McCowan, T. L. Groy, M. T. Caudle, *Inorg. Chem.* **2002**, *41*, 1120.

[118] W. Clegg, D. R. Harbron, C. D. Homan, P. A. Hunt, I. R. Little, B. P. Straughan, *Inorganica Chim. Acta* **1991**, *186*, 51.

[119] R. M. Gordon, H. B. Silver, *Can. J. Chem.* **1983**, *61*, 1218.

[120] P. Cubillas, K. Etherington, M. W. Anderson, M. P. Attfield, *CrystEngComm* **2014**, *16*, 9834.

[121] N. L. Rosi, J. Eckert, M. Eddaoudi, D. T. Vodak, J. Kim, M. O'Keeffe, O. M. Yaghi, *Science,* **2003**, *300*, 1127.

[122] M. Carraro, S. Gross, *Materials,* **2014**, *7*, 3956.

[123] F. R. Kogler, T. Koch, H. Peterlik, S. Seidler, U. Schubert, *J. Polym. Sci. Part B Polym. Phys.* **2007**, *45*, 2215.

[124] U. Schubert, *Chem. Soc. Rev.* **2011**, *40*, 575.

[125] U. Schubert, *Chem. Mater.* **2001**, *13*, 3487.

[126] N. Mojarad, J. Gobrecht, Y. Ekinci, *Microelectron. Eng.* **2015**, *143*, 55.

[127] N. Mojarad, D. Fan, J. Gobrecht, Y. Ekinci, *Opt. Lett.* **2014**, *39*, 2286.

[128] G. F. Lorusso, T. Sutani, V. Rutigliani, F. Van Roey, A. Moussa, A.-L. Charley, C. Mack, P. Naulleau, C. Perera, V. Constantoudis, *J. Micro/Nanolithography, MEMS, MOEMS* **2018**, *17*, 041009.

[129] G. Palasantzas, *Phys. Rev. B* **1993**, *48*, 14472.

[130] I. Mochi, Y. Ekinci, *Synchrotron Radiat. News* **2019**, *32*, 22.

[131] A. Grenville, J. T. Anderson, B. L. Clark, P. De Schepper, J. Edson, M. Greer, K. Jiang, M. Kocsis, S. T. Meyers, J. K. Stowers, A. J. Telecky, D. De Simone, G. Vandenberghe, *Proc. SPIE* **2015**, *9425*, 94250S.

[132] B. Cardineau, R. Del Re, M. Marnell, H. Al-Mashat, M. Vockenhuber, Y. Ekinci, C. Sarma, D. A. Freedman, R. L. Brainard, *Microelectron. Eng.* **2014**, *127*, 44.

[133] J. Haitjema, Y. Zhang, M. Vockenhuber, D. Kazazis, Y. Ekinci, A. M. Brouwer, *J. Micro/Nanolithography, MEMS, MOEMS* **2017**, *16*, 033510.

[134] T. Gädda, L. N. Dang, M. Laukkanen, K. Karaste, O. Kähkönen, E. Kauppi, D. Kazazis, Y. Ekinci, J. T. Rantala, *Proc. SPIE* **2019**, *10960*, 109600B.

[135] M. Sportelli, M. Valentini, R. Picca, A. Milella, A. Nacci, A. Valentini, N. Cioffi,

Appl. Sci. **2018**, *8*, 77.

[136] Y. Kawamoto, K. Ogura, M. Shojiya, M. Takahashi, K. Kadono, *J. Fluor. Chem.* **1999**, *96*, 135.

[137] E. Polydorou, A. Zeniou, D. Tsikritzis, A. Soultati, I. Sakellis, S. Gardelis, T. A. Papadopoulos, J. Briscoe, L. C. Palilis, S. Kennou, *J. Mater. Chem. A* **2016**, *4*, 11844.

[138] S. G. Rosenberg, M. Barclay, D. H. Fairbrother, *ACS Appl. Mater. Interfaces* **2014**, *6*, 8590.

[139] K. Ahlenhoff, S. Koch, D. Emmrich, R. Dalpke, A. Gölzhäuser, P. Swiderek, *Phys. Chem. Chem. Phys.* **2019**, *21*, 2351.

[140] F. Lebreux, F. Buzzo, I. Marko, *ECS Trans.* **2008**, *13*, 1.

[141] C.-C. Yeh, H.-C. Liu, W. Heni, D. Berling, H.-W. Zan, O. Soppera, *J. Mater. Chem. C* **2017**, *5*, 2611.

[142] F. Stehlin, F. Wieder, A. Spangenberg, J.-M. Le Meins, O. Soppera, *J. Mater. Chem. C* **2014**, *2*, 277.

[143] L. Li, S. Chakrabarty, K. Spyrou, C. K. Ober, E. P. Giannelis, *Chem. Mater.* **2015**, *27*, 5027.

[144] M. Zawadzki, A. Chachereau, J. Kočišek, C. M. Franck, J. Fedor, *J. Chem. Phys.* **2018**, *149*, 204305.

[145] J. P. Wiens, J. C. Sawyer, T. M. Miller, N. S. Shuman, A. A. Viggiano, M. Khamesian, V. Kokoouline, I. I. Fabrikant, *Phys. Rev. A* **2016**, *93*, 32706.

[146] J. Langer, M. Stano, S. Gohlke, V. Foltin, S. Matejcik, E. Illenberger, *Chem. Phys. Lett.* **2006**, *419*, 228.

[147] M. Orzol, T. Sedlacko, R. Balog, J. Langer, G. P. Karwasz, E. Illenberger, A. Lafosse, M. Bertin, A. Domaracka, R. Azria, *Int. J. Mass Spectrom.* **2006**, *254*, 63.

[148] E. Böhler, J. Warneke, P. Swiderek, *Chem. Soc. Rev.* **2013**, *42*, 9219.

[149] P. Walther, M. Puchberger, F. R. Kogler, K. Schwarz, U. Schubert, *Phys. Chem. Chem. Phys.* **2009**, *11*, 3640.

[150] N. Thakur, R. Bliem, I. Mochi, M. Vockenhuber, Y. Ekinci, S. Castellanos, *J. Mater. Chem. C* **2020**, *8*, 14499.

[151] I. Pollentier, Y. Vesters, J. Jiang, P. Vanelderen, D. De Simone, *Proc. SPIE* **2017**, *10450*, 104500H.

[152] H. Fukuda, *J. Micro/Nanolithography, MEMS, MOEMS* **2019**, *18*, 013503.

[153] Y. Komuro, H. Yamamoto, Y. Utsumi, K. Ohomori, T. Kozawa, *Appl. Phys. Express* **2012**, *6*, 14001.

[154] N. Mojarad, J. Gobrecht, Y. Ekinci, *Sci. Rep.* **2015**, *5*, 9235.

[155] K. D. Closser, D. F. Ogletree, P. Naulleau, D. Prendergast, *J. Chem. Phys.* **2017**, *146*, 164106.

[156] S. Grzeskowiak, A. Narasimhan, M. Murphy, L. Napolitano, D. A. Freedman, R. L. Brainard, G. Denbeaux, *Proc. SPIE* **2017**, *10146*, 1014605.

[157] J. Haitjema, L. Wu, A. Giuliani, L. Nahon, S. Castellanos, A. M. Brouwer, *J. Photopolym. Sci. Technol.* **2018**, *31*, 243.

[158] L. Nahon, N. De Oliveira, G. A. Garcia, J. F. Gil, B. Pilette, O. Marcouillé, B. Lagarde, F. Polack, *J. Synchrotron Radiat.* **2012**, *19*, 508.

[159] A. R. Milosavljević, C. Nicolas, J. F. Gil, F. Canon, M. Réfrégiers, L. Nahon, A. Giuliani, *J. Synchrotron Radiat.* **2012**, *19*, 174.

[160] D. J. Frisch, M. J.; Trucks, G. W.; Schlegel, H. B.; Scuseria, G. E.; Robb, M. A.; Cheeseman, J. R.; Scalmani, G.; Barone, V.; Petersson, G. A.; Nakatsuji, H.; Li, X.; Caricato, M.; Marenich, A. V.; Bloino, J.; Janesko, B. G.; Gomperts, R.; Mennucci, B.; Hratch, **2016**, Gaussian.

[161] L. Patiny, A. Borel, *J. Chem. Inf. Model.* **2013**, *53*, 1223.

[162] O. R. Wood, H. Kinoshita, in *EUV Lithogr.* (Ed.: V. Bakshi), SPIE, Washington, **2018**, pp. 1–56.

[163] I. Bespalov, Y. Zhang, J. Haitjema, R. M. Tromp, S. J. Van Der Molen, A. M. Brouwer, J. Jobst, S. Castellanos, *ACS Appl. Mater. Interfaces* **2020**, *12*, 9881.

[164] J. M. Sturm, F. Liu, E. Darlatt, M. Kolbe, A. A. I. Aarnink, C. J. Lee, F. Bijkerk, *J. Micro/Nanolithography, MEMS, MOEMS* **2019**, *18*, 1.

[165] R. M. Thorman, R. Kumar, D. H. Fairbrother, O. Ingólfsson, *Beilstein J. Nanotechnol* **2015**, *6*, 1904.

[166] J. H. Ma, P. Naulleau, M. Ahmed, O. Kostko, *J. Appl. Phys.* **2020**, *127*, 245301.

[167] E. Böhler, J. Warneke, P. Swiderek, *Chem. Soc. Rev.* **2013**, *42*, 9219.

[168] A. Thete, D. Geelen, S. Wuister, S. J. van der Molen, R. M. Tromp, *Proc. SPIE* **2015**, *9422*, 94220A.

[169] J. Kaminsky, S. Grzeskowiak, S. Gibbons, J. Chandonait, U. Welling, S. Gibbons, L. S. Melvin, Y. Kandel, R. L. Brainard, G. H. Denbeaux, *Proc. SPIE* **2018**, *10586*, 105861N.

[170] S. Grzeskowiak, J. Kaminsky, S. Gibbons, A. Narasimhan, R. L. Brainard, G. Denbeaux, *J. Micro/Nanolithography, MEMS, MOEMS* **2018**, *17*, 1.

[171] S. Grzeskowiak, K. Jake, S. Gibbons, M. Murphy, J. Chandonait, R. L. Brainard, G. H. Denbeaux, *Proc. SPIE* **2018**, *10586*, 105860D.

[172] R. T. Frederick, J. T. Diulus, D. C. Hutchison, M. Nyman, G. S. Herman, *ACS Appl. Mater. Interfaces* **2019**, *11*, 4514.

[173] K. Ahlenhoff, S. Koch, D. Emmrich, R. Dalpke, A. Gölzhäuser, P. Swiderek, *Phys. Chem. Chem. Phys.* **2019**, *21*, 2351.

[174] M. C. Sharps, R. T. Frederick, M. L. Javitz, G. S. Herman, D. W. Johnson, J. E. Hutchison, *Chem. Mater.* **2019**, *31*, 4840.

[175] M. Rohdenburg, P. Martinović, K. Ahlenhoff, S. Koch, D. Emmrich, A. Gölzhäuser, P. Swiderek, *J. Phys. Chem. C* **2019**, *123*, 21774.

[176] T. E. Madey, *Science (80-.).* **1986**, *234*, 316.

[177] K. Ahlenhoff, C. Preischl, P. Swiderek, H. Marbach, *J. Phys. Chem. C* **2018**, *122*, 26658.

[178] B. W. Jacobs, R. J. T. Houk, B. M. Wong, A. A. Talin, M. D. Allendorf, *Nanotechnology* **2011**, *22*, 375601.

[179] W. E. Wallace, "'Mass Spectra' in NIST Chemistry WebBook, NIST Standard Reference Database Number 69," DOI 10.18434/T4D303, (retrieved October 1, 2020)can be found under https://webbook.nist.gov/cgi/cbook.cgi?Contrib=MSDC**.**

[180] V. Tarnovsky, P. Kurunczi, D. Rogozhnikov, K. Becker, *Int. J. Mass Spectrom. Ion Process.* **1993**, *128*, 181.

[181] N. Thakur, A. Giuliani, L. Nahon, S. Castellanos, *J. Photopolym. Sci. Technol.* **2020**, *33*, 153.

[182] K. O. Christe, D. Naumann, *Spectrochim. Acta Part A Mol. Spectrosc.* **1973**, *29*, 2017.

[183] E. C. Mattson, Y. Cabrera, S. M. Rupich, Y. Wang, K. A. Oyekan, T. J. Mustard, M. D. Halls, H. A. Bechtel, M. C. Martin, Y. J. Chabal, *Chem. Mater.* **2018**, *30*, 6192.

[184] J. Matthew, *Surface Analysis by Auger and X-Ray Photoelectron Spectroscopy*, Wiley, **2004**.

[185] A. Chaker, H. R. Alty, P. Tian, A. Kotsovinos, G. A. Timco, C. A. Muryn, S. M. Lewis, R. E. P. Winpenny, *ACS Appl. Nano Mater.* **2021**, *4*, 406.

[186] Z. Geng, X. Kong, W. Chen, H. Su, Y. Liu, F. Cai, G. Wang, J. Zeng, *Angew. Chemie Int. Ed.* **2018**, *57*, 6054.

[187] S. G. Lias, R. D. Levin, K. S. A., "'Ion Energetics Data' in NIST Chemistry WebBook, NIST Standard Reference Database Number 69,"**.**

[188] Y. K. Kim, K. K. Irikura, M. E. Rudd, M. A. Ali, P. M. Stone, J. Chang, J. S. Coursey, R. A. Dragoset, A. R. Kishore, K. J. Olsen, A. M. Sansonetti, G. G. Wiersma, D. S. Zucker, M. A. Zukker, "Electron-Impact Cross Sections for Ionization and Excitation Database, NIST Standard Reference Database 107," DOI 10.18434/T4KK5C, (accessed on March 19, 2021)can be found under https://www.nist.gov/pml/electron-impact-cross-sections-ionization-and-excitation-database, **2004**.

[189] N. S. Shuman, T. M. Miller, J. F. Friedman, A. A. Viggiano, A. I. Maergoiz, J. Troe, *J. Chem. Phys.* **2011**, *135*, 054306.

[190] J. P. Benschop, *Proc. SPIE* **2021**, *11609*, 1160903.

[191] D. De Simone, Y. Vesters, G. Vandenberghe, *Adv. Opt. Technol.* **2017**, *6*, 163.

[192] M. Neisser, K. Cummings, S. Valente, C. Montgomery, Y.-J. Fan, K. Matthews, J. Chun, P. D. Ashby, *Proc. SPIE* **2015**, *9422*, 94220L.

[193] T. Manouras, P. Argitis, *Nanomaterials* **2020**, *10*, 1593.

[194] A. Sekiguchi, Y. Matsumoto, M. Isono, M. Naito, Y. Utsumi, T. Harada, T. Watanabe, *Proc. SPIE* **2018**, *10583*, 1058320.

[195] A. De Silva, *Proc. SPIE* **2021**, *11609*, 116090G.

[196] M. Neisser, K. Cho, K. Petrillo, N. Mark, K. Cho, K. Petrillo, *J. Photopolym. Sci. Technol.* **2012**, *25*, 87.

[197] M. Rohdenburg, N. Thakur, R. Cartaya, S. Castellanos, P. Swiderek, *Phys. Chem. Chem. Phys.* **2021**, *23*, 16646.

[198] J. Raabe, G. Tzvetkov, U. Flechsig, M. Böge, A. Jaggi, B. Sarafimov, M. G. C. Vernooij, T. Huthwelker, H. Ade, D. Kilcoyne, T. Tyliszczak, R. H. Fink, C. Quitmann, *Rev. Sci. Instrum.* **2008**, *79*, 113704.

[199] S. Nannarone, F. Borgatti, A. Deluisa, B. P. Doyle, G. C. Gazzadi, A. Giglia, P. Finetti, N. Mahne, L. Pasquali, M. Pedio, G. Selvaggi, G. Naletto, M. G. Pelizzo, G. Tondello, *AIP Conf. Proc.* **2004**, *705*, 450.

[200] L. Pasquali, A. De Luisa, S. Nannarone, *AIP Conf. Proc.* **2004**, *705*, 1142.

[201] "CXRO X-Ray Interactions With Matter," can be found under http://henke.lbl.gov/optical_constants/.

[202] W. Clegg, D. R. Harbron, C. D. Homan, P. A. Hunt, I. R. Little, B. P. Straughan, *Inorganica Chim. Acta* **1991**, *186*, 51.

[203] L. Hiltunen, M. Leskelä, M. Mäkelä, L. Niinistö, L. Niinistö, *Acta Chem. Scand.* **1987**, *41a*, 548.

[204] R. G. Jones, C. K. Ober, T. Hayakawa, C. K. Luscombe, N. Stingelin, *Pure Appl. Chem.* **2020**, *92*, 1861-1891.

[205] R. Q. Li, M. X. Wang, Q. Y. Zhang, J. G. Chen, K. Wang, X. Y. Zhang, S. Shen, Z. T. Liu, Z. W. Liu, J. Jiang, *Polymers.* **2020**, *12*, 78.

[206] H. Ito, D. C. Miller, *J. Polym. Sci. Part A Polym. Chem.* **2004**, *42*, 1468.

[207] H. Ito, D. C. Miller, C. G. Willson, *Macromolecules* **1982**, *15*, 915.

[208] L. Wu, I. Bespalov, K. Witte, O. Lugier, J. Haitjema, M. Vockenhuber, Y. Ekinci, B. Watts, A. M. Brouwer, S. Castellanos, *J. Mater. Chem. C* **2020**, *8*, 14757.

[209] R. Fallica, B. Watts, B. Rösner, G. Della Giustina, L. Brigo, G. Brusatin, Y. Ekinci, *Nanotechnology* **2018**, *29*, 36LT03.

[210] B. Watts, H. Ade, *Mater. Today* **2012**, *15*, 148.

[211] B. Watts, S. Swaraj, D. Nordlund, J. Lüning, H. Ade, *J. Chem. Phys.* **2011**, *134*, 24702.

[212] G. M. Su, S. N. Patel, C. D. Pemmaraju, D. Prendergast, M. L. Chabinyc, *J. Phys. Chem. C* **2017**, *121*, 9142.

[213] D. A. Outka, J. Stöhr, J. P. Rabe, J. D. Swalen, *J. Chem. Phys.* **1988**, *88*, 4076.

[214] D. A. Outka, J. Stöhr, *J. Chem. Phys* **1988**, *88*, 3539.

[215] O. Dhez, H. Ade, S. G. Urquhart, *J. Electron Spectros. Relat. Phenomena* **2003**, *128*, 85.

[216] D. C. Koningsberger, B. L. Mojet, G. E. Van Dorssen, D. E. Ramaker, *Top. Catal.* **2000**, *10*, 143.

[217] D. Solomon, J. Lehmann, J. Kinyangi, B. Liang, K. Heymann, L. Dathe, K. Hanley, S. Wirick, C. Jacobsen, *Soil Sci. Soc. Am. J.* **2009**, *73*, 1817.

[218] P. S. Bagus, K. Weiss, A. Schertel, C. Wöll, W. Braun, C. Hellwig, C. Jung, *Chem. Phys. Lett.* **1996**, *248*, 129.

[219] J. Sedlmair, S. C. Gleber, C. Peth, K. Mann, J. Niemeyer, J. Thieme, *J. Soils Sediments* **2012**, *12*, 24.

[220] N. Tiwale, A. Subramanian, G. Freychet, E. Gann, K. Kisslinger, M. Lu, A. Stein, J. Kim, C.-Y. Nam, *Proc. SPIE* **2021**, *11612*, 9.

[221] Y. Ekinci, M. Vockenhuber, B. Terhalle, M. Hojeij, L. Wang, T. R. Younkin, *Proc. SPIE* **2012**, *8322*, 83220W.

[222] N. Kenane, D. A. Keszler, *ACS Appl. Mater. Interfaces* **2021**, *13*, 18974.

[223] S. Drewniak, R. Muzyka, A. Stolarczyk, T. Pustelny, M. Kotyczka-Morańska, M. Setkiewicz, *Sensors* **2016**, *16*, 103.

APPENDIX I

NMR of Zn(MA)(TFA)

^{1}H NMR (300 MHz, DMSO-d_6) δ: 1.83 (3H, $-CH_3$, MA), 5.34 (1H, $=CH_2$, MA), 5.83 (1H, $=CH_2$, MA) ppm

^{19}F NMR (300 MHz, DMSO-d_6) δ: -73.94 ($-CF_3$, TFA) ppm

^{13}C NMR (300 MHz, DMSO-d_6) δ: 19.36 ($-CH_3$, MA), 115.04 (s, $-CF_3$, TFA), 122.02 ($=CH_2$, MA), 139.93 (-C=, MA), 158.57 (s, -COO, TFA), 173.00 (-COO, MA) ppm

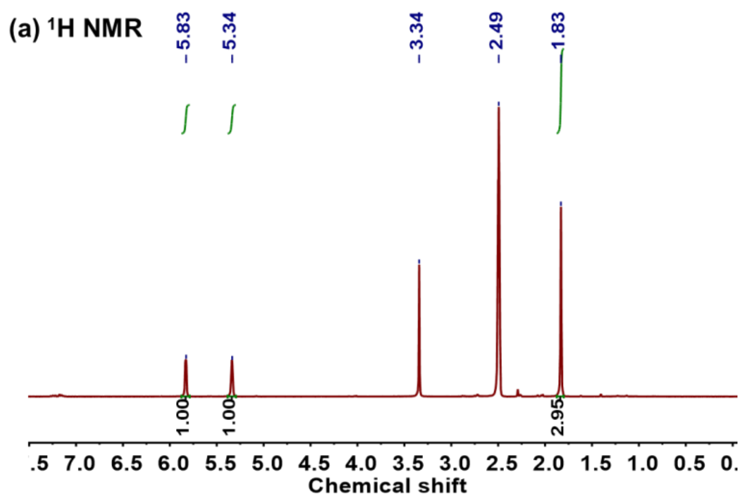

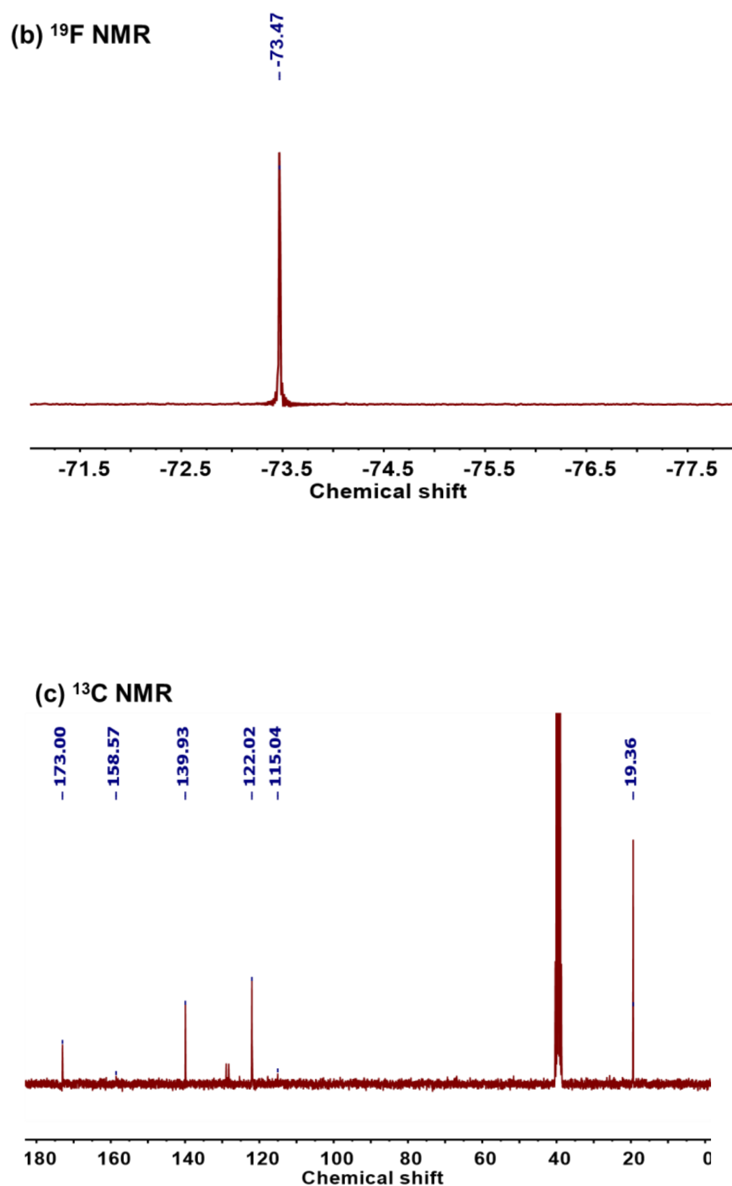

Figure AI.1: (a) ^{1}H NMR, (b) ^{19}F NMR, and (c) ^{13}C NMR of synthesized Zn(MA)(TFA) oxocluster.

APPENDIX II

EUVL performance of Zn(TFA)

EUV exposures were carried out at a wavelength of 13.5 nm (92 eV), at the XIL-II beamline of the Swiss Light Source (SLS) synchrotron. For spectroscopic studies open frame 1.7 × 1.7 mm^2 area mask and pin-hole (PI), 70 μm was used.

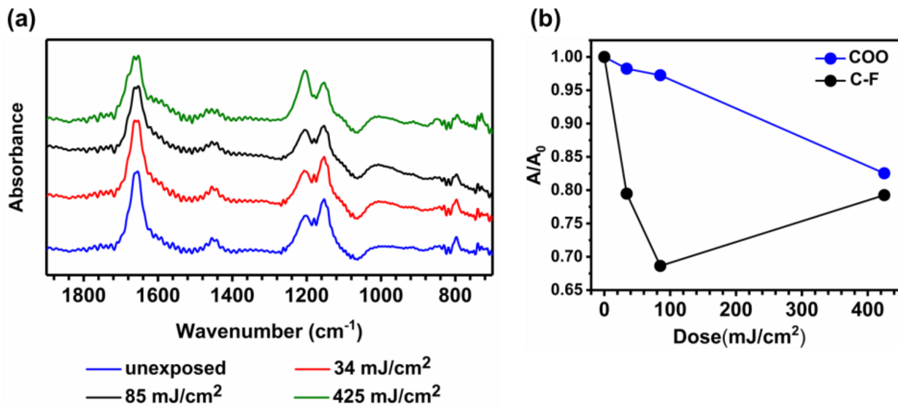

Figure AII.1: (a) FTIR spectra of Zn(TFA) resist film before and after EUV exposure to different doses, and (b) change in the area of the peaks related to TFA ligand: O-C=O and C-F as a function of EUV dose relative to the unexposed resist.

EUV open frame exposures for contrast curves measurements were performed over a range of EUV doses, using a 0.5 × 0.5 mm^2 aperture mask with a PI of 30 μm.

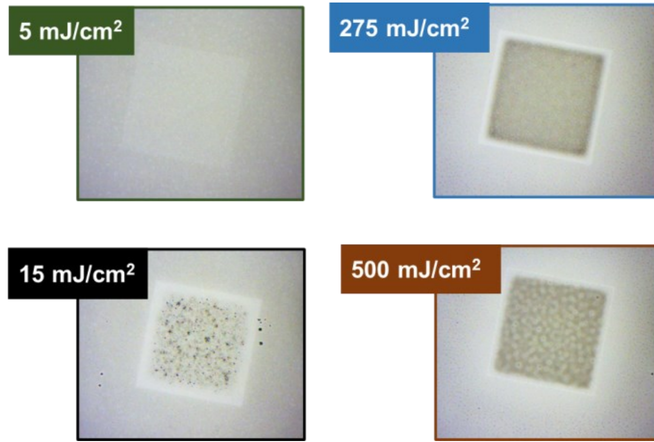

Figure AII.2: Optical microscope image of exposed area of Zn(TFA) resist thin film to EUV photons, without development.

APPENDIX III

NMR of Zn(TFMA)(TFA)

^{1}H NMR (300 MHz, DMSO-d_6) δ: 6.52 (1H, $=CH_2$) and 6.30 (1H, $=CH_2$) ppm

^{19}F NMR (300 MHz, DMSO-d_6) δ: -73.69 (-CF_3, TFA) and -63.92 ((-CF_3, TFMA) ppm

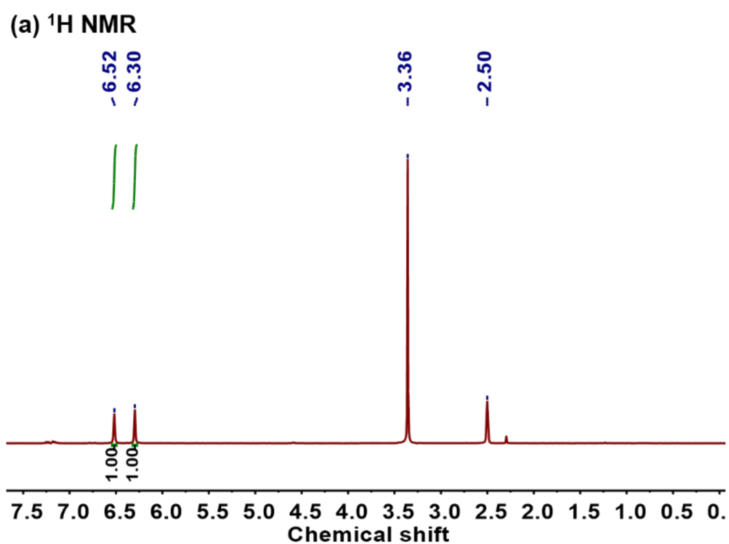

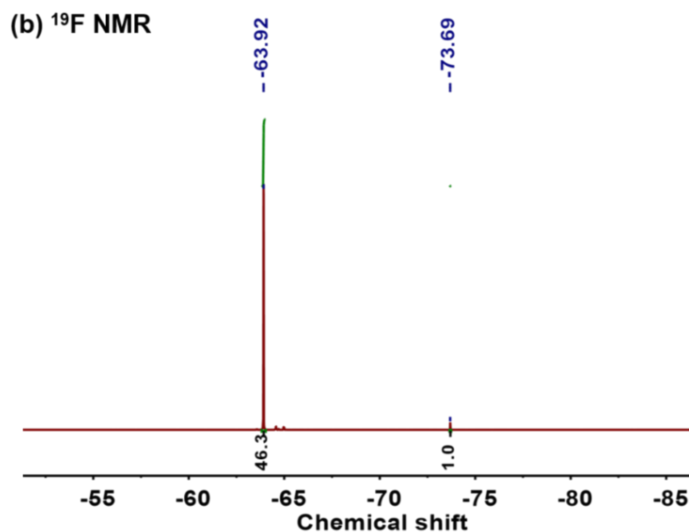

Figure AIII.1: (a) ^{1}H NMR, and (b) ^{19}F NMR of synthesized $Zn(TFMA)_{5.9}(TFA)_{0.1}$. oxocluster.

NMR of Zn(TFMA)(MA)(TFA)

^{1}H NMR (300 MHz, DMSO-d_6) δ: 6.52 (1H, $=CH_2$, TFMA), 6.30 (1H, $=CH_2$, TFMA), 5.85 (1H, $=CH_2$, MA), 5.36 (1H, $=CH_2$, MA) and 1.85 ($-CH_3$, MA) ppm

^{19}F NMR (300 MHz, DMSO-d_6) δ: -73.58 ($-CF_3$, TFA) and -63.85 ($-CF_3$, TFMA) ppm

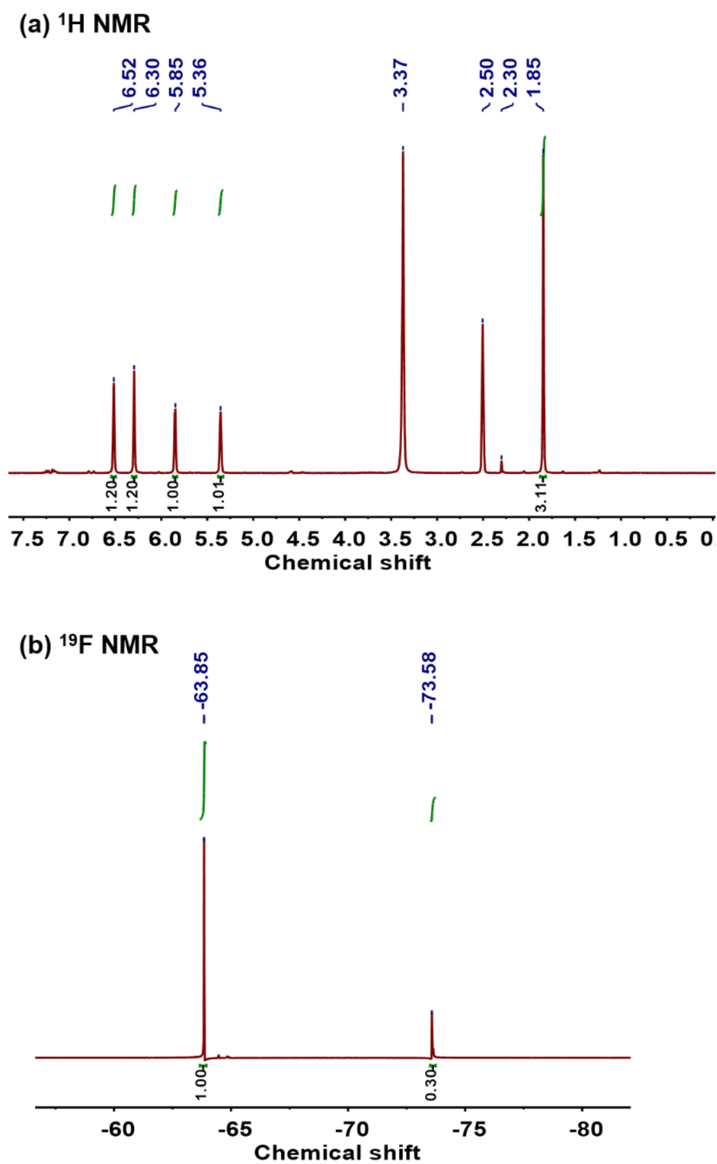

Figure AIII.2: (a) ^{1}H NMR, and (b) ^{19}F NMR of synthesized $Zn(TFMA)_{2.4}(MA)_{2.9}(TFA)_{0.8}$ oxocluster.

SUMMARY

This thesis evaluates hybrid inorganic-organic, zinc-based metal oxoclusters (MOCs) as extreme ultraviolet (EUV, ~92 eV) photoresist materials. The Zn-MOCs comprise a tetranuclear core having four Zn atoms in a tetrahedral geometry bridged by an O in the centre (μ_4-oxo). The core is surrounded by six carboxylate ligands, each bridging two Zn atoms. Zn-MOCs attract great interest as photoresists for EUV lithography (EUVL) applications because their monodisperse particle size ensures homogeneity in thin films and because of the high EUV absorption coefficient of Zn at 92 eV, which is 13.5 times higher than that of C. In this thesis, EUV lithography performance and photochemistry of Zn-MOCs with selected organic shell ligands are explored, making use of the highly dynamic nature of the ligand shell of the MOCs, which provides the flexibility to exchange ligands with simple synthetic approach.

Various tools are used to evaluate the overall performance of the Zn-MOCs for EUVL applications and understand the fundamentals of the interaction of Zn-MOCs with EUV photons. The tool used to evaluate the lithography performance of the Zn-MOCs is EUV-interference lithography (EUV-IL) at the XIL-II beamline in the Paul Scherrer Institute, Switzerland. Further, to gain insights into the chemical changes responsible for the solubility switch following EUV exposure on Zn-MOCs, a combination of different advanced spectroscopic techniques is used, available in our laboratories and at various synchrotron facilities.

In **Chapter 1**, the impact of the semiconductor industry in our modern life, its key technology "*photolithography*" and the advancements it has made over the years are discussed. The photolithography process uses a photosensitive material, the photoresist, to fabricate 3D features on a substrate. The transfer of the features is a multi-step procedure and to enhance their resolution, the wavelength of the imaging light in photolithography has decreased moving from g-line (436 nm) to i-line (365 nm) to KrF (248 nm) to ArF (193 nm) to ArF immersion lithography (ArFi, 193 nm) over the years, and now, EUV (13.5 nm) is introduced as the next-generation technology. The shortening of the wavelength of the imaging light

also demands a simultaneous development of suitable photoresists to meet the requirements of photon absorption and reactivity. The fundamental attributes of photoresists and challenges in the development especially for EUVL applications that lead to the introduction of the hybrid inorganic-organic materials as a promising candidate for EUV photoresist are discussed in this chapter.

In **Chapter 2**, we study the Zn-MOC having a dense tetranuclear Zn-oxo core surrounded by methacrylate (MA) and trifluoroacetate (TFA) ligands in the organic shell, Zn(MA)(TFA). The introduction of MA ligands having a terminal double bond is anticipated to provide an effective solubility switch via cross-linking of double bonds upon exposure. Additionally, the TFA ligand having fluorine is anticipated to enhance the EUV absorption. The shelf life of Zn(MA)(TFA) and its response towards EUV radiation are investigated in this chapter. We found that the Zn-MOC (having labile carboxylate ligands) is susceptible to undergo structural changes on a two months′ timescale when stored as a powder/ bulk material in moisture-free conditions. When deposited as thin film the material undergoes polymerization in a timescale of hours in ambient conditions, shown using UV and IR spectroscopy studies. Nevertheless, the thin films are stable in air as well as in vacuum long enough to perform the lithography process, from thin film application to development (~4.5 h). The results show that Zn(MA)(TFA) is a negative-tone photoresist that displays high EUV absorptivity and appreciable sensitivity towards EUV radiation, albeit with potential batch to batch variations.

In **Chapter 3**, the lithography performance of Zn(MA)(TFA) as an EUV photoresist using the EUV-IL tool is investigated by printing line/space (L/S) patterns of half-pitch (HP) 50 nm, 40 nm, 30 nm and 22 nm. In addition, insights into the complex reaction mechanisms in the material induced upon EUV irradiation are obtained using a combination of spectroscopy techniques: FTIR, UV-vis and X-ray photoelectron spectroscopy (XPS). Zn(MA)(TFA) shows outstanding lithography performance as the L/S patterns of all HP are printed at doses close to 20 mJ/cm^2, which is considered as a target for industrial application of EUV resists. Additionally, the unbiased line-width roughness (LWR) of the printed L/S patterns is calculated and the LWR values of the HP 50 nm, 40 nm and 30 nm are found to fulfil the industry requirement, which demands LWR to be less than 20% of the critical dimension. Spectroscopy studies on EUV exposed samples reveal plausible reaction mechanisms responsible for the solubility switch in the material upon exposure: (i) ionization followed by decarboxylation from the ligand, leading to the generation of reactive radical species in the thin films; (ii) radical initiated cross-linking of the terminal double bonds of the MA ligands; and (iii) formation of new Zn-F species due to reductive C-F bond cleavage of the TFA ligand and migration of fluoride anions from the ligand shell to the Zn-oxo core.

In **Chapter 4**, the photon-induced fragmentations in Zn(MA)(TFA) are investigated. The ionization of material by highly energetic EUV photons is accompanied by the emission of electrons, thus, leaving behind molecular ions with high residual energy and "holes". To study the favourable reaction pathways that can be derived from the holes formed upon exposure to ionizing radiations, photon-induced fragmentations are studied in this chapter. Zn-oxoclusters are brought into the gas phase in their cationic form with a net charge +1 by using the atmospheric pressure photoionization (APPI) technique. Subsequently, the parent cations are trapped in a linear quadrupole ion trap and exposed to ultraviolet (UV) and vacuum ultraviolet (VUV) photons of 4 to 14 eV energy. The study shows that the ligand dissociation from the parent ionic oxocluster is favourable at energies below the second ionization threshold (~12 eV). Formation of $[Zn_3O(MA)_3]^+$ is detected, showing multiple ligand dissociation of the Zn-oxo (μ_4-oxo) core together with loss of a Zn atom. However, above the threshold ~12 eV formation of products from the second ionization event begins to compete with the ligand dissociation process. This study gives the fundamental insights into the reactive sites and stability of the cationic species of Zn(MA)(TFA) after exposure to ionizing radiation.

In **Chapter 5**, we study the electron-induced chemistry of Zn-MOCs. Electron energies of 80 eV and 20 eV are used in these studies: an electron energy of 80 eV mimics the effect of the primary photoelectron, released from the valence band after ionization by EUV photon absorption, while 20 eV electrons fall in the energy range of the low-energy secondary electrons. The chemical changes in the thin films of the oxocluster are monitored by using mass spectrometry (MS) upon electron exposure and measuring reflection absorption infrared spectra (RAIRS) before and after the irradiation of the material. MS shows the desorption of CO_2 from the Zn-MOCs thin films upon electron irradiation with both 80 eV and 20 eV. Additionally, desorption of CO is also detected which points towards the formation of Zn-oxide species in the thin films. Studies show that only a small amount of the reactive species derived from the ligand cleavage (after decarboxylation) desorb while most of these reactive species primarily remains in the thin films. The radical initiated crosslinking processes that consume the terminal double bond of MA, monitored using RAIRS occurs faster than the decarboxylation process. MS also supports the reaction pathway of cleavage of the C-F bond of the TFA ligand via the dissociative electron attachment process (DEA).

In **Chapter 6**, we study the fluorine-rich Zn oxocluster prepared using 2-(trifluoromethyl)acrylate (TFMA) ligand instead of MA, as EUV photoresist. The EUV absorption cross section of a fluorine atom is ~26 times higher than that of H. Therefore, introducing more fluorine in the oxocluster leads to enhanced EUV absorption. EUV contrast curve experiments reveal a decrease in the sensitivity of the fluorine-rich Zn oxoclusters as compared to their analogue Zn(MA)(TFA) studied in chapters 2 and 3. This decrease in the sensitivity can arise from the

electron-withdrawing effect of the $-CF_3$ group at the α position of the TFMA ligand, which decreases the rate of radical homopolymerization of the TFMA unit. In addition, different molecular packing of the Zn(TFMA) oxocluster compared to its analogue Zn(MA)(TFA) or interaction with the developer can also contribute towards this decreased sensitivity. Furthermore, the chemical changes upon EUV exposure were monitored using ex situ near edge X-ray absorption fine structure (NEXAFS), FTIR and UV-vis spectroscopy tools and in situ XPS technique. From the combination of all spectroscopy studies, possible reaction pathways responsible for the solubility switch in fluorine rich Zn-MOC upon EUV exposure are proposed. The studies support decarboxylation events in the carboxylate ligands, as well as the subsequent radical-initiated and low-energy secondary electrons pathways in the thin films responsible for solubility switch. Overall, the presence of CF_3 group in the TFMA ligands hinders smooth thin film formation and lowers the sensitivity but does not change the solubility switch pathway as compared to its analogue Zn(MA)(TFA).

SAMENVATTING

In dit proefschrift onderzoeken we nieuwe materialen voor extreem-ultraviolet (EUV) lithografie (EUVL). In het bijzonder kijken we naar op zink gebaseerde metaal oxoclusters (MOC's), als prototype van een organisch-anorganische hybride fotolak (*photoresist*). Deze Zn-MOC's hebben een kern-structuur met vier Zn atomen in een tetraedergeometrie, verbonden door een O atoom in het midden. Deze kern wordt omringd door zes carboxylaat liganden, die elk verbonden zijn met twee Zn atomen. Zn-MOC's worden beschouwd als een zeer veelbelovende kandidaat als fotolak voor EUV-lithografietoepassingen vanwege de sterke absorptie van Zn bij de fotonenergie van 92 eV die in EUVL wordt gebruikt en vanwege hun monodispersiteit, die ervoor zorgt dat de dunne lagen homogeen zijn. In dit proefschrift worden de prestaties en de fotochemie bekeken van Zn-MOC's met verschillende organische liganden. De ligandschil van de MOC's is van nature zeer dynamisch en biedt de flexibiliteit om de liganden uit te wisselen met een simpele synthetische methode.

Verschillende technieken worden gebruikt om de algehele prestatie van Zn-MOC's voor EUVL-toepassingen te evalueren en om fundamenteel inzicht te verkrijgen in de interactie van Zn-MOC's met EUV-fotonen. Voor het evalueren van de lithografische prestaties van de Zn-MOC's is EUV-interferentielithografie gebruikt in de XIL-II bundellijn bij het Paul Scherrer Instituut in Zwitserland. Verder is een combinatie van verschillende geavanceerde spectroscopische technieken gebruikt, die beschikbaar waren in onze laboratoria en bij verscheidene synchrotronfaciliteiten, om inzicht te verkrijgen in de chemische ontwikkelingen die ten grondslag liggen aan de abrupte verandering in oplosbaarheid na blootstelling aan EUV licht.

In **Hoofdstuk 1** wordt de impact van de halfgeleiderindustrie besproken, evenals de fotolithografietechniek die daarin een centrale rol vervult. Het fotolithografieproces gebruikt een lichtgevoelig materiaal, de fotolak, om driedimensionale structuren te fabriceren op een substraat. Het opbouwen van deze structuren is een procedure met meerdere stappen en om de resolutie

hiervan te kunnen verhogen, heeft het gebruikte licht door de jaren heen een ontwikkeling doorgemaakt naar steeds kortere golflengtes, van *g-line* (436 nm) naar *i-line* (365 nm) naar KrF (246 nm) naar ArF (193 nm) naar ArF immersielithografie (ArFi, 193 nm). Onlangs is EUVL (13.5 nm) geïntroduceerd als de nieuwste techniek voor de komende generaties. De drastische verkorting van de golflengte van het gebruikte licht in EUVL vereist een ontwikkeling van nieuwe fotolakken, om te voldoen aan de vereisten in termen van fotonabsorptie en –reactiviteit. De fundamentele eigenschappen van fotolakken en de uitdagingen in de ontwikkeling ervan, in het bijzonder voor EUVL-toepassingen, die hebben geleid tot het introduceren van de hybride anorganisch-organische materialen als veelbelovende kandidaat voor EUV fotolak worden eveneens in dit hoofdstuk besproken.

In **Hoofdstuk 2** bestuderen we een type Zn-MOC, Zn(MA)(TFA), waarin de tetranucleaire Zn-oxo kern omringd wordt door methacrylaat (MA) en trifluoroacetaat (TFA) liganden. We verwachten dat de introductie van MA-liganden, die eindigen in een dubbele binding, leidt tot een effectieve verandering in oplosbaarheid via de vorming van binding tussen de liganden na blootstelling aan EUV. Als extra bijkomstigheid wordt verwacht dat de aanwezigheid van fluor in de liganden zal bijdragen aan een hogere EUV-absorptie. De houdbaarheid van Zn(MA)(TFA) en de reactie op hoogenergetische EUV-straling worden in dit hoofdstuk onderzocht. We vonden dat de Zn-MOC, vanwege zijn labiele carboxylaat liganden, structurele veranderingen ondergaat op een tijdschaal van 2 maanden wanneer het wordt opgeslagen als poeder/bulk materiaal in vochtvrije omstandigheden. Wanneer het als dunne laag is aangebracht ondergaat Zn(MA)(TFA) polymerisatie op een typische tijdschaal van enkele uren, zoals aangetoond door UV en IR-spectroscopie. Desondanks zijn de dunne lagen zowel in lucht als vacuüm stabiel genoeg om het lithografisch proces te ondergaan, van depositie tot aan ontwikkeling (ca. 4,5 uur). De resultaten tonen aan dat Zn(MA)TFA) een negatieve *photoresist* is met hoge EUV-absorptie en aanzienlijke gevoeligheid voor EUV-straling, zij het met mogelijke variaties van batch tot batch.

In **Hoofdstuk 3** worden de kwaliteiten van Zn(MA)(TFA) als EUV fotolak onderzocht met behulp van de EUV-IL-tool, door het printen van *line/space* (L/S) patronen met een *half-pitch* (HP) van 50 nm, 40 nm, 30 nm en 22 nm. Daarnaast verkrijgen we inzicht in de complexe reactiemechanismen in het materiaal na EUV-blootstelling door een combinatie van spectroscopische technieken, namelijk *FTIR*, *UV-vis* en *X-ray photoelectron spectroscopy* (XPS). Zn(MA)(TFA) vertoont uitstekende lithografische prestaties: alle L/S-patronen worden geprint met behulp van doses rondom 20 mJ/cm^2. In dit opzicht voldoet het aan de wensen van de industrie aan de gevoeligheid van EUV-fotolakken. Verder is de zogeheten *unbiased line-width roughness* (LWR) van de patronen berekend (een maat voor de precisie). De waarden hiervan voor de patronen met een HP van 50

nm, 40 nm en 30 nm voldoen aan de vereisten van de industrie, die zeggen dat de LWR kleiner moet zijn dan 20% van de kritische dimensie. De spectroscopische studies van de aan EUV blootgestelde samples onthullen mogelijke reactiemechanismen voor de verandering in oplosbaarheid van het materiaal na blootstelling: (i) ionisatie gevolgd door decarboxylatie van een ligand, wat leidt tot het ontstaan van reactieve radicalen in de dunne lagen; (ii) door radicalen geïnitieerde kruisverbinding van de dubbele bindingen van de MA liganden en (iii) vorming van nieuwe Zn-F bindingen na verbreking van de C-F binding van het TFA ligand door reductie, gevolgd door migratie van fluoride anionen van de ligand-schil naar de Zn-oxo kern.

In **Hoofdstuk 4** worden de door fotonen geïnduceerde fragmentaties van Zn(MA)(TFA) onderzocht. De ionisatie van materiaal door hoogenergetische EUV-fotonen wordt vergezeld door emissie van elektronen, waarbij er geïoniseerde moleculen met hoge resterende energie en "gaten" achterblijven in de dunne lagen. De foto-geïnduceerde fragmentaties worden hier bestudeerd om de gunstige reactiepaden te onderzoeken van de gaten die door de blootstelling aan ioniserende straling gecreëerd worden. Zn-oxoclusters worden in de gasfase gebracht als kation met netto lading +1 door middel van de *atmospheric pressure photoionization* (*APPI*) techniek. Vervolgens worden de kationen gevangen in een lineaire quadrupool ionenval en aldaar blootgesteld aan ultraviolet (UV) en vacuüm ultraviolet (VUV) fotonen met een energiebereik van tussen de 4 en 14 eV. Het onderzoek wijst uit dat de dissociatie van de liganden in de ionische oxoclusters gunstig is bij energieën beneden de tweede ionisatiegrens (~12 eV). Ook wordt de vorming van $[ZnO(MA)_3]^+$ waargenomen, wat wijst op meervoudige afsplitsing van liganden van de Zn-oxo (μ_4-oxo) kern samen met het verlies van een Zn atoom. Echter, boven de grens van ~12 eV begint de vorming van producten van de tweede ionisatie te wedijveren met de dissociatie van de liganden. Dit onderzoek verschaft fundamenteel inzicht in de reactieve plaatsen en de stabiliteit van de kationische vormen van Zn(MA)(TFA) na blootstelling aan ioniserende straling.

In **Hoofdstuk 5** bestuderen we de door elektronen geïnduceerde chemie van Zn-MOC's. In dit onderzoek worden elektronenergieën van 80 en 20 eV gebruikt: 80 eV elektronen bootsen het effect na van de primaire foto-elektronen die zijn vrijgekomen uit de valentieband na ionisatie door absorptie van EUV-fotonen, terwijl 20 eV elektronen in het energiebereik zitten van de laag energetische secundaire elektronen. De chemische veranderingen in dunne lagen van de oxoclusters worden gevolgd door middel van massaspectrometrie na blootstelling aan de elektronen en door het meten van *reflection absorption infrared spectra* (RAIRS) voor en na blootstelling van het materiaal. MS toont aan dat er desorptie van CO_2 vanuit de dunne lagen van Zn-MOC plaatsvindt na blootstelling aan elektronen van 80 eV en van 20 eV. Hiernaast wordt ook desorptie van CO waargenomen wat duidt op de vorming van Zn-oxides in de dunne lagen. Onderzoek wijst uit dat slechts een klein deel desorbeert van de

reactieve deeltjes afkomstig van de verbreking van liganden (na decarboxylatie), terwijl het merendeel van deze deeltjes achterblijft in de dunne lagen. De door radicalen geïnitieerde kruisverbindingsprocessen die de dubbele binding van MA omzetten, bekeken met behulp van RAIRS, vinden sneller plaats dan het decarboxylatieproces. MS ondersteunt ook de aanwezigheid van het reactiepad van verbreking van de C-F verbinding van de TFA-ligand via het *dissociative electron attachment* (DEA) proces.

In **Hoofdstuk 6** bestuderen we fluorrijke Zn oxoclusters, waarin 2-(trifluoromethyl)acrylaat (TFMA) liganden worden gebruikt in plaats van MA, als EUV *photoresist*. De EUV-absorptie van een fluor atoom is ~26× zo sterk als die van een waterstofatoom. Hierdoor leidt het introduceren van meer fluor in de oxoclusters tot verbeterde EUV-absorptie. EUV-contrast curve experimenten tonen een afname in de gevoeligheid van de fluorrijke Zn oxoclusters vergeleken met hun Zn(MA)(TFA) voorgangers die bestudeerd zijn in hoofdstukken 2 en 3. Deze afname in de gevoeligheid kan toegeschreven worden aan het elektronenzuigende effect van de –CF_3 groep, wat de snelheid van de radicaal-homopolymerisatie van de TFMA-groep vermindert. Een verschillende onderlinge interactie van de Zn(TFMA) oxocluster moleculen vergeleken met hun Zn(MA)(TFA) tegenhangers of verschillende interactie met de ontwikkelaar zouden ook een bijdrage kunnen leveren aan de afname van de gevoeligheid. Verder werden de chemische veranderingen na blootstelling aan EUV gemonitored door middel van zowel ex situ *near edge x-ray absorption fine structure* (NEFAXS), FTIR en UV-vis spectroscopie als in situ XPS. Op basis van de resultaten van al deze spectroscopische onderzoeken worden mogelijke reactiepaden voorgesteld die verantwoordelijk zijn voor de verandering in oplosbaarheid van fluorrijk Zn-MOC. De resultaten ondersteunen het optreden van decarboxylatie van de liganden, evenals daaropvolgende door radicalen en laag energetische secundaire elektronen geïnitieerde reacties in de dunne lagen. Over het geheel beschouwd belemmert de aanwezigheid van de CF_3 groep in TFMA-liganden de vorming van een gelijkmatige dunne laag en verlaagt het de gevoeligheid, maar verandert deze de reactiemechanismen voor de verandering in oplosbaarheid niet vergeleken met hun Zn(MA)(TFA) tegenhanger.

PUBLICATION LIST

This thesis is based on the following publications:

- N. Thakur, M. Vockenhuber, Y. Ekinci, and S. Castellanos, "Zinc-based metal oxoclusters: towards enhanced EUV absorptivity", *Proc. SPIE*, 2019, **10957**, 109570D. DOI: 10.1117/12.2514814;

  N. Thakur, L. T. Tseng, M. Vockenhuber, Y. Ekinci, and S. Castellanos, "Stability studies on a sensitive EUV photoresist based on zinc metal oxoclusters", *J. of Micro/Nanolithography, MEMS, and MOEMS*, 2019, **18**(4), 043504. DOI: 10.1117/1.JMM.18.4.043504 **[Chapter 2]**

- N. Thakur, R. Bliem, I. Mochi, M. Vockenhuber, Y. Ekinci, and S. Castellanos, "Mixed-ligand zinc-oxoclusters: efficient chemistry for high resolution nanolithography", *J. Mater. Chem. C*, 2020, **8**(41), 14499-14506. DOI: 10.1039/D0TC03597A **[Chapter 3]**

- N. Thakur, A. Giuliani, L. Nahon, and S. Castellanos, "Photon-induced fragmentation of zinc-based oxoclusters for EUV lithography applications", *J. Photopolym. Sci. Technol.*, 2020, **33**(2), 153-158. DOI: 10.2494/photopolymer.33.153 **[Chapter 4]**

- M. Rohdenburg, N. Thakur, R. Cartaya, S. Castellanos, and P. Swiderek, "Role of low-energy electrons in the solubility switch of Zn-based oxocluster photoresist for extreme ultraviolet lithography", *Phys. Chem. Chem. Phys.*, 2021, **23**(31), 16646-16657. DOI: 10.1039/D1CP02334A **[Chapter 5]**

- N. Thakur, M. Vockenhuber, Y. Ekinci, B. Watts, A. Giglia, N. Mahne, S. Nannarone, S. Castellanos, and A.M. Brouwer, "Fluorine-rich zinc oxoclusters as EUV photoresists: monitoring chemical changes and lithography performance", *ACS Mater. Au*, 2022. DOI: 10.1021/acsmaterialsau.1c00059. **[Chapter 6]**

Other Publications:

- C. D. Dieleman, J. van der Burgt, N. Thakur, E. C. Garnett, and B. Ehrler, "Direct Patterning of $CsPbBr_3$ Nanocrystals via Electron-Beam Lithography", *ACS Appl. Energy Mater.*, 2022. DOI: 10.1021/acsaem.1c03091

- L. Wu, M.F. Hilbers, O. Lugier, N. Thakur, M. Vockenhuber, Y. Ekinci, A.M. Brouwer, and S. Castellanos, "Fluorescent labeling to investigate nanopatterning processes in extreme ultraviolet lithography", *ACS Appl. Mater. Interfaces*, 2021, **13**(43), 51790-51798. DOI: 10.1021/acsami.1c16257

- O. Lugier, N. Thakur, L. Wu, M. Vockenhuber, Y. Ekinci, and S. Castellanos, "Bottom-up nanofabrication with extreme-ultraviolet light: metal-organic frameworks on patterned monolayers", *ACS Appl. Mater. Interfaces*, 2021, **13**(36), 43777-43786. DOI: 10.1021/acsami.1c13667

- C. D. Dieleman, W. Ding, L. Wu, N. Thakur, I. Bespalov, B. Daiber, Y. Ekinci, S. Castellanos and B. Ehrler, "Universal direct patterning of colloidal quantum dots by (extreme) ultraviolet and electron beam lithography", *Nanoscale*, 2020, **12**(20), 11306-11316. DOI: 10.1039/D0NR01077D

- N. Thakur, P. G. Reddy, S. Nandi, M. Yogesh, S. K. Sharma, C. P. Pradeep, S. Ghosh, and K. E. Gonsalves, "New non-chemically amplified molecular resist design with switchable sensitivity for multi-lithography applications and nanopatterning", *J. Micromech. Microeng.*, 2017, **27**(12), 125010. DOI: 10.1088/1361-6439/aa8751

- P. G. Reddy, N. Thakur, C. L. Lee, S. W. Chein, C. P. Pradeep, S. Ghosh, K. Y. Tsai, and K. E. Gonsalves, "Heavy metal incorporated helium ion active hybrid non-chemically amplified resists: Nano-patterning with low line edge roughness", *AIP Adv.*, 2017, **7**(8), 085314. DOI: 10.1063/1.4989981

ACKNOWLEDGEMENTS

Here's to the end of this chapter;
to all the late nights, early mornings, learnings gained,
and experiences shared.
Here's to the hardships that became our teachers;
to the heaviness that taught us how to rise again,
and to the people who would stop their world to sit
and celebrate our presence.

Here's to the times we chose feeling over disconnection;
freedom over perfection;
courage over what's known and certain
and doing the work.
Here's to releasing what wasn't ours to keep.
Here's to holding our palms wide open to our blessings;
and here's to taking one step forward into the hope & possibility of tomorrow.

-Danielle Doby

Four years ago, when I received the acceptance email for my doctoral application, I was thrilled yet nervous to embark upon this journey at ARCNL. Today, as I am writing this acknowledgement, I truly feel nostalgic going down the memory lane, thinking about the memories I have made, the challenges I have conquered and the personal growth I have experienced. My PhD journey was, indeed, a rollercoaster ride with its own hills, dips and loops, but the support I have received from my supervisors, colleagues, friends, and family made this all worthwhile.

Firstly, I would like to express my sincerest gratitude to dr. Sonia Castellanos, my first PhD supervisor. Thank you for believing in me, and for providing me with a healthy research-oriented atmosphere, which greatly helped me to adapt in my initial days. Your presence has always encouraged me and provided

independence and clarity to my thoughts. I am also thankful for the numerous opportunities you provided me which has helped me in my professional growth.

Secondly, I would like to thank prof. Fred Brouwer, my direct supervisor during the second phase of my PhD, for welcoming me in your group and for making it, indeed, a comfortable transition for me. To be honest, I was bit worried about the course of my PhD when Sonia announced her relocation. The pandemic made it even worse. But the first meeting we had about my progress and future prospective made me feel reassured. Thank you for your advice and insightful suggestions during our group discussions and synchrotron experiments, which always helped me to gain a better perspective on my research. Honestly, I have learnt a lot under your supervision. Also, thank you for always being an e-mail away.

I would also like to thank all the committee members, prof. Elizabeth von Hauff, prof. Sander Woutersen, prof. Bruno Ehrler, prof. Subrata Ghosh, and dr. Jara García Santaclara, for investing time in reading my thesis.

I am thankful to all the collaborators with whom I worked on several projects, without your support and commitment, my PhD would have been impossible. I would specifically like to acknowledge; from Paul Scherrer Institute: Michaela Vockenhuber, dr. Yasin Ekinci, dr. Iacopo Mochi, dr. Dimitrios Kazazis, dr. Li-Ting Tseng from XIL-II beamline and dr. Benjamin Watts from PolLux beamline; from SOLEIL synchrotron: dr. Alexandre Giuliani and dr. Laurent Nahon; from Elettra synchrotron: dr. Nicola Mahne, dr. Angelo Giglia and prof. Stefano Nannarone. dr. Roland Bliem (ARCNL), I am grateful for your help with the XPS experiments and data analysis. dr. Ruben Mass (ASML), thank you for always taking your time out for discussions and insights into the SEM metrology. prof. Petra Swiderek (Bremen University), thank you for our productive collaboration which resulted in the research output as hot article presented in Chapter 5.

Special thanks to all the technicians and research staff, from ARCNL: Arend-Jan van Calcar, Bartjan Spaanderman, Mark Mol, Nick Feldman, Reinout Jaarsma, Sander van Leeuwen, and Thomas van den Hooven; from AMOLF: Andries Lof, Bob Drent, Dimitry Lamers, Hans Zeijlemaker, and Igor Hoogsteder; from UvA: Hans Sanders, Michiel Hilbers, and Wim Roeterdink; the work presented in my thesis would not have been possible without your support and help.

Thanks to all the group members that were part of EUV photochemistry and Nanophotochemistry group at ARCNL. Yu, thank you for all the help in XIL-II beamline during my first year; Lianjia, Olivier, Quentin, and Najmeh thank you for being my synchrotron companion and night owls during our synchrotron shifts and for crazy conversations and laughter; Jarich, thank you for all the meaningful conversations; Ivan, thank you for being a helpful and humorous colleague; Felix, thank you for funny random conversations and for sharing memes over internet and for visiting me in Finland; Marco, thank you for all the

help during my first few weeks at ARCNL. I am also thankful to Aniket, Christian (AMOLF), Jeremy, Maarten, Marie-Noelle, Robbert, and Unnati for your cooperation and extending support during my PhD.

Victor, you were the first person outside my research group with whom I happened to interact with during your second lunch. I am glad that all your plans to kill me at ARCNL failed and I eventually managed to survive! Jokes apart, thank you for all the fun talks, feeding me fine tuna pizza, and all the wisdom you have imparted. Thank you for translating my thesis's summary in Dutch language, and for being my paranymph. Maisie and Randy, thank you for making me feel welcomed and comfortable at your home. To all the lunches, dinners and sleepovers at your place, a big cheer and thank you. Also, Maisie, thank you for being my paranymph. Stephen, you are the one I have always reached out to whenever I needed help, be it at any time of the day. Thanks for making me feel like home whenever I was homesick. Zoey, thank you for cooking amazing vegan food, showering love and all the good memories. I will cherish them forever. Ale A., thank you for being a lovely friend, and for participating in our stupid conversations. More importantly, thank you for helping me with Julia language. Ruben, you are a confetti of happiness, and thank you for spreading joy. John, thank you for the fun, weird, and yet amazing conversations. Lucas, thank you for adopting my pressure cooker and I hope you're taking good care of it. Fengling, although we only interacted during my last days at ARCNL, I am thankful for your help during my move to Finland. It was a pleasure knowing you. I would also like to thank Ale. T., Antonios, Christos, Cyrian, Diko, Felix. C, Feng-Chun, Fiona, Gorsel, Guido, Jan, Junxio, Lars, Maksym, Matthijs, Stefan, Sylvianne, Vanessa, Zeudi: you guys are amazing and thank you for all the fun we had during my time at ARCNL.

I would also like to extend my gratitude to my colleagues from the Molecular Photonics group at UvA. Thank you to the members, dr. Annemieke Petrignani, Prof. Hong Zhang, dr. Rene Williams, Prof. Sander Woutersen, and Prof. Wybren Jan Buma, for your inputs and suggestions during our group meetings. Aishwarya, Begum, Benjamin, Chao, Daire, Dina, Dongdong, Hernan, Ivan, Jiayun (thank you for being a sweet friend), Mark, Maximilan (तुम अपरंपार हो। :P), Qiqing, Roberto, Yanni, Yansong, Yorrick, and Zoi, thank you for your companionship and discussions during our group meetings.

Getting through these four years required more than the academic support and I am glad I met some beautiful souls outside my work life.

Krishma, I am glad that we met in Amsterdam, even though we literally stayed in the same student hostel building in New Delhi for two years. I could confine in you without the fear of being judged. Thank you for your support throughout in Amsterdam, taking care of me when I was sick and for all the lovely times. I miss you!

Thank you, Ambuj, Arjun, Khushi, KK, Kuldeep, Mangal, Mohsin, Monika, Payal, and Sumit, for your support and good times. Thank you for making my PhD journey memorable.

Special gratitude to prof. Subrata Ghosh, I will always be grateful for your support and encouragement. The experience which I gained in your group at IIT Mandi equipped me with right tools that have helped me achieve this PhD. Also, thanks to dr. Atul Chaudhari for your encouragement and support.

Dakshita, Nalin, Nitin, Sukrit, and Yash, thank you for all the fun conversations, laughter's and for being so warm and kind. Abhishek, Adesh, Kunal, Navneet, Pratiksha, Priybrat, Punit, Rahul, Reetu, Rohit, and Ruchika, a big thank you for all the weekend conversations and laughter.

Sarthak, without you, none of this would have been possible. You have been by my side throughout, even before my PhD journey began, and without your support, I would not have had the courage to embark on this journey in the first place. Thank you for always acting as wind beneath my wings!

Last but not the least, I would like to thank my family, maa, bhai, dadda and amma, thank you for believing in me and supporting me in all my decisions, and for bringing in so much love, laughter, energy, and positivity into my life.

It is impossible to put in words, the efforts of all the people who have helped me reach here in their personal capacity. I apologize if I forgot to acknowledge someone here.